A THEORETICAL STUDY OF ELECTROCHEMICAL CARBON DIOXIDE REDUCTION REACTION ON COPPER–ZINC CATALYSTS

ATHIS WATWIANGKHAM

A Thesis Submitted in Partial Fulfillment of the Requirements for the
Degree of Doctor of Philosophy in Chemistry
Suranaree University of Technology
Academic Year 2023

การศึกษาเชิงทฤษฎีของปฏิกิริยารีดักชันเชิงเคมีไฟฟ้าของคาร์บอนไดออกไซด์บนตัวเร่งปฏิกิริยาทองแดงและสังกะสี

นายอธิศ วัดเวียงคำ

วิทยานิพนธ์นี้เป็นส่วนหนึ่งของการศึกษาตามหลักสูตรปริญญาวิทยาศาสตรดุษฎีบัณฑิต
สาขาวิชาเคมี
มหาวิทยาลัยเทคโนโลยีสุรนารี
ปีการศึกษา 2566

A THEORETICAL STUDY OF ELECTROCHEMICAL CARBON DIOXIDE REDUCTION REACTION ON COPPER–ZINC CATALYSTS

Suranaree University of Technology has approved this submitted in partial fulfillment of the requirements for the Degree of Doctor of Philosophy.

Thesis Examining Committee

(Dr. Anchalee Junkaew)
Chairperson

(Assoc. Prof. Dr. Suwit Suthirakun)
Member (Thesis Advisor)

(Prof. Dr. Kritsana Sagarik)
Member

(Assoc. Prof. Dr. Kamonwad Ngamchuea)
Member

(Dr. Sarawoot Impeng)
Member

(Assoc. Prof. Dr. Yupaporn Ruksakulpiwat)
Vice Rector for Academic Affairs
and Quality Assurance

(Prof. Dr. Santi Maensiri)
Dean of the Institute of Science

อธิศ วัดเวียงคำ : การศึกษาเชิงทฤษฎีของปฏิกิริยารีดักชันเชิงเคมีไฟฟ้าของคาร์บอนไดออกไซด์บนตัวเร่งปฏิกิริยาทองแดงและสังกะสี (A THEORETICAL STUDY OF ELECTROCHEMICAL CARBON DIOXIDE REDUCTION REACTION ON COPPER–ZINC CATALYSTS). อาจารย์ที่ปรึกษา : รองศาสตราจารย์ ดร.สุวิทย์ สุธีรากุล, 92 หน้า

คำสำคัญ: ปฏิกิริยารีดักชันของคาร์บอนไดออกไซด์ การเร่งปฏิกิริยาเชิงเคมีไฟฟ้า เอทานอล ทองแดง สังกะสี ทฤษฎีฟังก์ชันนอลความหนาแน่น

ปฏิกิริยารีดักชันเชิงเคมีไฟฟ้าของคาร์บอนไดออกไซด์ (CO_2RR) เป็นหนึ่งในกระบวนการที่มีประสิทธิภาพสูงในการเปลี่ยน CO_2 เป็นผลิตภัณฑ์ที่มีมูลค่าเพิ่มชนิดต่าง ๆ โดยตัวเร่งปฏิกิริยาเชิงไฟฟ้าที่มีโลหะ 2 ชนิดซึ่งประกอบด้วยทองแดงและสังกะสีได้รับความสนใจอย่างมากเนื่องจากเป็นตัวเร่งปฏิกิริยาที่มีประสิทธิภาพและมีความจำเพาะในการผลิตเอทานอลจากกระบวนการ CO_2RR แม้ว่าการศึกษากระบวนการ CO_2RR บนตัวเร่งปฏิกิริยาเดี่ยวของทองแดงและสังกะสี รวมทั้งอัลลอยชนิดเนื้อเดียวจะมีจำนวนมาก แต่การศึกษากระบวนการ CO_2RR บนพื้นผิวระหว่างโลหะทองแดงและสังกะสีแบบวิวิธพันธ์นั้นยังมีไม่มากนัก ดังนั้น ผู้วิจัยจึงทำการศึกษาผลของพื้นผิวระหว่างโลหะทองแดงและสังกะสีต่อกระบวนการ CO_2RR ไปเป็นเอทานอลของตัวเร่งปฏิกิริยาทองแดงและสังกะสีแบบแยกวัฏภาคด้วยวิธีการเชิงทฤษฎี จากการศึกษา พบว่า ตำแหน่งพื้นผิวดังกล่าวมีผลกระทบอย่างยิ่งต่อกระบวนการ CO_2RR โดยการเปลี่ยนแปลงความเสถียรของสารมัธยันตร์และส่งเสริมให้เกิดปฏิกิริยาการควบรวมระหว่างสารมัธยันตร์สองชนิดที่มีคาร์บอนหนึ่งอะตอมซึ่งแตกต่างจากปฏิกิริยาบนตำแหน่งอื่น ได้แก่กระบวนการควบรวมระหว่าง *CO และ *CH ซึ่งมีโอกาสเกิดขึ้นได้สูงทั้งเชิงอุณหพลศาสตร์และจลนศาสตร์ หลังจากกระบวนการควบรวมดังกล่าว ปฏิกิริยาการผลิตเอทานอลที่ตำแหน่งพื้นผิวระหว่างโลหะจะมีโอกาสเกิดขึ้นได้มากกว่าปฏิกิริยาการผลิตเอทิลีน นอกจากนี้ ผู้วิจัยยังทำการศึกษากระบวนการ CO_2RR บนตำแหน่งโลหะทองแดงเพื่อเปรียบเทียบกับตำแหน่งพื้นผิวระหว่างโลหะอีกด้วย จากผลการศึกษาสามารถสรุปได้ว่า ตำแหน่งพื้นผิวระหว่างโลหะ 2 ชนิดมีส่วนช่วยในกระบวนการ CO_2RR ไปเป็นเอทานอลอย่างจำเพาะบนตัวเร่งปฏิกิริยาที่มีทองแดงและสังกะสีแบบแยกวัฏภาค

สาขาวิชาเคมี
ปีการศึกษา 2566

ลายมือชื่อนักศึกษา _____
ลายมือชื่ออาจารย์ที่ปรึกษา _____

ATHIS WATWIANGKHAM : A THEORETICAL STUDY OF ELECTROCHEMICAL CARBON DIOXIDE REDUCTION REACTION ON COPPER–ZINC CATALYSTS. THESIS ADVISOR : ASSOC. PROF. SUWIT SUTHIRAKUN, Ph.D. 92 PP.

Keywords: Carbon dioxide reduction reaction; ethanol; electrocatalysis; copper; zinc; density functional theory

Electrochemical carbon dioxide reduction reaction (CO_2RR) is one of the most efficient methods to convert CO_2 to value-added products. Bimetallic Cu–Zn electrocatalysts have gained considerable interest as one of the effective catalysts for selective CO_2RR to ethanol. Although the CO_2RR has been studied extensively on Cu and Zn monometallic catalysts as well as their homogenous alloys, the reaction on heterogeneous Cu–Zn interface has not been explored yet. Herein, we theoretically studied the effect of interface Cu–Zn site on CO_2 conversion to C_2H_5OH catalyzed by phase-separated Cu–Zn catalysts. The interface site has significant impacts on the CO_2 reduction pathway by tuning the stability of the intermediates and promoting the distinct C–C coupling step. The *CO–*CH coupling at the interface site is the most kinetically and thermodynamically favorable step. The interface site will then favor the ethanol pathway over the ethylene after subsequent *COCH production. The reaction on the Cu site was also studied as the comparative counterpart to highlight the effect of interface site. Overall, this study reveals the cooperative role of the interface site in selective ethanol production for CO_2RR on the Cu–Zn catalysts.

School of Chemistry
Academic Year 2023

Student's Signature _____
Advisor's Signature _____

ACKNOWLEDGEMENTS

First, I would like to thank Assoc. Prof. Dr. Suwit Suthirakun for the opportunity he provided me to pursue a Ph.D. under his supervision. I am grateful for his continuous support, patience, encouragement, and freedom to work on topics of interest. I am thankful to Dr. Pussana Hirunsit from the National Nanotechnology Center (NANOTEC), National Science and Technology Development Agency (NSTDA) for her patience, guidance, and thoughtful discussion about computational electrocatalysis in my Ph.D. dissertation and other projects. I am also grateful to Dr. Anchalee Junkaew, Prof. Dr. Kritsana Sagarik, Assoc. Prof. Dr. Kamonwad Ngamchuea, and Dr. Sarawoot Impeng for serving as members of my defense committee and for their generous contributions of knowledge and expertise, which have been very helpful for this dissertation and my career development. I would also like to thank Jirapat Santatiwongchai for her help and support for the projects we have worked on together.

I would like to thank the Human Resource Development in Science Project (Science Achievement Scholarship of Thailand, SAST) for the PhD scholarship. This research has received funding support from the NSRF via the Program Management Unit for Human Resources & Institutional Development, Research and Innovation [grant number B40G660031]. The research is also financially supported by NANOTEC and Suranaree University of Technology. I would like to acknowledge the NANOTEC supercomputer, the NSTDA Supercomputer Center (ThaiSC), and the Institute of Science, Suranaree University of Technology, for computational resources.

During my research visiting program, I would like to thank Prof. Dr. Andreas Heyden from the Department of Chemical Engineering, University of South Carolina for the great opportunity to do the internship in his research group. I also thank Dr. Subrata Kumar Kundu, and Panuwat Watthaisong for teaching me about the Explicit Solvation model for Metal Surface (eSMS) method. I appreciate the support from the members of Heyden's lab. Furthermore, I would like to thank all my friends and the

Thai Student Association of the University of South Carolina for their help during one year in Columbia, SC.

Over the last four years, my Ph.D. life has had a lot of fun thanks to former and current members of the Computational Materials Science and Catalysis (COMSCAT) group. It has been a memorable experience working with them. I thank all the collaborators for providing me with the opportunity to join their projects which helped me expand my expertise. Moreover, I would like to thank my friends and colleagues from Khon Kaen University, Chiang Mai University, and Suranaree University of Technology for their support.

Finally, I would like to express my gratitude and thanks to my family for their support and encouragement throughout my life.

Athis Watwiangkham

CONTENTS

CONTENTS (Continued)

LIST OF TABLES

LIST OF FIGURES

LIST OF FIGURES (Continued)

LIST OF FIGURES (Continued)

LIST OF FIGURES (Continued)

LIST OF FIGURES (Continued)

LIST OF FIGURES (Continued)

LIST OF ABBREVIATIONS

CO_2RR	= Carbon dioxide reduction reaction
FE	= Faradaic efficiency
RHE	= Reverse hydrogen electrode
DFT	= Density functional theory
VASP	= Vienna ab initio simulation package
PAW	= Projector-augmented wave
PBE	= Perdew-Burke-Ernzerhof
RPBE	= Revised Perdew-Burke-Ernzerhof
CI-NEB	= Climbing image-nudged elastic band
CHE	= Computational hydrogen electrode
NHE	= Normal hydrogen electrode
SCF	= Self-consistent field
LDA	= Local density approximation
LSDA	= Local spin-density approximation
GGA	= Generalized gradient approximation
PAW	= Projector-augmented wave
SHE	= Standard hydrogen electrode
XC	= Exchange-correlation
SCF	= Self-consistent field
ZPE	= Zero-point energy
MP	= Monkhorst-Pack grid
PDS	= Potential-determining step

CHAPTER I

INTRODUCTION

Global warming is the rising of global temperature induced by the increasing atmospheric greenhouse gas concentrations: carbon dioxide (CO_2), methane (CH_4), nitrous oxide (N_2O), ozone (O_3), chlorofluorocarbons (CFCs), and others (Edenhofer, 2015). The mean sea level increase caused by melting polar ice sheets is one of the global warming effects: the annual global mean sea level recently set a record of 91.3 mm above the 1993 level. As the major greenhouse gas, scientists have observed the gradual increase of CO_2 concentration since the industrial revolution in 1800; In 2019, the atmospheric carbon had reached nearly 110 ppm greater than ever in history, and by 2020 it had risen another 2.5 points (Blunden and Boyer, 2021). Human activities are the major causes of CO_2 releasing: burning fuels for energy in heating, cooking, and transporting. Thus, lowering the CO_2 level has become the most urgent mission of humanity.

Reducing atmospheric carbon dioxide (CO_2) can decrease the impact of greenhouse gases on global warming. To lower the atmospheric CO_2 level, electrocatalytic CO_2 reduction reaction (CO_2RR) to value-added hydrocarbon products is one of the promising methods for CO_2 utilization (Jouny, Luc, and Jiao, 2018; 2020). The electrocatalytic cell consists of three main parts, as shown in **Figure 1.1**; two electrodes: an anode and a cathode, and a separator. At the anode (grey), H_2O will oxidize to O_2 and H^+ (oxygen evolution reaction), then H^+ will diffuse through the separator (dotted line) into the cathode (orange) that CO_2 will be reduced to various products (reduction reaction), driven with the applied electricity. Solid metals gain substantial attention as the catalyst for CO_2RR to the value-added products (cathode)—the different metals yield different products and activities (Hori, 2008).

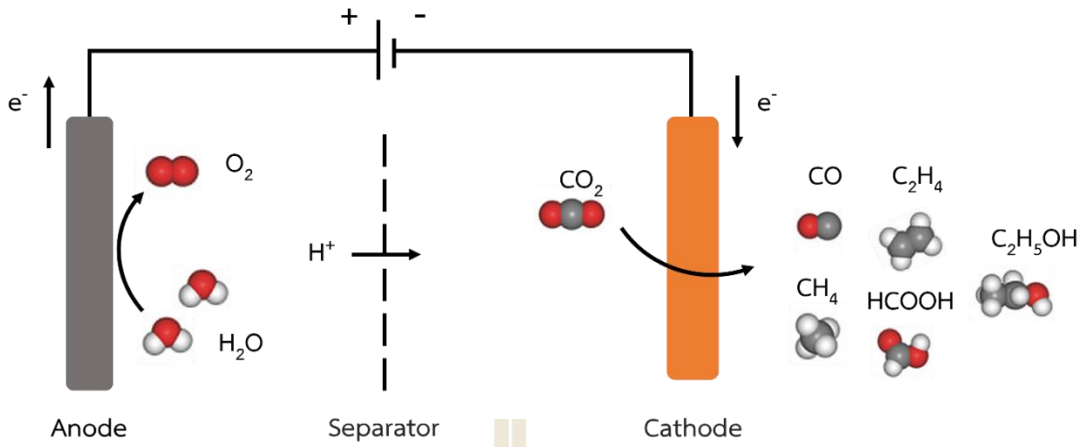

Figure 1.1 Illustration of the electrochemical CO_2 reduction process and the possible products generated in an electrochemical reaction cell.

From the literature, the obtained products from CO_2RR, including carbon monoxide (CO), methane (CH_4), formic acid (HCOOH), ethylene (C_2H_4), ethanol (C_2H_5OH), and others, are highly dependent on the intrinsic properties of catalysts (Feaster et al., 2017; Hori, 2008; Hori, Wakebe, Tsukamoto, and Koga, 1994; Kuhl et al., 2014). Bagger and co-workers divided the monometallic catalysts into four groups based on the major products: H_2, CO, HCOOH, and beyond CO (Bagger, Ju, Varela, Strasser, and Rossmeisl, 2017). For example, the group of metals that majorly yields the H_2 consists of Fe, Ru, Ir, Rh, Pt, Ni, and Pd. CO metals include Au, Ag, and Zn, while HCOOH-favored metals are Cd, Hg, Pb, and Sn. Interestingly, the Cu metals can yield products beyond CO, such as C_2H_4 and C_2H_5OH. Thus, choosing the metal for the CO_2RR affects product selectivity and activity.

Among the metal catalysts, Cu has gained considerable interest due to its relatively high CO_2RR reactivity and the superiority of C_2 production (Gawande et al., 2016; Nitopi et al., 2019). Meanwhile, the C_2H_5OH is a high value-added oxygenate that is an essential feedstock for fuel production, medicine synthesis, and the food industry (Karapinar, Creissen, Rivera de la Cruz, Schreiber, and Fontecave, 2021). However, most Cu catalysts yielded higher selectivity of C_2H_4 than C_2H_5OH (Karapinar et al., 2021; Ren, Ang, and Yeo, 2016; Todorova, Schreiber, and Fontecave, 2020). Moreover, the variety of possible reaction pathways of CO_2RR toward C_2 products on Cu catalysts makes the development of tuning the C_2 selectivity still challenging, especially between C_2H_4 and

C_2H_5OH (Garza, Bell, and Head-Gordon, 2018; Kortlever, Shen, Schouten, Calle-Vallejo, and Koper, 2015; Lum, Cheng, Goddard, and Ager, 2018; Santatiwongchai, Faungnawakij, and Hirunsit, 2021).

To enhance the catalytic activity and selectivity of Cu-based catalysts, researchers have applied various strategies: ion interaction, defect engineering, alloy effect, and others (Yang et al., 2021). The bimetallic alloy effect is a promising way to improve Cu-based catalysts because of their unique electronic and geometric properties (Ferrando, Jellinek, and Johnston, 2008; Li, Wu, Lv, Wang, and Wu, 2022). Several bimetallic Cu-based catalysts shows the high C_2 selectivity for CO_2RR, including Cu–Ce (Shan et al., 2022), Cu–Pd (Ma et al., 2017), Cu–Ni (Song, Tan, Kim, Ringe, and Oh, 2021), Cu–Cd (Mosali et al., 2021), Cu–Au (Zhang et al., 2021), Cu–Ag (Herzog et al., 2021), and Cu–Zn (Juntrapirom et al., 2021). We summarize the bimetallic Cu-based catalysts that yield the C_2 products from CO_2RR, as exhibited in **Figure 1.2**. Thus, bimetallic catalysts are the potential candidate for CO_2RR.

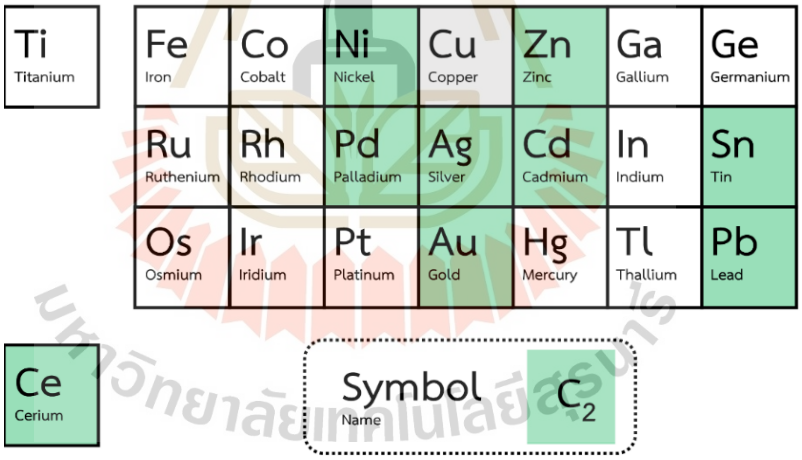

Figure 1.2 The bimetallic Cu–X catalysts (X = the second metal) that produced the C_2 hydrocarbons and oxygenates as the major product from CO_2RR.

As the earth-abundant metal, introducing the Zn into Cu catalysts to generate the cost-effective Cu–Zn catalysts showed the remarkable performance of CO_2RR selectively towards C_2H_5OH. However, C_2H_5OH selectivity from CO_2RR is still low on Cu-based catalysts. Ren and co-workers fabricated various compositions of the phase-separated Cu–Zn catalysts (Ren et al., 2016). They found that the Cu–Zn catalyst with a Cu:Zn ratio of 4:1 yielded the highest efficiency for C_2H_5OH production: 29.1%

Faradaic efficiency (FE) of C_2H_5OH at −1.05 V vs. the reverse hydrogen electrode (RHE), which is higher than those of the monometallic Cu catalyst and the Cu–Zn catalysts with other compositions (Ren et al., 2016).

Similarly, Juntrapirom and co-workers revealed that the phase-separated Cu–Zn (1:1) catalyst yielded the C_2H_5OH as a major product with FE of 11.4% at −1.05 V vs. RHE compared with the Cu catalyst and the homogenous Cu–Zn catalysts (Juntrapirom et al., 2021). These works demonstrate that the bimetallic Cu–Zn catalysts with the phase-separated structure are excellent catalyst candidates for improved CO_2RR selectivity towards C_2H_5OH. Moreover, the Cu–Zn catalyst is more attractive than Cu–Ag, Cu–Au, and Cu–Pd, because of the cost-efficiency. However, the selectivity of CO_2RR on these catalysts involves many possible factors such as spillover, charge transfer, and confinement effects, as demonstrated in **Figure 1.3** (Li et al., 2022; Nitopi et al., 2019; Vasileff, Xu, Jiao, Zheng, and Qiao, 2018; Zhu, Tackett, Chen, and Jiao, 2018). Thus, an in–depth understanding of these effects on the CO_2RR to C_2H_5OH of Cu–Zn catalyst will be beneficial for the catalyst design of the Cu-based electrocatalysts.

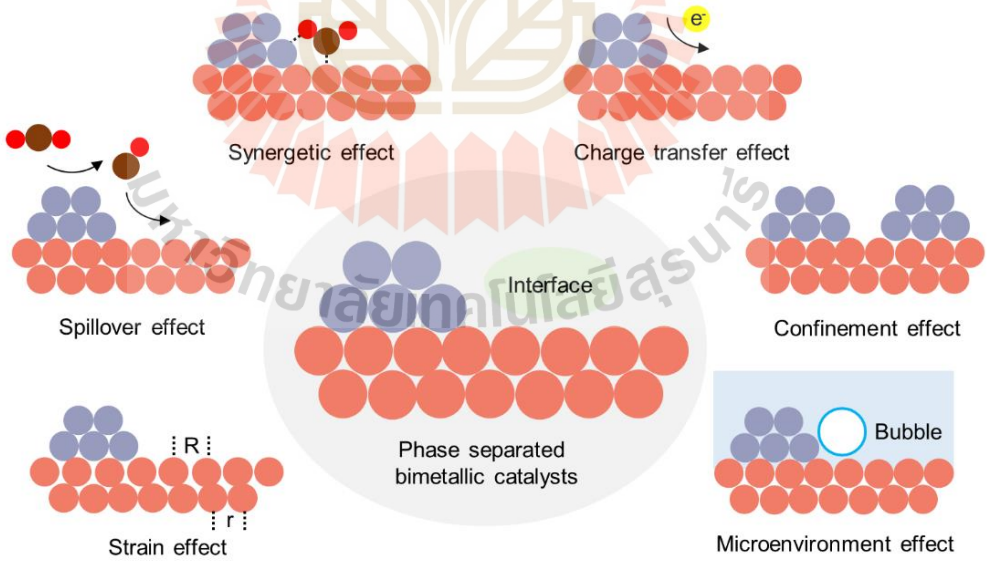

Figure 1.3 Schematic illustration of interface of bimetallic catalysts and their effects for enhanced CO_2RR performance (Li et al., 2022).

Herein, we theoretically investigate the role of the interface Cu–Zn sites on the phase-separated Cu–Zn catalyst in selective CO_2RR toward C_2H_5OH production. The model includes a Zn cluster deposited on Cu(111) surface containing Zn, Cu–Zn interface, and Cu sites. We extensively investigated the CO_2RR pathways: CO_2RR to C_1 products, the possible C–C coupling reaction, and CO_2RR to C_2H_4, and C_2H_5OH.

1.1 Research objectives

Here we use various computational tools to study the role of interface site on CO_2RR to C_2H_5OH on the Cu–Zn catalyst based on the density functional theory (DFT) including CO_2 reaction pathways to CO and CH_4, C–C coupling reactions, and late-stage reduction steps to C_2H_5OH. The hydrogen reduction reaction was also studied as the competitive reaction for CO_2RR.

An atomistic understanding will be benefited for further development of bimetallic Cu-based catalysts for selective CO_2RR to C_2H_5OH.

1.2 Scope and limitation of the study

This thesis aims to understand the role of the interface site of the phase-separated Cu–Zn catalyst on the selective CO_2RR to C_2H_5OH using computational methods based on DFT method as implemented in a Vienna ab initio simulation (VASP) package (Kresse and Furthmüller, 1996). The projector-augmented-wave (PAW) method (Blöchl, 1994; Kresse and Joubert, 1999) were used to treat the core electron in the system. The exchange and correlation energy were applied using the Revised Perdew-Burke-Ernzerhof (RPBE) functional that improves the energetics for atomic and molecular adsorption on transition-metal surfaces (Hammer, Hansen, and Nørskov, 1999). The van der Waals interaction correction was employed using DFT-D3 schemes (Grimme, Antony, Ehrlich, and Krieg, 2010). The solvent effect was included using an implicit solvation model as in the VASPsol package (Mathew, Sundararaman, Letchworth-Weaver, Arias, and Hennig, 2014). We used the 10-atom Zn cluster deposited on Cu(111) surface as the model of Cu–Zn catalyst. The computational hydrogen electrode (CHE) approach was used to account for the coupled proton-electron transfer step in free energy landscape construction (Nørskov et al., 2004). The climbing image nudged elastic band (Henkelman, Uberuaga, and Jónsson, 2000), and

dimer (Henkelman and Jónsson, 1999) methods were performed to find the structures at transition state for CO diffusion and C–C coupling reactions. Barriers for proton transferring steps will be not calculated since those are expected to be quite small and able to overcome under the applied potential (Peterson, Abild-Pedersen, Studt, Rossmeisl, and Nørskov, 2010).

1.3 References

Bagger, A., Ju, W., Varela, A. S., Strasser, P., and Rossmeisl, J. (2017). Electrochemical CO_2 reduction: A classification problem. *ChemPhysChem, 18*(22), 3266-3273.

Blöchl, P. E. (1994). Projector augmented-wave method. *Physical Review B, 50*(24), 17953-17979.

Blunden, J., and Boyer, T. (2021). State of the climate in 2020. *Bulletin of the American Meteorological Society, 102*(8), S1-S475.

Feaster, J. T., Shi, C., Cave, E. R., Hatsukade, T., Abram, D. N., Kuhl, K. P., Hahn, C., Nørskov, J. K., and Jaramillo, T. F. (2017). Understanding selectivity for the electrochemical reduction of carbon dioxide to formic acid and carbon monoxide on metal electrodes. *ACS Catalysis, 7*(7), 4822-4827.

Ferrando, R., Jellinek, J., and Johnston, R. L. (2008). Nanoalloys: From theory to applications of alloy clusters and nanoparticles. *Chemical Reviews, 108*(3), 845-910.

Garza, A. J., Bell, A. T., and Head-Gordon, M. (2018). Mechanism of CO_2 reduction at copper surfaces: Pathways to C_2 products. *ACS Catalysis, 8*(2), 1490-1499.

Gawande, M. B., Goswami, A., Felpin, F.-X., Asefa, T., Huang, X., Silva, R., Zou, X., Zboril, R., and Varma, R. S. (2016). Cu and Cu-based nanoparticles: Synthesis and applications in catalysis. *Chemical Reviews, 116*(6), 3722-3811.

Grimme, S., Antony, J., Ehrlich, S., and Krieg, H. (2010). A consistent and accurate ab initio parametrization of density functional dispersion correction (DFT-D) for the 94 elements H-Pu. *The Journal of Chemical Physics, 132*(15), 154104.

Hammer, B., Hansen, L. B., and Nørskov, J. K. (1999). Improved adsorption energetics within density-functional theory using Revised Perdew-Burke-Ernzerhof functionals. *Physical Review B, 59*(11), 7413-7421.

Henkelman, G., and Jónsson, H. (1999). A dimer method for finding saddle points on high dimensional potential surfaces using only first derivatives. *The Journal of Chemical Physics, 111*(15), 7010-7022.

Henkelman, G., Uberuaga, B. P., and Jónsson, H. (2000). A climbing image nudged elastic band method for finding saddle points and minimum energy paths. *The Journal of Chemical Physics, 113*(22), 9901-9904.

Herzog, A., Bergmann, A., Jeon, H. S., Timoshenko, J., Kühl, S., Rettenmaier, C., Lopez Luna, M., Haase, F. T., and Roldan Cuenya, B. (2021). Operando investigation of Ag-decorated Cu_2O nanocube catalysts with enhanced CO_2 electroreduction toward liquid products. *Angewandte Chemie International Edition, 60*(13), 7426-7435.

Hori, Y. (2008). Electrochemical CO_2 reduction on metal electrodes. In C. G. Vayenas, R. E. White, and M. E. Gamboa-Aldeco (Eds.), *Modern aspects of electrochemistry* (pp. 89-189). New York, NY: Springer New York.

Hori, Y., Wakebe, H., Tsukamoto, T., and Koga, O. (1994). Electrocatalytic process of CO selectivity in electrochemical reduction of CO_2 at metal electrodes in aqueous media. *Electrochimica Acta, 39*(11), 1833-1839.

Jouny, M., Luc, W., and Jiao, F. (2018). General techno-economic analysis of CO_2 electrolysis systems. *Industrial & Engineering Chemistry Research, 57*(6), 2165-2177.

Jouny, M., Luc, W., and Jiao, F. (2020). Correction to "General techno-economic analysis of CO_2 electrolysis systems". *Industrial & Engineering Chemistry Research, 59*(16), 8121-8123.

Juntrapirom, S., Santatiwongchai, J., Watwiangkham, A., Suthirakun, S., Butburee, T., Faungnawakij, K., Chakthranont, P., Hirunsit, P., and Rungtaweevoranit, B. (2021). Tuning CuZn interfaces in metal–organic framework-derived electrocatalysts for enhancement of CO_2 conversion to C_2 products. *Catalysis Science & Technology, 11*(24), 8065-8078.

Karapinar, D., Creissen, C. E., Rivera de la Cruz, J. G., Schreiber, M. W., and Fontecave, M. (2021). Electrochemical CO_2 reduction to ethanol with copper-based catalysts. *ACS Energy Letters, 6*(2), 694-706.

Kortlever, R., Shen, J., Schouten, K. J. P., Calle-Vallejo, F., and Koper, M. T. M. (2015). Catalysts and reaction pathways for the electrochemical reduction of carbon dioxide. *The Journal of Physical Chemistry Letters, 6*(20), 4073-4082.

Kresse, G., and Furthmüller, J. (1996). Efficient iterative schemes for ab initio total-energy calculations using a plane-wave basis set. *Physical Review B, 54*(16), 11169-11186.

Kresse, G., and Joubert, D. (1999). From ultrasoft pseudopotentials to the projector augmented-wave method. *Physical Review B, 59*(3), 1758-1775.

Kuhl, K. P., Hatsukade, T., Cave, E. R., Abram, D. N., Kibsgaard, J., and Jaramillo, T. F. (2014). Electrocatalytic conversion of carbon dioxide to methane and methanol on transition metal surfaces. *Journal of the American Chemical Society, 136*(40), 14107-14113.

Li, X., Wu, X., Lv, X., Wang, J., and Wu, H. B. (2022). Recent advances in metal-based electrocatalysts with hetero-interfaces for CO_2 reduction reaction. *Chem Catalysis, 2*(2), 262-291.

Lum, Y., Cheng, T., Goddard, W. A., and Ager, J. W. (2018). Electrochemical CO reduction builds solvent water into oxygenate products. *Journal of the American Chemical Society, 140*(30), 9337-9340.

Ma, S., Sadakiyo, M., Heima, M., Luo, R., Haasch, R. T., Gold, J. I., Yamauchi, M., and Kenis, P. J. A. (2017). Electroreduction of carbon dioxide to hydrocarbons using bimetallic Cu–Pd catalysts with different mixing patterns. *Journal of the American Chemical Society, 139*(1), 47-50.

Mathew, K., Sundararaman, R., Letchworth-Weaver, K., Arias, T. A., and Hennig, R. G. (2014). Implicit solvation model for density-functional study of nanocrystal surfaces and reaction pathways. *The Journal of Chemical Physics, 140*(8), 084106.

Mosali, V. S. S., Zhang, X., Liang, Y., Li, L., Puxty, G., Horne, M. D., Brajter-Toth, A., Bond, A. M., and Zhang, J. (2021). CdS-enhanced ethanol selectivity in electrocatalytic CO_2 reduction at sulfide-derived Cu–Cd. *ChemSusChem, 14*(14), 2924-2934.

Nitopi, S., Bertheussen, E., Scott, S. B., Liu, X., Engstfeld, A. K., Horch, S., Seger, B., Stephens, I. E. L., Chan, K., Hahn, C., Nørskov, J. K., Jaramillo, T. F., and Chorkendorff, I. (2019). Progress and perspectives of electrochemical CO_2 reduction on copper in aqueous electrolyte. *Chemical Reviews, 119*(12), 7610-7672.

Nørskov, J. K., Rossmeisl, J., Logadottir, A., Lindqvist, L., Kitchin, J. R., Bligaard, T., and Jónsson, H. (2004). Origin of the overpotential for oxygen reduction at a fuel-cell cathode. *The Journal of Physical Chemistry B, 108*(46), 17886-17892.

Peterson, A. A., Abild-Pedersen, F., Studt, F., Rossmeisl, J., and Nørskov, J. K. (2010). How copper catalyzes the electroreduction of carbon dioxide into hydrocarbon fuels. *Energy & Environmental Science, 3*(9), 1311-1315.

Ren, D., Ang, B. S.-H., and Yeo, B. S. (2016). Tuning the selectivity of carbon dioxide electroreduction toward ethanol on oxide-derived Cu_xZn catalysts. *ACS Catalysis, 6*(12), 8239-8247.

Santatiwongchai, J., Faungnawakij, K., and Hirunsit, P. (2021). Comprehensive mechanism of CO_2 electroreduction toward ethylene and ethanol: The solvent effect from explicit water–Cu(100) interface models. *ACS Catalysis, 11*(15), 9688-9701.

Shan, J., Shi, Y., Li, H., Chen, Z., Sun, c., Shuai, Y., and Wang, Z. (2022). Effective CO_2 electroreduction toward C_2H_4 boosted by Ce-doped Cu nanoparticles. *Chemical Engineering Journal, 433*, 133769.

Song, H., Tan, Y. C., Kim, B., Ringe, S., and Oh, J. (2021). Tunable product selectivity in electrochemical CO_2 reduction on well-mixed Ni–Cu alloys. *ACS Applied Materials & Interfaces, 13*(46), 55272-55280.

Todorova, T. K., Schreiber, M. W., and Fontecave, M. (2020). Mechanistic understanding of CO_2 reduction reaction (CO_2RR) toward multicarbon products by heterogeneous copper-based catalysts. *ACS Catalysis, 10*(3), 1754-1768.

Vasileff, A., Xu, C., Jiao, Y., Zheng, Y., and Qiao, S.-Z. (2018). Surface and interface engineering in copper-based bimetallic materials for selective CO_2 electroreduction. *Chem, 4*(8), 1809-1831.

Yang, C., Wang, Y., Qian, L., Al-Enizi, A. M., Zhang, L., and Zheng, G. (2021). Heterogeneous electrocatalysts for CO_2 reduction. *ACS Applied Energy Materials, 4*(2), 1034-1044.

Zhang, L., Li, M., Zhang, S., Cao, X., Bo, J., Zhu, X., Han, J., Ge, Q., and Wang, H. (2021). Promoting carbon dioxide electroreduction toward ethanol through loading Au nanoparticles on hollow Cu_2O nanospheres. *Catalysis Today, 365*, 348-356.

Zhu, W., Tackett, B. M., Chen, J. G., and Jiao, F. (2018). Bimetallic electrocatalysts for CO_2 reduction. *Topics in Current Chemistry, 376*(6), 41.

CHAPTER II

LITERATURE REVIEW

2.1 Electrocatalytic CO_2 reduction reaction on Cu and Zn catalysts

2.1.1 Monometallic Cu catalysts

The Cu metal is a promising catalyst for CO_2RR to C_2 products. Most works showed that the Cu catalysts produced more C_2H_4 than the C_2H_5OH (Nitopi et al., 2019). For example, Hori and co-workers found that the FE of C_2H_4 is 25.5%, while that of C_2H_5OH is 5.7% at −1.44 vs. the normal hydrogen electrode (NHE) (Hori, Wakebe, Tsukamoto, and Koga, 1994). However, the Cu yields the major product of CH_4 with a FE of 33.3% at −1.44 vs. NHE. Ren and co-workers also suggest that C_2H_4 and C_2H_5OH yield the FE of 26.46% and 11.32%, respectively (Ren, Ang, and Yeo, 2016). Meanwhile, the selectivity of the Cu catalyst depends on the Cu facet: Cu(100) favors C_2H_4; Cu(111) favors CH_4 (Todorova, Schreiber, and Fontecave, 2020).

A computational study is one of the powerful tools to understand the selectivity of the products by considering the reaction mechanism of CO_2RR (Nitopi et al., 2019). The exact strategy for controlling the selectivity is still challenging because the products share the same intermediates leading to the complex mechanism pathway, as demonstrated in **Figure 2.1** (Nitopi et al., 2019; Todorova et al., 2020). We divided the CO_2RR mechanism into the C_1 pathway, C–C coupling step, and C_2 pathway.

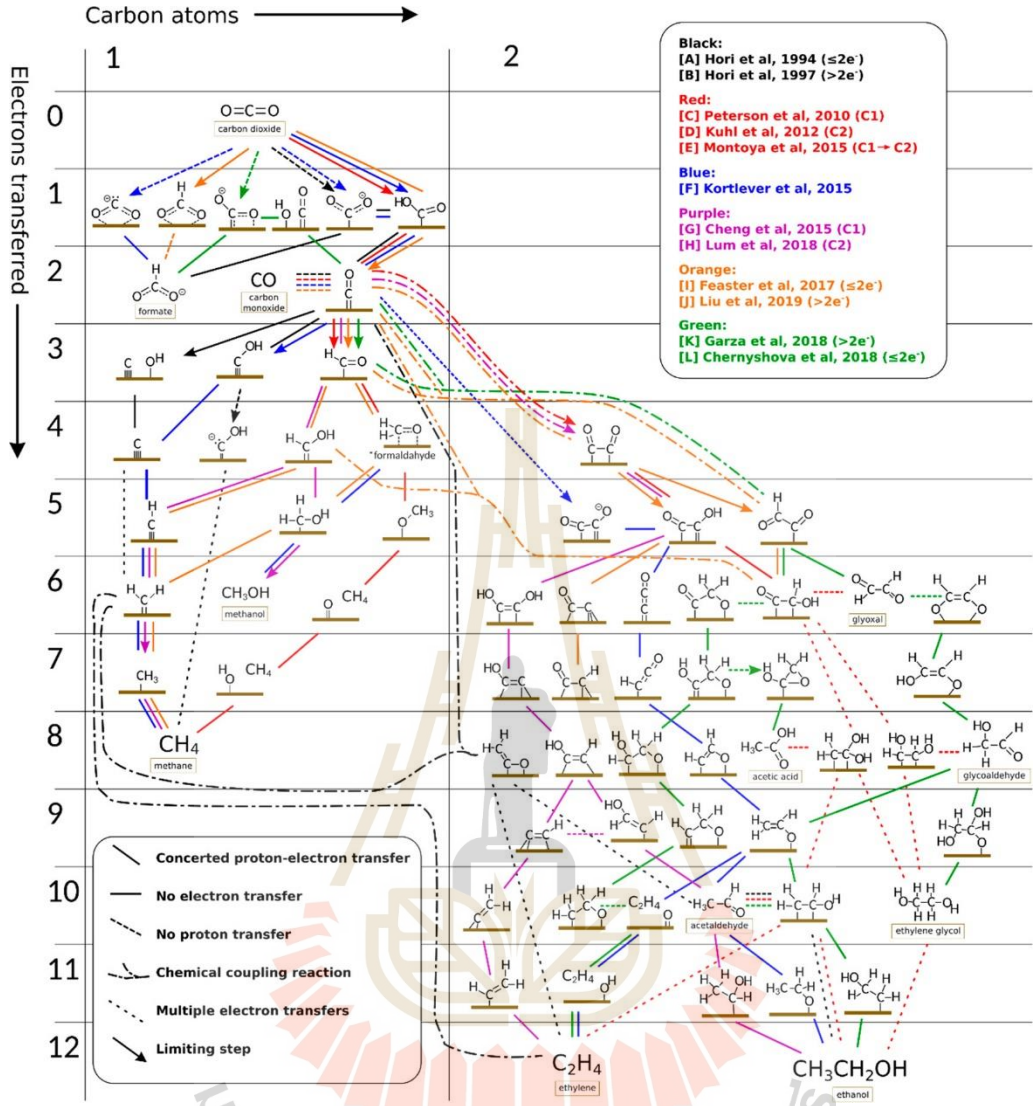

Figure 2.1 Possible reaction pathways of CO_2 reduction to C_1 and C_2 products on polycrystalline copper, grouped into different colored reaction schemes taken from the works in the top-right legend: [A] (Hori et al., 1994); [B] (Hori, Takahashi, Yoshinami, and Murata, 1997); [C] (Peterson, Abild-Pedersen, Studt, Rossmeisl, and Nørskov, 2010); (201) [D] (Kuhl, Cave, Abram, and Jaramillo, 2012); [E] (Montoya, Shi, Chan, and Nørskov, 2015); [F] (Kortlever, Shen, Schouten, Calle-Vallejo, and Koper, 2015); [G] (Cheng, Xiao, and Goddard, 2015); [H] (Lum, Cheng, Goddard, and Ager, 2018); [I] (Feaster et al., 2017); [J] (Liu et al., 2019); [K] (Garza, Bell, and Head-Gordon, 2018); [L] (Chernyshova, Somasundaran, and Ponnurangam, 2018). The bottom-left legend states the meaning of the texture of the lines connecting intermediates. Adopted from the mechanistic compilation by (Nitopi et al., 2019).

For the Cu(111), several works suggested that the Cu(111) favors the CH_4 production for CO_2RR (Dong, Li, and Jiang, 2018; Hussain, Jónsson, and Skúlason, 2018; Luo, Nie, Janik, and Asthagiri, 2016; Nie, Esopi, Janik, and Asthagiri, 2013; Ou and Chen, 2020; Ou, Chen, Chen, and Jin, 2019). On the Cu(111), the pathway for CO_2RR to CH_4 is under discussion because of many possible intermediates and the solvation effect (Dong et al., 2018; Hussain, Jónsson, and Skúlason, 2016; Hussain et al., 2018; Hussain, Skúlason, and Jónsson, 2015; Nie et al., 2013). Peterson and co-workers study the CH_4 formation on pure Cu(111), accounting for the solvent effect by using a hexagonal water overlayer (Peterson et al., 2010). They proposed that the CH_4 formation proceeds through a CHO intermediate and subsequent reduction step to $*CH_2O$, $*CH_3O$, and finally, the CH_4 product. Meanwhile, Nie and co-workers theoretically studied the CH_4 formation on the pure Cu(111) by including the explicit water molecule: the CH_4 production proceeds by reducing CO to COH, leading to CH_x species and finally, CH_4 (Nie et al., 2013).

Recently, Oh and co-workers theoretically studied the CO_2RR to C_1 products on pure Cu(111) modeling in the fully relaxed water layers as the solvation model, as shown in **Figure 2.2(a)** (Ou et al., 2019). The energy profiles for CH_2O and CHOH pathways. For the protonation of *CO, **Figure 2.2(b)** shows that the Cu(111) favored the *CHO due to the lower $\Delta G^{\neq}$ of 0.85 eV than the $\Delta G^{\neq}$ of 1.39 eV of *COH. Then, the *CHO can be reduced to $*CH_2O$ and *CHOH with a slight $\Delta G^{\neq}$ deviation of 0.02 eV. For the CH_2O pathway, the $*CH_3O$ formation has a lower $\Delta G^{\neq}$ of 0.23 eV than $\Delta G^{\neq}$ of 0.32 eV for the $*CH_2OH$, leading to the CH_3OH production (**Figure 2.2(c)**). For the CHOH pathway, the *CH formation has more stability than $*CH_2OH$ with the $\Delta G^{\neq}$ of 0.19 and 0.38 eV, respectively (Ou et al., 2019). In this work, we adopted the CHOH pathway to CH_4 from the work of Ou and co-workers because the CH_2O may favor the CH_3OH more than CH_4 productions (Ou et al., 2019).

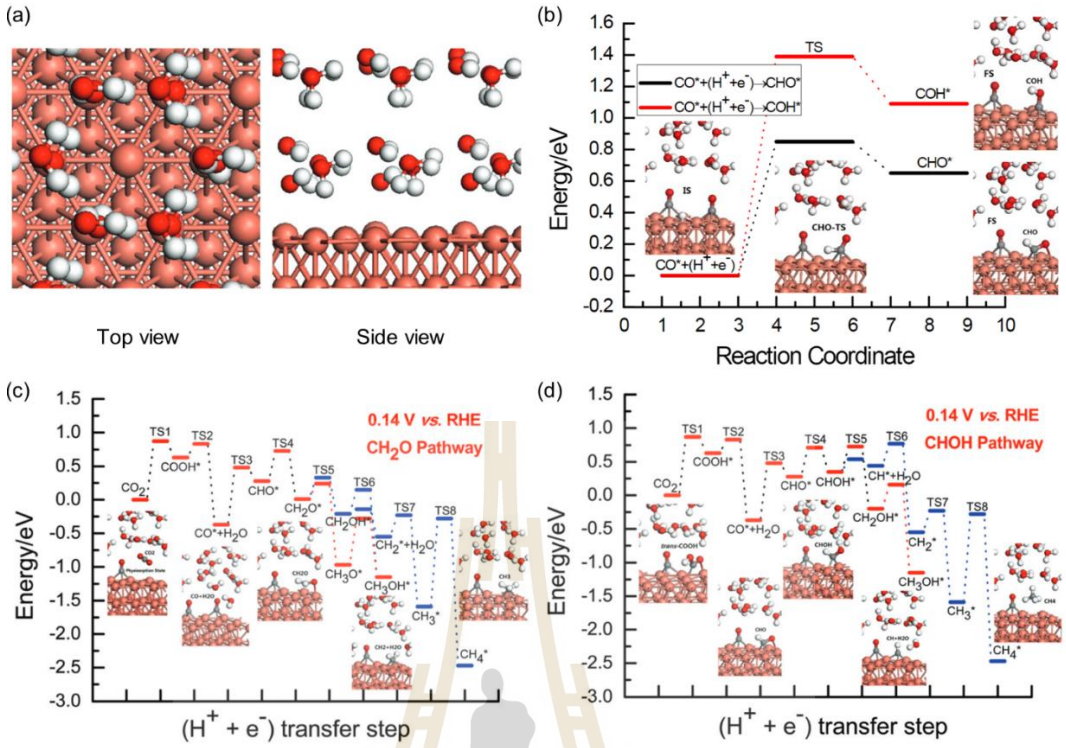

Figure 2.2 The solvation model on Cu(111) (a); the energy profile of CO reduction into CHO and COH intermediates on Cu(111) at 0.14 V vs. RHE (b); the overall energy diagram of CO_2RR to CH_4 and CH_3OH on Cu(111) at 0.14 V vs. RHE: CH_2O pathway (c); CHOH pathway (d). Adopted from (Ou et al., 2019).

For the CO_2RR on different facets of Cu, the Cu(100) favored the C_2 products while Cu(111) favored the CH_4 product (Todorova et al., 2020; W. Zhang et al., 2018). From literature, the superiority of the Cu(100) in CO_2RR to C_2 products, were possibly originated from the facile *CO–*CO and *CO–*CHO coupling steps due to the favorable reaction free energy (ΔG_{rxn}) and free energy barrier ($\Delta G^{\neq}$). **Figure 2.3** shows that Cu with the (100) facet exhibited a barrier of 0.45 eV for the *CO–*CO coupling that is lower than both of (111) and (211) facets of 0.72 eV (Sandberg, Montoya, Chan, and Nørskov, 2016). Liu and co-workers showed that ΔG_{rxn} and $\Delta G^{\neq}$ are 1.00 and 1.22 eV for *CO–*CO coupling, and 0.26, 0.77 eV for *CO–*CHO coupling on Cu(100) (the implicit water model) (Luo et al., 2016). Santatiwongchai and co-workers suggested that the *CO–*CO and *CO–*CHO coupling steps have $\Delta G^{\neq}$ of 1.17 and 0.75 eV, respectively, in the vacuum (Santatiwongchai, Faungnawakij, and Hirunsit, 2021). In the explicit water model, the $\Delta G^{\neq}$ of the *CO–*CO coupling step is lower than that of the

*CO–*CHO step, with the values of 0.49 and 0.91 eV, respectively (Santatiwongchai et al., 2021). In addition, Piqué and co-workers reported that *CO–*CO coupling on the Cu(111) and Cu(100) require the $\Delta G^{\neq}$ of 1.52 and 0.81 eV, respectively (Piqué, Viñes, Illas, and Calle-Vallejo, 2020). These works demonstrated that the different facets give different favored C–C coupling steps that may affect the product selectivity from the CO_2RR.

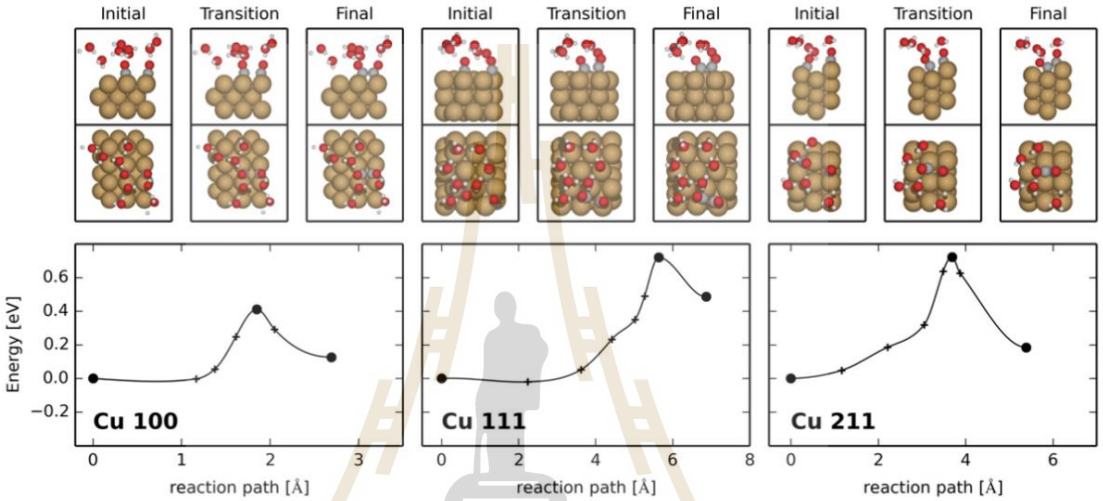

Figure 2.3 Structures and barriers for the *CO–*CO coupling step on Cu surfaces with (100), (111), and (211) facets (Sandberg et al., 2016).

2.1.2 Monometallic Zn catalysts

For the Zn catalysts, most works reported that the Zn catalysts majorly produced the CO from CO_2RR (Kang, Kolb, Calle-Vallejo, and Yeo, 2022; Li, Liu, Li, and Yang, 2018; Luo et al., 2020; Qin et al., 2018; Won et al., 2016; Xiao, Gao, Liu, and Luo, 2020; T. Zhang et al., 2018), while some reported the HCOOH production (Takatsuji, Morimoto, Nakatsuru, and Haruyama, 2022; Zhang, Zhong, Qiu, Li, and Zhang, 2016). For the CO production, Hori and co-workers revealed that the Zn catalyst showed the FE of 79.4% for CO at −1.54 vs. the normal hydrogen electrode (NHE) (Hori et al., 1994). Won and co-workers showed that the Zn catalyst with a hexagonal structure yields the highest FE for CO of 85.4% at −0.95 V vs. RHE (Won et al., 2016). Xiao and co-workers revealed that the hexagonal Zn nanoparticles exhibited the highest CO FE of 94.2% at −0.96 V vs. RHE (Xiao et al., 2020). For the HCOOH production, Zhang and co-workers

showed that the Zn catalyst exhibited a high FE for $HCOO^-$ of 87.1% −1.93 V vs. RHE (Zhang et al., 2016), while Takatsuji and co-workers suggested that the Zn catalysts showed the FE more than 60% at −1.19 V vs. RHE (Takatsuji et al., 2022). In the comparative studies of Cu, Zn, and Cu−Zn, Ren and co-workers showed that the Zn catalysts produced CO with a FE of 75.84% at −1.10 V vs. RHE, which is higher than the $HCOO^-$ with the FE of 6.09% at −1.15 V vs. RHE (Ren et al., 2016). Thus, the Zn catalyst is one of the potential catalysts with promising CO production from CO_2RR.

Computational studies revealed that the selectivity of CO_2RR to CO and HCOOH depends on facets of the Zn catalysts (Qin et al., 2018; Won et al., 2016; Xiao et al., 2020). Won and co-workers studied the CO_2RR to CO on the Zn(002) and Zn(101) as shown in **Figure 2.4(a, b)** (Won et al., 2016). The protonation step of CO_2 to *COOH is the limiting step for the CO_2RR to CO. The Zn(101) prefers more the CO production than that of Zn(002) by 0.43 V due to the *COOH absorptivity of the Zn(101) (Won et al., 2016). Qin and co-workers revealed the similar results that the CO_2RR to CO is more favorable on the Zn(101) than that of the Zn(002), with the relative energy of CO_2 to COOH* of 0.185 and 0.543 eV on the Zn(002), respectively (Qin et al., 2018). Moreover, Xiao and co-workers suggested that the Zn(100) reduces the free energy of CO_2 to COOH*, leading to CO production, compared with the Zn(002) (Xiao et al., 2020).

Furthermore, several works revealed that the edge and corner sites of the hexagonal Zn cluster favor more the CO production than those of (002), (101), and (100) facets of Zn surfaces because the COOH* is very stable at the edge and corner sites, respectively (Xiao et al., 2020; T. Zhang et al., 2018). From **Figure 2.4(c)**, Xiao and co-workers found that the corner sites tend to strongly bind the CO* while the edge site binds CO* weaker than the corner site, enhancing the CO_2RR to CO (Xiao et al., 2020). The d-band center of the surface Zn(100) atoms of Zn is higher than that of Zn(002) (see **Figure 2.4(d)**), leading to a stronger binding ability to the key intermediates (Xiao et al., 2020). Moreover, Kang and co-workers showed that the undercoordinated Zn sites provide the higher activity for the CO production because of optimal *COOH adsorption energies for the CO_2RR to CO (Kang et al., 2022). The origin of high activity for CO_2RR to CO on hexagonal Zn nanoparticles is due to the high

absorptivity of low-coordinated atoms for the key intermediate (Kang et al., 2022; Xiao et al., 2020; T. Zhang et al., 2018).

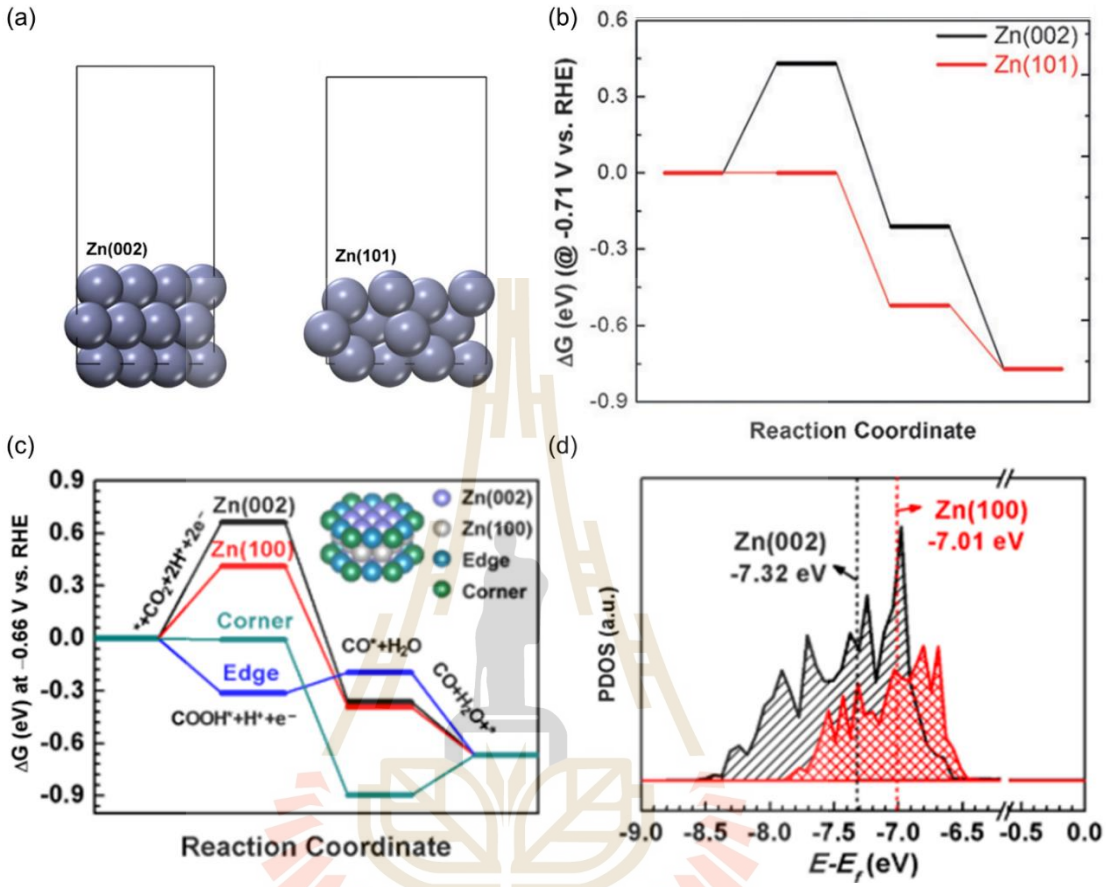

Figure 2.4 The Zn slab models with different facets of (002) and (101) (a); free-energy diagrams for CO_2RR to CO on Zn (002) and Zn (101) at −0.71 V (b) (Won et al., 2016); free energy diagrams for the CO_2RR to CO on Zn(002) and Zn(100) and edge and corner sites at −0.66 V (c), and calculated PDOS of the surface Zn atoms of Zn(002) and Zn(100) facets (d) (Xiao et al., 2020).

2.1.3 Bimetallic Cu-based catalysts

The C_2H_5OH selectivity from CO_2RR is still low on the monometallic Cu catalysts (Nitopi et al., 2019). The bimetallic approach is a promising strategy for improving the C_2H_5OH selectivity (Karapinar, Creissen, Rivera de la Cruz, Schreiber, and Fontecave, 2021; Nitopi et al., 2019). For example, Li and co-workers prepared the homogenous bimetallic Cu–Ag catalyst, which achieved a high FE of 41% for C_2H_5OH at −0.67 V vs. RHE (Li et al., 2019). The solid solution Cu–Ag alloy generated different active sites (see **Figure 2.5(a, b)**) that stabilize the *HCCHOH intermediate of the CO_2RR pathway to C_2H_5OH as shown in **Figure 2.5(c)** (Li et al., 2019). Lv and co-workers revealed that the synthesized Cu–Ag solid–solution alloy showed high selectivity towards C_2H_5OH with the FE of 81% at −0.67 V vs. RHE (Lv et al., 2020). The Ag induces the electron transfer from Cu to Ag in the solid solution Cu–Ag alloy, as demonstrated in **Figure 2.5(d)**. The generated electron–deficient Cu site stabilizes $*CH_3CHO$ intermediate of the C_2H_5OH pathway (ΔG_5) compared with $*C_2H_4$ + *O of the C_2H_4 path, favoring the C_2H_5OH production as shown in **Figure 2.5(d)** (Lv et al., 2020). These works demonstrate that the second metal effect on the CO_2RR of the bimetallic Cu catalyst is beyond a tandem catalytic process, as shown in the tuned electronic and geometrical properties.

Apart from the homogenous alloy, the phase-separated bimetallic Cu-based catalysts also showed promising performance for high selective CO_2RR. Ma and co-workers showed that the phase-separated Cu–Pd structure produced C_2 products higher than the homogenous Cu–Pd alloy with a higher C_2H_4 FE than C_2H_5OH as shown in **Figure 2.6(a, b)** (Ma et al., 2017). **Figure 2.6(c)** showed that the interface site of the phase-separated Cu–Pd affects the C–C coupling reaction, improving C_2 production (Li, Tian, and Chen, 2021). For the C_2H_5OH production, Ting and co-workers found that the phase-separated Cu–Ag showed the selectivity of CO_2 reduction to C_2H_5OH, as shown in **Figure 2.7(a)**. Their theoretical study revealed that the spillover of *CO intermediate on the Ag cluster to Cu sites is an exergonic reaction with a low energy barrier (see **Figure 2.7(b)**) (Ting et al., 2020). Then, the C–C coupling and late–stage reduction reactions will proceed on the Cu(111) surface model (Ting et al., 2020). The catalyst favors the coupling of *CO–*CH and *CO–$*CH_2$, leading to C_2H_5OH production, as shown in **Figure 2.7(c, d)** (Ting et al., 2020). These works demonstrate that the

bimetallic Cu-based catalysts with the phase-separated structure are excellent catalyst candidates for improved CO_2RR selectivity towards C_2H_4 and C_2H_5OH.

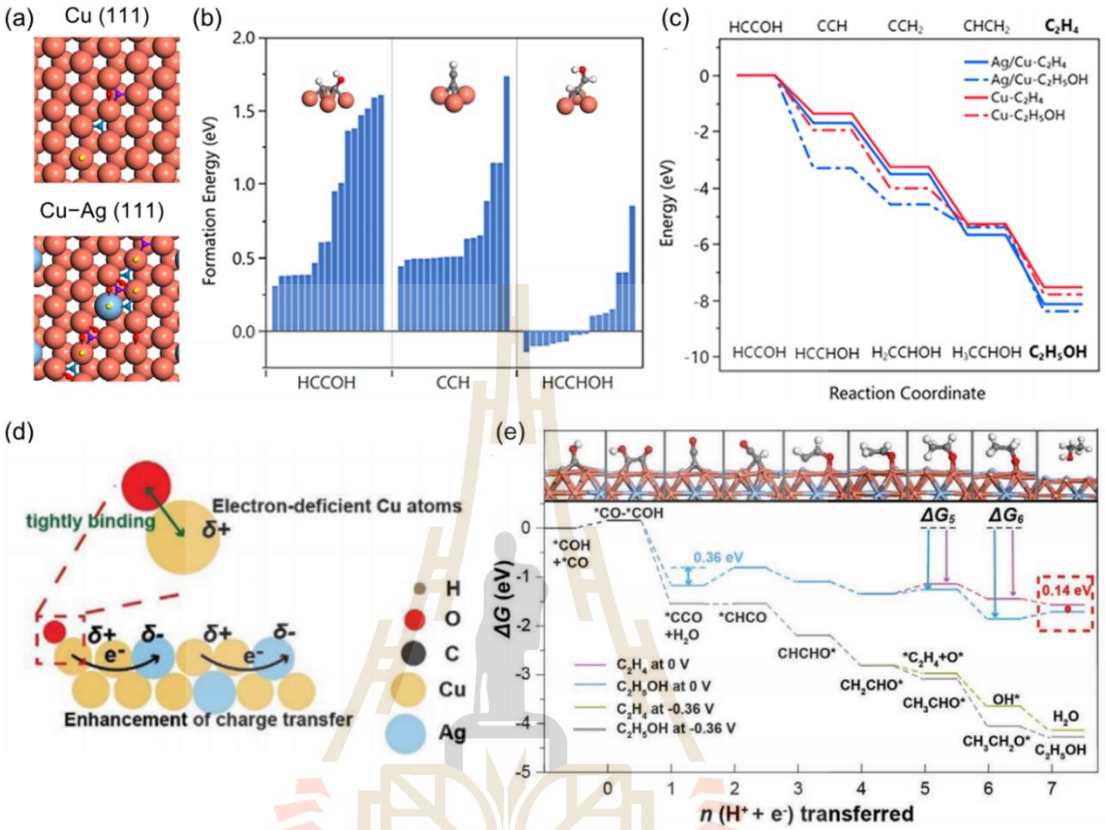

Figure 2.5 Possible actives sites on Cu and Ag/Cu (a); formation energies of important intermediates: *HCCOH, *CCH, and *HCCHOH (b); the energy profile for *HCCOH reduction to C_2H_4 and C_2H_5OH at Cu and Ag/Cu sites (c) (Li et al., 2019); schematic of charge transfer mechanism on the Cu–Ag alloy (d); the energy profile of the reduction of *COH + *CO to C_2H_4 and C_2H_5OH (e) (Lv et al., 2020).

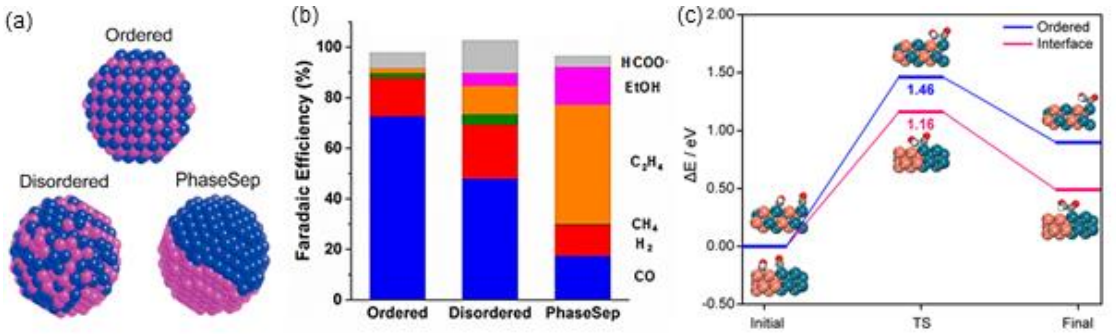

Figure 2.6 Schematic of orders, disordered, phase separated Cu–Pd catalysts (a) and their FEs of products from CO_2RR (b) (Ma et al., 2017); the energy profile for the *CO–*CHO coupling reaction (d) and the energy profile of the reduction of CO_2RR to C_2H_4 (e) at orders and interface sites of Cu–Pd catalysts (Li et al., 2021).

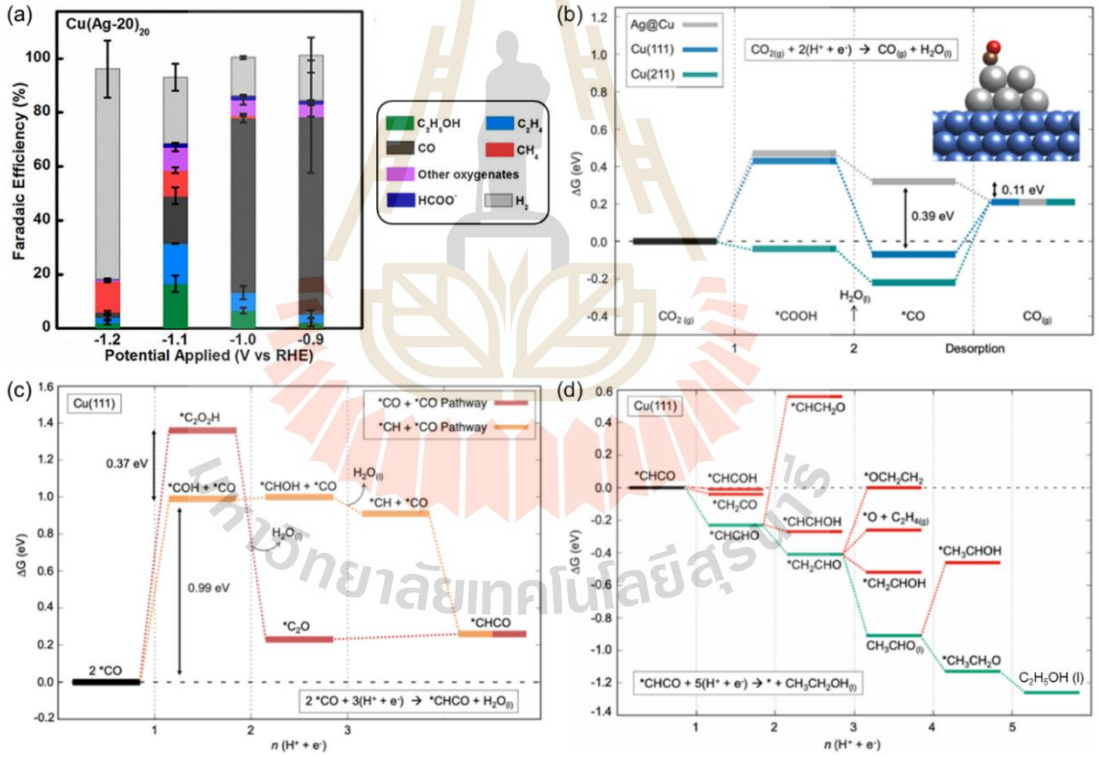

Figure 2.7 FEs of various products from CO_2RR of the Cu–Ag catalyst (a); the energy profile of CO_2 reduction to CO (b); the coupling reactions of *CO–*CO and *CO–*CH on Cu(111) (c); the energy profile for the *CHCO reduction to C_2H_5OH at 0 V (d) (Ting et al., 2020).

2.1.4 Bimetallic Cu–Zn catalysts

For the phase-separated Cu–Zn catalysts, Ren and co-workers fabricated various compositions of the phase-separated Cu–Zn catalysts. They found that the Cu_{80}–Zn_{20} catalyst yielded the highest efficiency for producing C_2H_5OH: 29.1% FE of C_2H_5OH at −1.05 V vs. RHE, as shown in **Figure 2.8(a)** (Ren et al., 2016). The Cu showed a lower FE of 11.3% for C_2H_5OH than the Cu_{80}–Zn_{20}, as exhibited in **Figure 2.8(b)** (Ren et al., 2016). Moreover, they found that the C_2H_5OH/C_2H_4 selectivity is dependent on the Zn content: The 25% of Zn is the optimum composition to achieve the maximum FE of C_2H_5OH on the Cu–Zn catalysts (see **Figure 2.8(c)**) (Ren et al., 2016). Considering the experimental evidence, Ren and co-workers proposed the mechanism that Zn will act as the CO promoter, and the produced CO subsequently spills over to Cu sites where the C–C coupling and the further reduction occur to produce C_2 products, as demonstrated in **Figure 2.8(d)** (Ren et al., 2016). Similarly, Juntrapirom and co-workers revealed that the phase-separated Cu–Zn (1:1) catalyst yielded the C_2H_5OH as a major product with FE of 11.4% at −1.05 V vs. RHE compared with the homogenous Cu–Zn alloy (Juntrapirom et al., 2021). Therefore, these works demonstrate that the phase-separated Cu–Zn catalyst shows remarkable performance for selective CO_2RR to C_2H_5OH.

In comparison, several Cu–Zn catalysts show the high selectivity of CO_2RR towards other products such as CO and C_2H_4. Wan and co-workers showed that the phase-separated Cu–Zn catalyst with the ratio of about 1:1 exhibited a FE of 94% for CO at −1.0 V vs. RHE (Wan et al., 2022). Meanwhile, the porous homogenous Cu–Zn (5:8) catalyst exhibited the FE of C_2H_5OH of 46.6 % at −0.8 V vs. RHE (Su et al., 2020). Compared with those of homogeneous Cu–Zn alloys, they exhibited high CO_2RR selectivity towards C_2H_4: FE of 41.1% at −1.1 V vs. RHE for Cu–Zn (3:1) (da Silva et al., 2021); FE of 33.3% at −1.1 V vs. RHE for Cu–Zn (4:1) (Feng et al., 2018); FE of 15.4% at −0.99 V vs. RHE for Cu–Zn (3:1) (Juntrapirom et al., 2021). In addition, some homogeneous Cu–Zn catalysts favored CO production, such as with ratios of 1:9 (Jeon et al., 2019) and (1:10) (Wang et al., 2021). Thus, the selectivity of CO_2RR on Cu–Zn catalysts is sensitive to many factors such as atomic arrangement and composition.

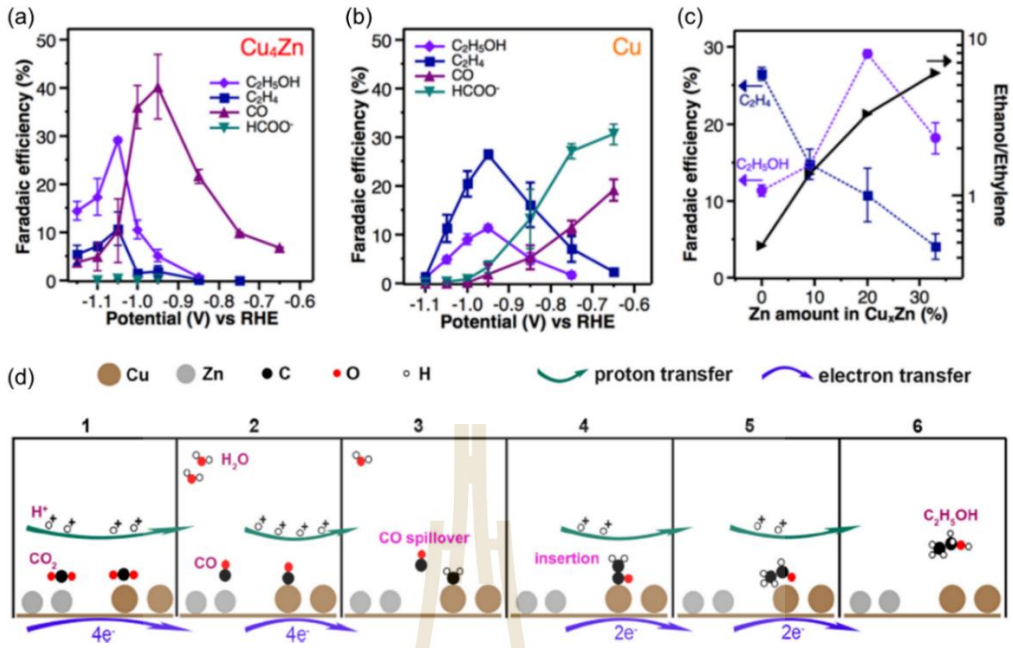

Figure 2.8 Faradaic efficiencies as a function of potential for ethanol, ethylene, carbon monoxide, and $HCOO^-$ from the CO_2RR on the catalysts on (a) Cu and (b) $Cu_{75}–Zn_{25}$; (c) maximum Faradaic efficiencies of ethanol and ethylene and the average FE_{C2H5OH}/FE_{C2H4} ratio (calculated based on the ratios measured at different potentials) on the Cu–Zn catalysts; (d) proposed mechanism for CO_2RR to ethanol on the Cu–Zn catalysts (Ren et al., 2016).

2.2 Phase-separated Cu–Zn models

For the phase-separated models of bimetallic Cu catalysts, Li and co-workers used the model as shown in **Figure 2.9(a)** to understand the CO_2RR selectivity on the phase-separated Cu–Pd catalysts. The Pd atoms replaced half of the Cu atoms in the Cu(211) model to construct the phase-separated Cu–Pd model (Li et al., 2021). Meanwhile, Wan and co-workers modeled the phase-separated Cu–Zn system to study the CO_2RR to CO, as illustrated in **Figure 2.9(b)** (Wan et al., 2022). Interestingly, Ting and co-workers studied the CO_2RR to C_2 products on the Cu–Ag catalysts using the Ag-cluster deposited Cu(111) model (Ting et al., 2020). For the Cu–Zn model, as shown in **Figure 2.9(c)**. From the experiment, Ren and co-workers revealed that the Cu–Zn catalysts show any alloying phase (Ren et al., 2016). Thus, we adopted the cluster deposited Cu(111) as the model for phase-separated Cu–Zn catalysts.

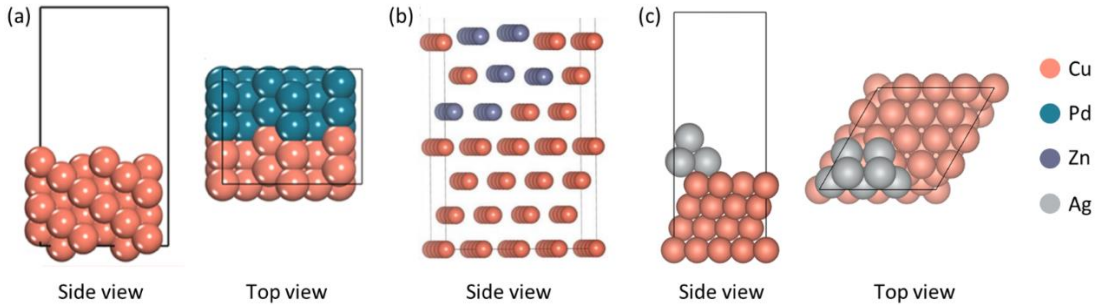

Figure 2.9 Phase-separated models of bimetallic Cu catalysts: (a) Cu–Pd (Li et al., 2021); (b) Cu–Zn (Wan et al., 2022); (c) Cu–Ag (Ting et al., 2020).

Similarly to the Ag-cluster deposited Cu(111) model, Reichenbach and co-workers performed the optimization of Zn-cluster deposited on the Cu(111) model as shown in **Figure 2.10** (Reichenbach, Walter, Moseler, Hammer, and Bruix, 2019). They found that the Zn clusters with the sizes (N) of 3–7 and 9 are flat on Cu(111) surfaces. The Zn atoms locate at hollow sites the Cu(111) (Reichenbach et al., 2019). The most high-coordinated Zn atom at the center of the cluster is up-lifted because Zn atoms reorganize to fit into the Cu(111) hollow sites while maximizing the Zn–Zn interactions (Reichenbach et al., 2019). For the size of the Zn cluster, Aguado and co-workers studied the global minimum structures of the Zn_N^- cluster anions provided by photoemission spectra (Aguado, Vega, Lebon, and von Issendorff, 2018). The system contained Zn's anion, neutral, and cation forms clustering up to 73 atoms. For the neutral cluster, the clusters with N = 10, 17, 20, 29, 32, 35, 46, 54, 65, and 69–71 have enhanced stability compared to that average, as shown in **Figure 2.11**. From the results, the 10-atom Zn cluster is one of sizes that showed relatively high stability than the average. Thus, we selected the 10-atom Zn cluster to represent the Zn in the phase-separated Cu–Zn catalysts.

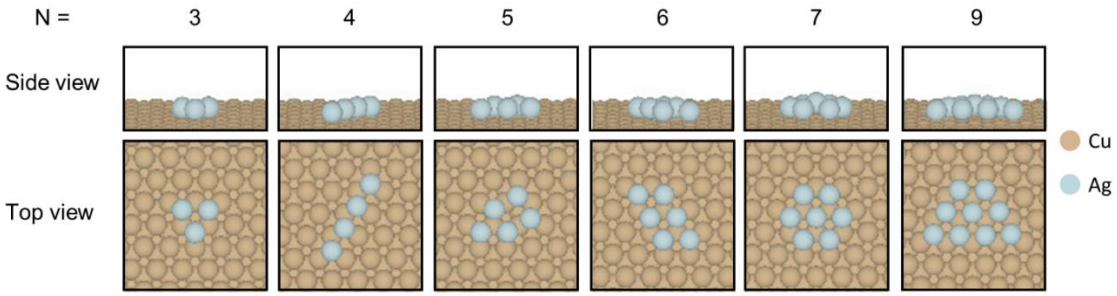

Figure 2.10 Global minima structures of Zn_N–Cu(111) for N = 3–7 and 9 (Reichenbach et al., 2019).

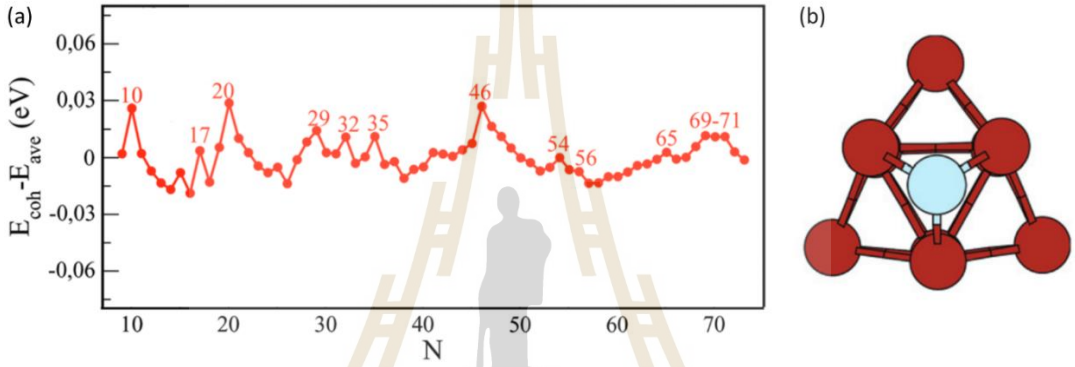

Figure 2.11 The cohesive energies, referenced to energy average of the neutral clusters with the indicators for the cluster showing the enhanced stability (a); the Zn_{10} structure (b). Blue color is additionally used to highlight that a structure is obtained by adding several atoms to the Zn_9 cluster. Adopted from the work of (Aguado et al., 2018).

2.3 References

Aguado, A., Vega, A., Lebon, A., and von Issendorff, B. (2018). Are zinc clusters really amorphous? A detailed protocol for locating global minimum structures of clusters. *Nanoscale, 10*(40), 19162-19181.

Cheng, T., Xiao, H., and Goddard, W. A. (2015). Free-energy barriers and reaction mechanisms for the electrochemical reduction of CO on the Cu(100) surface, including multiple layers of explicit solvent at pH 0. *The Journal of Physical Chemistry Letters, 6*(23), 4767-4773.

Chernyshova, I. V., Somasundaran, P., and Ponnurangam, S. (2018). On the origin of the elusive first intermediate of CO_2 electroreduction. *Proceedings of the National Academy of Sciences, 115*(40), E9261-E9270.

da Silva, A. H. M., Raaijman, S. J., Santana, C. S., Assaf, J. M., Gomes, J. F., and Koper, M. T. M. (2021). Electrocatalytic CO_2 reduction to C_{2+} products on Cu and Cu_xZn_y electrodes: Effects of chemical composition and surface morphology. *Journal of Electroanalytical Chemistry, 880*, 114750.

Dong, H., Li, Y., and Jiang, D.-e. (2018). First-principles insight into electrocatalytic reduction of CO_2 to CH_4 on a copper nanoparticle. *The Journal of Physical Chemistry C, 122*(21), 11392-11398.

Feaster, J. T., Shi, C., Cave, E. R., Hatsukade, T., Abram, D. N., Kuhl, K. P., Hahn, C., Nørskov, J. K., and Jaramillo, T. F. (2017). Understanding selectivity for the electrochemical reduction of carbon dioxide to formic acid and carbon monoxide on metal electrodes. *ACS Catalysis, 7*(7), 4822-4827.

Feng, Y., Li, Z., Liu, H., Dong, C., Wang, J., Kulinich, S. A., and Du, X. (2018). Laser-prepared CuZn alloy catalyst for selective electrochemical reduction of CO_2 to ethylene. *Langmuir, 34*(45), 13544-13549.

Garza, A. J., Bell, A. T., and Head-Gordon, M. (2018). Mechanism of CO_2 reduction at copper surfaces: Pathways to C_2 products. *ACS Catalysis, 8*(2), 1490-1499.

Hori, Y., Takahashi, R., Yoshinami, Y., and Murata, A. (1997). Electrochemical reduction of CO at a copper electrode. *The Journal of Physical Chemistry B, 101*(36), 7075-7081.

Hori, Y., Wakebe, H., Tsukamoto, T., and Koga, O. (1994). Electrocatalytic process of CO selectivity in electrochemical reduction of CO_2 at metal electrodes in aqueous media. *Electrochimica Acta, 39*(11), 1833-1839.

Hussain, J., Jónsson, H., and Skúlason, E. (2016). Faraday efficiency and mechanism of electrochemical surface reactions: CO_2 reduction and H_2 formation on Pt(111). *Faraday Discussions, 195*(0), 619-636.

Hussain, J., Jónsson, H., and Skúlason, E. (2018). Calculations of product selectivity in electrochemical CO_2 reduction. *ACS Catalysis, 8*(6), 5240-5249.

Hussain, J., Skúlason, E., and Jónsson, H. (2015). Computational study of electrochemical CO_2 reduction at transition metal electrodes. *Procedia Computer Science, 51*, 1865-1871.

Jeon, H. S., Timoshenko, J., Scholten, F., Sinev, I., Herzog, A., Haase, F. T., and Roldan Cuenya, B. (2019). Operando insight into the correlation between the structure and composition of CuZn nanoparticles and their selectivity for the electrochemical CO_2 reduction. *Journal of the American Chemical Society, 141*(50), 19879-19887.

Juntrapirom, S., Santatiwongchai, J., Watwiangkham, A., Suthirakun, S., Butburee, T., Faungnawakij, K., Chakthranont, P., Hirunsit, P., and Rungtaweevoranit, B. (2021). Tuning CuZn interfaces in metal–organic framework-derived electrocatalysts for enhancement of CO_2 conversion to C_2 products. *Catalysis Science & Technology, 11*(24), 8065-8078.

Kang, M. P. L., Kolb, M. J., Calle-Vallejo, F., and Yeo, B. S. (2022). The role of undercoordinated sites on zinc electrodes for CO_2 reduction to CO. *Advanced Functional Materials*.

Karapinar, D., Creissen, C. E., Rivera de la Cruz, J. G., Schreiber, M. W., and Fontecave, M. (2021). Electrochemical CO_2 reduction to ethanol with copper-based catalysts. *ACS Energy Letters, 6*(2), 694-706.

Kortlever, R., Shen, J., Schouten, K. J. P., Calle-Vallejo, F., and Koper, M. T. M. (2015). Catalysts and reaction pathways for the electrochemical reduction of carbon dioxide. *The Journal of Physical Chemistry Letters, 6*(20), 4073-4082.

Kuhl, K. P., Cave, E. R., Abram, D. N., and Jaramillo, T. F. (2012). New insights into the electrochemical reduction of carbon dioxide on metallic copper surfaces. *Energy & Environmental Science, 5*(5), 7050-7059.

Li, Y., Tian, Z., and Chen, L. (2021). Theoretical understanding of the interface effect in promoting electrochemical CO_2 reduction on Cu–Pd alloys. *The Journal of Physical Chemistry C, 125*(39), 21381-21389.

Li, Y. C., Wang, Z., Yuan, T., Nam, D.-H., Luo, M., Wicks, J., Chen, B., Li, J., Li, F., de Arquer, F. P. G., Wang, Y., Dinh, C.-T., Voznyy, O., Sinton, D., and Sargent, E. H. (2019). Binding site diversity promotes CO_2 electroreduction to ethanol. *Journal of the American Chemical Society, 141*(21), 8584-8591.

Li, Y. H., Liu, P. F., Li, C., and Yang, H. G. (2018). Sharp-tipped zinc nanowires as an efficient electrocatalyst for carbon dioxide reduction. *Chemistry – A European Journal, 24*(58), 15486-15490.

Liu, X., Schlexer, P., Xiao, J., Ji, Y., Wang, L., Sandberg, R. B., Tang, M., Brown, K. S., Peng, H., Ringe, S., Hahn, C., Jaramillo, T. F., Nørskov, J. K., and Chan, K. (2019). pH effects on the electrochemical reduction of CO_2 towards C_2 products on stepped copper. *Nature Communications, 10*(1), 32.

Lum, Y., Cheng, T., Goddard, W. A., and Ager, J. W. (2018). Electrochemical CO reduction builds solvent water into oxygenate products. *Journal of the American Chemical Society, 140*(30), 9337-9340.

Luo, W., Nie, X., Janik, M. J., and Asthagiri, A. (2016). Facet dependence of CO_2 reduction paths on Cu electrodes. *ACS Catalysis, 6*(1), 219-229.

Luo, W., Zhang, Q., Zhang, J., Moioli, E., Zhao, K., and Züttel, A. (2020). Electrochemical reconstruction of ZnO for selective reduction of CO_2 to CO. *Applied Catalysis B: Environmental, 273*, 119060.

Lv, X., Shang, L., Zhou, S., Li, S., Wang, Y., Wang, Z., Sham, T.-K., Peng, C., and Zheng, G. (2020). Electron-deficient Cu sites on Cu_3Ag_1 catalyst promoting CO_2 electroreduction to alcohols. *Advanced Energy Materials, 10*(37), 2001987.

Ma, S., Sadakiyo, M., Heima, M., Luo, R., Haasch, R. T., Gold, J. I., Yamauchi, M., and Kenis, P. J. A. (2017). Electroreduction of carbon dioxide to hydrocarbons using bimetallic Cu–Pd catalysts with different mixing patterns. *Journal of the American Chemical Society, 139*(1), 47-50.

Montoya, J. H., Shi, C., Chan, K., and Nørskov, J. K. (2015). Theoretical insights into a CO dimerization mechanism in CO_2 electroreduction. *The Journal of Physical Chemistry Letters, 6*(11), 2032-2037.

Nie, X., Esopi, M. R., Janik, M. J., and Asthagiri, A. (2013). Selectivity of CO_2 reduction on copper electrodes: The role of the kinetics of elementary steps. *Angewandte Chemie International Edition, 52*(9), 2459-2462.

Nitopi, S., Bertheussen, E., Scott, S. B., Liu, X., Engstfeld, A. K., Horch, S., Seger, B., Stephens, I. E. L., Chan, K., Hahn, C., Nørskov, J. K., Jaramillo, T. F., and Chorkendorff, I. (2019). Progress and perspectives of electrochemical CO_2 reduction on copper in aqueous electrolyte. *Chemical Reviews, 119*(12), 7610-7672.

Ou, L., and Chen, J. (2020). Theoretical insights into the effect of the overpotential on CO electroreduction mechanisms on Cu(111): Regulation and application of electrode potentials from a CO coverage-dependent electrochemical model. *Physical Chemistry Chemical Physics, 22*(1), 62-73.

Ou, L., Chen, J., Chen, Y., and Jin, J. (2019). Mechanistic study on Cu-catalyzed CO_2 electroreduction into CH_4 at simulated low overpotentials based on an improved electrochemical model. *Physical Chemistry Chemical Physics, 21*(28), 15531-15540.

Peterson, A. A., Abild-Pedersen, F., Studt, F., Rossmeisl, J., and Nørskov, J. K. (2010). How copper catalyzes the electroreduction of carbon dioxide into hydrocarbon fuels. *Energy & Environmental Science, 3*(9), 1311-1315.

Piqué, O., Viñes, F., Illas, F., and Calle-Vallejo, F. (2020). Elucidating the structure of ethanol-producing active sites at oxide-derived Cu electrocatalysts. *ACS Catalysis, 10*(18), 10488-10494.

Qin, B., Li, Y., Fu, H., Wang, H., Chen, S., Liu, Z., and Peng, F. (2018). Electrochemical reduction of CO_2 into tunable syngas production by regulating the crystal facets of earth-abundant Zn catalyst. *ACS Applied Materials & Interfaces, 10*(24), 20530-20539.

Reichenbach, T., Walter, M., Moseler, M., Hammer, B., and Bruix, A. (2019). Effects of gas-phase conditions and particle size on the properties of Cu(111)-supported Zn_yO_x particles revealed by global optimization and ab initio thermodynamics. *The Journal of Physical Chemistry C, 123*(51), 30903-30916.

Ren, D., Ang, B. S.-H., and Yeo, B. S. (2016). Tuning the selectivity of carbon dioxide electroreduction toward ethanol on oxide-derived Cu_xZn catalysts. *ACS Catalysis, 6*(12), 8239-8247.

Sandberg, R. B., Montoya, J. H., Chan, K., and Nørskov, J. K. (2016). CO-CO coupling on Cu facets: Coverage, strain and field effects. *Surface Science, 654*, 56-62.

Santatiwongchai, J., Faungnawakij, K., and Hirunsit, P. (2021). Comprehensive mechanism of CO_2 electroreduction toward ethylene and ethanol: The solvent effect from explicit water–Cu(100) interface models. *ACS Catalysis, 11*(15), 9688-9701.

Su, X., Sun, Y., Jin, L., Zhang, L., Yang, Y., Kerns, P., Liu, B., Li, S., and He, J. (2020). Hierarchically porous Cu/Zn bimetallic catalysts for highly selective CO_2 electroreduction to liquid C_2 products. *Applied Catalysis B: Environmental, 269*, 118800.

Takatsuji, Y., Morimoto, M., Nakatsuru, Y., and Haruyama, T. (2022). Anodized Zn electrode for formate selectivity during the electrochemical reduction of CO_2 at low applied potential. *Electrochemistry Communications, 138*.

Ting, L. R. L., Piqué, O., Lim, S. Y., Tanhaei, M., Calle-Vallejo, F., and Yeo, B. S. (2020). Enhancing CO_2 electroreduction to ethanol on copper–silver composites by opening an alternative catalytic pathway. *ACS Catalysis, 10*(7), 4059-4069.

Todorova, T. K., Schreiber, M. W., and Fontecave, M. (2020). Mechanistic understanding of CO_2 reduction reaction (CO_2RR) toward multicarbon products by heterogeneous copper-based catalysts. *ACS Catalysis, 10*(3), 1754-1768.

Wan, L., Zhang, X., Cheng, J., Chen, R., Wu, L., Shi, J., and Luo, J. (2022). Bimetallic Cu–Zn catalysts for electrochemical CO_2 reduction: Phase-separated versus core–shell distribution. *ACS Catalysis, 12*(5), 2741-2748.

Wang, L., Peng, H., Lamaison, S., Qi, Z., Koshy, D. M., Stevens, M. B., Wakerley, D., Zamora Zeledón, J. A., King, L. A., Zhou, L., Lai, Y., Fontecave, M., Gregoire, J., Abild-Pedersen, F., Jaramillo, T. F., and Hahn, C. (2021). Bimetallic effects on Zn-Cu electrocatalysts enhance activity and selectivity for the conversion of CO_2 to CO. *Chem Catalysis, 1*(3), 663-680.

Won, D. H., Shin, H., Koh, J., Chung, J., Lee, H. S., Kim, H., and Woo, S. I. (2016). Highly efficient, selective, and stable CO_2 electroreduction on a hexagonal Zn catalyst. *Angewandte Chemie International Edition, 55*(32), 9297-9300.

Xiao, J., Gao, M.-R., Liu, S., and Luo, J.-L. (2020). Hexagonal Zn nanoplates enclosed by Zn(100) and Zn(002) facets for highly selective CO_2 electroreduction to CO. *ACS Applied Materials & Interfaces, 12*(28), 31431-31438.

Zhang, T., Li, X., Qiu, Y., Su, P., Xu, W., Zhong, H., and Zhang, H. (2018). Multilayered Zn nanosheets as an electrocatalyst for efficient electrochemical reduction of CO_2. *Journal of Catalysis, 357*, 154-162.

Zhang, T., Zhong, H., Qiu, Y., Li, X., and Zhang, H. (2016). Zn electrode with a layer of nanoparticles for selective electroreduction of CO_2 to formate in aqueous solutions. *Journal of Materials Chemistry A, 4*(42), 16670-16676.

Zhang, W., Hu, Y., Ma, L., Zhu, G., Wang, Y., Xue, X., Chen, R., Yang, S., and Jin, Z. (2018). Progress and perspective of electrocatalytic CO_2 reduction for renewable carbonaceous fuels and chemicals. *Advanced Science, 5*(1), 1700275.

CHAPTER III
DENSITY FUNCTIONAL THEORY WITH PERIODIC BOUNDARY CONDITIONS AND COMPUTATIONAL HYDROGEN ELECTRODE MODEL

Density functional theory (DFT) is an efficient method that has been applied to theoretically study various problems in physical science and engineering. This method was developed to solve the Schrödinger's equation which is the fundamental equation for describing the quantum behavior of atoms and molecules in quantum mechanics. The time-independent Schrödinger equation is:

$$\hat{H}\Psi = E\Psi \tag{3.1}$$

where $\hat{H}$ denotes as the Hamiltonian operator, Ψ is the wave function, and E is the energy of system. The Born–Oppenheimer approximation was applied for the motion of nuclei and electron. However, solving Schrödinger's equation in complex systems is still computationally difficult because of multi-dimensionality and many-body problems.

From the Schrödinger's equation, we will first give the introduction to DFT method and its methodology for the application of the system with a periodic-boundary conditions (Jensen 2007; Koch and Holthausen 2000; Sholl and Steckel 2009) in **Section 3.1**. Then, we will introduce the concept of computational hydrogen electrode (CHE) model (Nørskov et al. 2004) in **Section 3.2**. This model is a simple yet efficient method that can utilize DFT to study the electrocatalysis systems.

3.1 Density functional theory

From the challenge in solving the Schrödinger's equation, the Density functional theory (DFT) was introduced as the powerful tool to solve those problems by using electron density approach instead of the wave function approach for

electrons. This reduces the complexity while retaining its accuracy as those calculations from the Schrödinger's equation. The foundations of DFT rest on the Hohenberg-Kohn theorems and the derivation of set of equations called the Kohn-Sham Equations which will be explained later in this section.

3.1.1 The Hohenberg-Kohn theorems

The first theorem states (Hohenberg and Kohn, 1964) that "The ground-state energy of Schrödinger's equation is a unique functional of the electron density". This provides the one-to-one mapping between the ground-state wave function and the ground-state electron density. The electron density $n(r)$ can be written in terms of the wave function $\psi_i(r)$. The ground-state electron density represents all electron properties of the ground state. Then, the ground-state energy E can be expressed as $E[n(r)]$. The $n(r)$ functional is three spatial variables, while the wave function is the function of 3N variables. Thus, this theorem solves the multi-dimensionality problem of wave function. For example, the individual electron density can be written as

$$n(r) = 2\sum_i \psi_i^*(r)\psi_i(r). \tag{3.2}$$

The second Hohenberg-Kohn theorem (Hohenberg and Kohn, 1964) states that "The electron density that minimizes the energy of the overall functional is the true electron density corresponding to the full solution of the Schrödinger equation". If we could find a functional of the electron density $E[n(r)]$ that gives the exact ground-state energy E_0, then the results will be accurate as from the Schrödinger's equation. Unfortunately, the universal functional is yet to be described, therefore approximations must be made.

3.1.2 The Kohn-Sham equation

To make DFT computational feasible, Kohn and Sham (Kohn and Sham, 1965) introduced a simplification method to perform DFT. Instead of the term of electron-electron interaction in many-body problems, Kohn-Sham introduced that the electrons interact with an effective potential $V_{eff}(r)$. The Kohn-Shan equations are

$$\left[\frac{h^2}{2m}\nabla^2 + V_{eff}(r)\right]\psi_j(r) = \varepsilon_j\psi_j(r). \tag{3.3}$$

where $V_{eff}(r)$ is the effective potential. The effective potential is a set of function of $n(r)$, then Kohn–Sham equations have the form as

$$\left[\frac{h^2}{2m}\nabla^2 + V(r) + V_H(r) + V_{XC}(r)\right]\psi_j(r) = \varepsilon_j\psi_j(r). \quad (3.4)$$

$V(r)$ is the interaction energy between each electron and the collection of atomic nuclei. $V_H(r)$ is the Hartree potential for Coulomb repulsion between the electrons and is defined as

$$V_H(r) = e^2 \int \frac{n(r')}{|r-r'|} d^3r'. \quad (3.5)$$

$V_{XC}(r)$ is the exchange–correlation contribution and is defined as a functional derivative:

$$V_{XC}(r) = \frac{\delta E_{XC}(r)}{\delta}, \quad (3.6)$$

Where $E_{XC}(r)$ is the exchange–correlation functional that include all the quantum mechanical effects that are not included previously.

To obtain the ground-state electron density, there is an iteration method called a self-consistent field (SCF) method as shown in **Figure 3.1.**

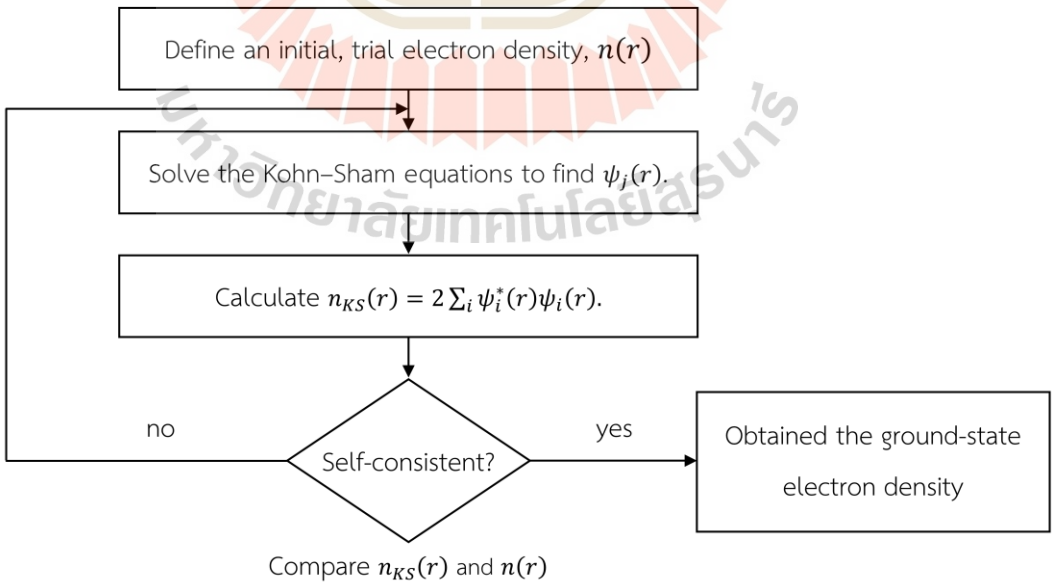

Figure 3.1 A flowchart showing a self-consistent field method for solving the Kohn-Sham equation.

3.1.3 Exchange-correlation functional

The DFT accuracy depends on the exchange–correlation functional $E_{XC}(r)$ which accounts for the complex interactions of electrons with each other and their self-interaction. Defining $E_{XC}(r)$ is challenging for DFT calculations since the universal $E_{XC}(r)$ is still unknown. Fortunately, there is the exact $E_{XC}(r)$ for the uniform electron gas called the LDA (local density approximation).The $E_{XC}^{LDA}(r)$ can be written in the simple form:

$$E_{XC}^{LDA}(r) = \int \varepsilon_{XC}^{LDA}\big(n(r)\big)\, dr. \tag{3.7}$$

Here, ε_{XC}^{LDA} is the exchange-correlation energy per particle of a uniform electron gas of density $n(r)$. From the LDA, the spin-polarized form can be called local spin-density approximation (LSDA), and it is defined as

$$E_{XC}^{LSDA}(r) = \int \varepsilon_{XC}^{LSDA}\Big(n_{\alpha}(r), n_{\beta}(r)\Big)\, dr, \tag{3.8}$$

where α or β indicates the spin difference of electrons.

In the case of solids, there is one of the popular functionals using a generalized gradient approximation (GGA) called the Perdew–Burke–Ernzerhof functional (PBE) (Ernzerhof and Scuseria, 1999; Hammer, Hansen, and Nørskov, 1999; Wan, Wang, Liu, and Liang 2021). The GGA method is a non-local method which includes a variable of the first derivative of the density, and it requires the integration of the Fermi and Coulomb holes. The GGA functional can be written as

$$E_{XC}^{GGA}(r) = \int \varepsilon_{XC}^{GGA}\Big(n_{\alpha}(r), n_{\beta}(r), \nabla n_{\alpha}(r), \nabla n_{\beta}(r)\Big)\, dr, \tag{3.9}$$

where f is an exchange-correlation energy per particle that depends on the spin densities and their gradients, and $\nabla n_{\alpha\ or\ \beta}(r)$ is the gradient of electron density $n_{\alpha\ or\ \beta}(r)$.

For PBE (Ernzerhof and Scuseria, 1999; Hammer et al., 1999; Wan et al. 2021), it has been revised in the integration term of the Fermi and Coulomb holes with the Taylor-like expansion. First, the $\varepsilon_{XC}^{PBE}(r)$ can be written in term of the exchange $\varepsilon_{X}^{PBE}(r)$ and correlation energies:

$$\varepsilon_{XC}^{PBE}(r) = \varepsilon_{X}^{PBE}(r) + \varepsilon_{C}^{PBE}(r). \tag{3.10}$$

Then, the exchange part is written as an enhancement factor $F^{PBE}(x)$ multiplied onto the LSDA functional:

$$\begin{aligned} \varepsilon_X^{PBE}(r) &= \varepsilon_X^{LDA} F^{PBE}(x) \\ F^{PBE}(x) &= 1 + a - \frac{a}{1+bx^2} \\ x &= \frac{|\nabla n(r)|}{n(r)^{\frac{4}{3}}}. \end{aligned} \tag{3.11}$$

Besides, the enhancement factor was also added to the correlation part, and it can be written as

$$\begin{aligned} \varepsilon_C^{PBE}(r) &= \varepsilon_C^{LDA} + H(t) \\ H(t) &= c f_3^3 \ln\left[1 + dt^2\left(\frac{1+At^2}{1+At^2+1+A^2t^4}\right)\right] \\ A &= d[exp\left(-\frac{\varepsilon_C^{LDA}}{c f_3^3}\right) - 1]^{-1} \\ f_3(\zeta) &= \frac{1}{2}\left[(1+\zeta)^{\frac{2}{3}} + (1-\zeta)^{\frac{2}{3}}\right] \\ t &= \left[2(3\pi^3)^{\frac{1}{3}} f_3\right]^{-1} x \\ \zeta &= \frac{n_\alpha(r) - n_\beta(r)}{n_\alpha(r) + n_\beta(r)}. \end{aligned} \tag{3.12}$$

The a, b, c, and d are fitting parameters obtained from physical constraints, and ζ is functions indicating the spin polarization.

Apart from the PBE, the revised version of PBE functional (RPBE) for periodic systems has been introduced (Hammer et al., 1999). and in this work, F_X^{PBE} is written similar to (3.11) as shown below

$$\begin{aligned} F^{PBE}(s) &= 1 + \kappa - \frac{\kappa}{1+\frac{\mu s^2}{\kappa}} \\ s &= \frac{|\nabla n(r)|}{2(3\pi^2)^{\frac{1}{3}} n(r)^{\frac{4}{3}}}, \end{aligned} \tag{3.13}$$

where μ and κ are the constants. The exchange enhancement factor of the RPBE F_X^{RPBE} is written as

$$F^{RPBE}(s) = 1 + \kappa\left(1 - e^{-\frac{\mu s^2}{\kappa}}\right). \tag{3.14}$$

It has been stated that RPBE improved performance for the estimation of adsorption energetics on the metal surfaces (Hammer et al., 1999).

3.1.4 Plane-wave basis sets, energy cutoffs, and pseudopotentials

The periodic system is the system with the cell which is repeated periodically in space called the supercell. To solve the Schrödinger equation of this system, Bloch's theorem states that

$$\psi_k(r) = \exp(i\mathbf{k}\cdot\mathbf{r})\, u_{\mathrm{k}}(\mathbf{r}), \tag{3.15}$$

Where $u_{\mathrm{k}}(\mathbf{r})$ is periodic in space, and the functions $\exp(i\mathbf{k}\cdot\mathbf{r})$ are called plane waves. Here, $\mathbf{r}$ is the vector in real space, and $\mathbf{k}$ is the vector in recipocal space. This solves the mathematical problems of DFT for the periodic system.

The periodicity of $u_{\mathrm{k}}(\mathbf{r})$ can be expanded as

$$u_{\mathrm{k}}(\mathbf{r}) = \sum_{\mathbf{G}} c_{\mathbf{G}} \exp[i\mathbf{G}\cdot\mathbf{r}], \tag{3.16}$$

where $\mathbf{G}$ is the set of vectors in reciprocal space. E_{cut} is the kinetic energy cutoff that is introduced as the practical solutions of the Schrödinger equation as

$$E_{\mathrm{cut}} = \frac{h^2}{2m} G_{\mathrm{cut}}^2. \tag{3.17}$$

Then, the equation will be written as

$$\psi_k(r) = \sum_{|\mathbf{G}+\mathbf{k}|<G_{\mathrm{cut}}} c_{\mathbf{k}+\mathbf{G}} \exp[i(\mathbf{k}+\mathbf{G})\mathbf{r}]. \tag{3.18}$$

To decrease the computational cost in the DFT calculation, the core electrons are treated as pseudopotials to reduce the number of plane waves. The core electron is the set of electrons that is insignificantly important in defining the chemical and physical properties of materials. These core electrons are replaced by rhe pseudopotential.

The pseudopotial defines the minimum energy cutoff of the system of interests. Among the method definding pseudopotentials, the projector augmented-wave (PAW) method (Blöchl, 1994; Kresse and Joubert, 1999) is a widely used method in current DFT codes. This method gives the results that is in good agreement with the all-electron calculations.

3.1.5 Thermochemistry

To evaluate free energies from DFT calculations, the Gibbs free energy G can be divided into enthalpy H and entropy S term by

$$G = H - TS. \tag{3.19}$$

Here, we considered only vibrational contribution of adsorbates and gasses in the enthalpy term H which can be expressed as follows:

$$H = U_{elec} + U_{vib}, \tag{3.20}$$

where U_{elec} is the total electronic energy obtained by DFT calculations denoted as E_{DFT}, and U_{vib} is a vibrational energy that will be calculated from statistical thermodynamics.

The vibrational energy U_{vib} can be calculated by using the vibrational frequencies v_k of the system for all the normal modes k using the formula:

$$U_{vib} = \sum_K \frac{1}{2} h v_k + \sum_K \left(\frac{h v_k \times e^{-\frac{h v_k}{k_B T}}}{1 - e^{-\frac{h v_k}{k_B T}}} \right), \tag{3.21}$$

where h is the Planck's constant, k_B is the Boltzmann constant, and T the absolute temperature. The term $\sum_K \frac{1}{2} h v_k$ is called a zero-point energy (ZPE), and the later term is considered as the heat capacity correction $\int C_p dT$.

For the entropy term S can be calculated from the vibrational frequencies v_k, so called S_{vib}. This can be calculated from the equation below:

$$S_{vib} = k_B \sum_K \left(\frac{\frac{h v_k}{k_B T} \times e^{-\frac{h v_k}{k_B T}}}{1 - e^{-\frac{h v_k}{k_B T}}} - \ln\left(1 - e^{-\frac{h v_k}{k_B T}}\right) \right). \tag{3.22}$$

3.2 Computational hydrogen electrode model

To construct the energy profile of CO_2 reduction reaction (CO_2RR), we have applied the computational hydrogen electrode (CHE) model (Nørskov et al., 2004). The CHE model is developed according to the standard hydrogen electrode (SHE) which is set to be the reference. The electrode potential is set to be zero at the standard conditions (pH = 0, P(H_2) = 1 atm, and T = 298K).

$$(\mathrm{H}^+ + \mathrm{e}^-) \rightarrow \frac{1}{2} H_2\,(g)$$

In the CHE model, the electron and protons are in thermodynamic equilibrium with that of $\frac{1}{2} H_2\,(g)$. Thus, the chemical potential of $\mathrm{H}^+ + \mathrm{e}^-$ can be replaced by the chemical potential of $\frac{1}{2} H_2\,(g)$:

$$\mu(\mathrm{H}^+ + \mathrm{e}^-) \rightarrow \frac{1}{2}\mu\big(H_2\,(g)\big)$$

The chemical potential is the Gibbs free energy from the DFT calculation. The CHE model can be further applied to the calculation of reaction at different potentials and pH. In this work, all the calculations were performed at 0 V vs. SHE and pH = 0.

The CHE model helps the DFT calculation to study CO_2RR which involves electron-proton transfer steps. The electrical-field effect of adsorption energy is small thus can be neglected. For example, the adsorbed CO intermediate denoted $^*CO$ can be protonated to form an adsorbed $^*CHO$ intermediate as follows:

$$^*CO + (\mathrm{H}^+ + \mathrm{e}^-) \rightarrow {}^*CHO$$

Here, the reaction free energy ΔG_{rxn} is calculated as below:

$$\Delta G_{rxn} = \Delta G(*CHO) - \Delta G(*CO) - \frac{1}{2}\Delta G\big(H_2(g)\big) \qquad (3.23)$$

This solves the difficulty of DFT calculations for electron and proton transfer steps.

Energy barriers of these electron-proton transfer steps are not calculated because they are expected to become smaller with more negative applied potential (Peterson, Abild-Pedersen, Studt, Rossmeisl, and Nørskov, 2010). In addition, the effect of water environment will be included using the implicit solvent model (Mathew, Sundararaman, Letchworth-Weaver, Arias, and Hennig, 2014).

3.3 References

Blöchl, P. E. (1994). Projector augmented-wave method. *Physical Review B, 50*(24), 17953-17979.

Ernzerhof, M., and Scuseria, G. E. (1999). Assessment of the Perdew–Burke–Ernzerhof exchange-correlation functional. *The Journal of Chemical Physics, 110*(11), 5029-5036.

Hammer, B., Hansen, L. B., and Nørskov, J. K. (1999). Improved adsorption energetics within density-functional theory using Revised Perdew-Burke-Ernzerhof functionals. *Physical Review B, 59*(11), 7413-7421.

Hohenberg, P., and Kohn, W. (1964). Inhomogeneous electron gas. *Physical Review, 136*(3B), B864-B871.

Jensen, F. (2007). *Introduction to computational chemistry*: Wiley.

Koch, W., and Holthausen, M. C. (2000). *A chemist's guide to density functional theory*.

Kohn, W., and Sham, L. J. (1965). Self-consistent equations including exchange and correlation effects. *Physical Review, 140*(4A), A1133-A1138.

Kresse, G., and Joubert, D. (1999). From ultrasoft pseudopotentials to the projector augmented-wave method. *Physical Review B, 59*(3), 1758-1775.

Mathew, K., Sundararaman, R., Letchworth-Weaver, K., Arias, T. A., and Hennig, R. G. (2014). Implicit solvation model for density-functional study of nanocrystal surfaces and reaction pathways. *The Journal of Chemical Physics, 140*(8), 084106.

Nørskov, J. K., Rossmeisl, J., Logadottir, A., Lindqvist, L., Kitchin, J. R., Bligaard, T., and Jónsson, H. (2004). Origin of the overpotential for oxygen reduction at a fuel-cell cathode. *The Journal of Physical Chemistry B, 108*(46), 17886-17892.

Peterson, A. A., Abild-Pedersen, F., Studt, F., Rossmeisl, J., and Nørskov, J. K. (2010). How copper catalyzes the electroreduction of carbon dioxide into hydrocarbon fuels. *Energy & Environmental Science, 3*(9), 1311-1315.

Sholl, D. S., and Steckel, J. A. (2009). *Density functional theory : A practical introduction*. Hoboken, N.J.: Wiley Hoboken, N.J.

Wan, Z., Wang, Q.-D., Liu, D., and Liang, J. (2021). Effectively improving the accuracy of PBE functional in calculating the solid band gap via machine learning. *Computational Materials Science, 198*, 110699.

CHAPTER IV

A THEORETICAL STUDY OF THE ROLE OF THE INTERFACE SITES ON SELECTIVE CARBON DIOXIDE REDUCTION TOWARD ETHANOL ON PHASE-SEPARATED COPPER–ZINC CATALYSTS

4.1 Introduction

Electrocatalytic CO_2 reduction reaction (CO_2RR) is among the promising methods for CO_2 conversion to value-added products such as carbon monoxide (CO), methane (CH_4), formic acid (HCOOH), ethylene (C_2H_4), and ethanol (C_2H_5OH) (Birdja et al., 2019; Feaster et al., 2017; Hori, 2008; Hori, Wakebe, Tsukamoto, and Koga, 1994; Jouny, Luc, and Jiao, 2018; 2020; Kuhl et al., 2014). Obtaining C_2 products, in particular ethanol, is desirable since it is an essential feedstock for fuel production, medicine synthesis, and the food industry (Karapinar, Creissen, Rivera de la Cruz, Schreiber, and Fontecave, 2021).

High yield and selectivity of C_2 products, including C_2H_4 and C_2H_5OH, can be obtained using Cu-based bimetallic catalysts (Gawande et al., 2016; Nitopi et al., 2019; Vasileff, Xu, Jiao, Zheng, and Qiao, 2018; Xie et al., 2021; Zhu, Tackett, Chen, and Jiao, 2018). The role of the second metal is beyond a tandem catalytic process. For example, Ag in the Cu–Ag bimetal catalyst plays two roles: (i) it withdraws electrons from Cu leading to electron-deficient Cu sites which help stabilize $*CH_3CHO$ intermediate to further generate C_2H_5OH (Y. C. Li et al., 2019), and (ii) it provides unique active sites that stabilize *HCCHOH intermediate to produce C_2H_5OH (Vasileff et al., 2018). Nevertheless, the C_2H_5OH selectivity is still low for bimetallic Cu-based catalysts (Karapinar et al., 2021; Ren, Ang, and Yeo, 2016; Todorova, Schreiber, and Fontecave, 2020). Therefore, tuning the C_2 selectivity towards C_2H_5OH has been of interest (Garza, Bell, and Head-Gordon, 2018; Kortlever, Shen, Schouten, Calle-Vallejo, and Koper, 2015; Lum, Cheng, Goddard, and Ager, 2018; Santatiwongchai, Faungnawakij, and Hirunsit, 2021).

The structural properties of bimetallic catalysts affect the product selectivity of CO_2RR on Cu-based catalysts, especially the phase-separated structure (Feng et al., 2018; Herzog et al., 2021; Jeon et al., 2019; Juntrapirom et al., 2021; Li, Wu, Lv, Wang, and Wu, 2022; Ma et al., 2017; Su et al., 2020). Ma and co-workers showed that the phase-separated Cu–Pd structure produced C_2 products higher than that of the homogeneous Cu–Pd alloy with higher C_2H_4 selectivity than C_2H_5OH in both forms (Ma et al., 2017). The phase-separated Cu–Pd generates the interface site with different electronic properties than Cu and Pd sites, which may promote C_2 production (Li, Tian, and Chen, 2021). For the C_2H_5OH production, Ting and co-workers found that the phase-separated Cu–Ag showed the selectivity of CO_2RR to C_2H_5OH (Ting et al., 2020). Their theoretical study reveals that spillover of a *CO intermediate from the Ag cluster to Cu sites is an exergonic reaction with a low energy barrier, thus becomes favorable (Ting et al., 2020). Then, the C–C coupling and late-stage reduction reactions could take place on Cu which favors the coupling of *CO–*CH and *CO–*CH_2 to produce C_2H_5OH. These works demonstrate that the bimetallic Cu-based catalysts with the phase-separated structure are promising towards C_2H_5OH selectivity.

Introducing the phase-separated Zn into Cu catalysts showed the enhanced performance of CO_2RR selectively towards C_2H_5OH (Juntrapirom et al., 2021; Ren et al., 2016). Ren and co-workers fabricated various compositions of the phase-separated Cu–Zn catalysts and found that the Cu–Zn catalysts with 25% of Zn yielded the highest efficiency for C_2H_5OH production: 29.1% FE of C_2H_5OH at –1.05 V vs. RHE (Ren et al., 2016). They proposed the mechanism that Zn acts as the CO promoter, and the produced CO subsequently spills over to Cu sites where the C–C coupling and the further reduction occurs to produce C_2 products (Ren et al., 2016). Similarly, Juntrapirom and co-workers revealed that the phase-separated Cu–Zn (1:1) catalyst yielded C_2H_5OH as a major product with the FE of 11.4% at –1.05 V vs RHE (Juntrapirom et al., 2021). Besides, the bimetallic Cu–Zn catalyst is more attractive than the others such as Cu–Ag and Cu–Au because of the cost efficiency. Thus, an in–depth understanding of the structural effect on the CO_2RR selectivity to C_2H_5OH on the Cu–Zn catalyst is essential to the development of Cu-based electrocatalyst design to enhance catalytic activity and selectivity toward C_2H_5OH.

Herein, we theoretically investigate the role of the interface Cu–Zn sites on the phase-separated Cu–Zn catalyst in selective CO_2RR toward C_2H_5OH production. The model includes a Zn cluster deposited on the Cu(111) surface, which contains three types of active sites: Cu, Zn, and interface sites. The CO_2RR pathway towards CO at these active sites was extensively investigated. The reduction to CH_4 was studied comparatively on Cu and interface sites. All possible C–C coupling reactions were explored at the interface sites and Cu sites considering the coupling of *CO–*CO and *CO with other C_1 intermediates presenting in the CH_4 pathways. Finally, the intermediates resulting from the coupling step are reduced to C_2H_5OH and C_2H_4 products. The competitive hydrogen evolution reaction (HER) was also investigated. The results demonstrated the role of the Cu–Zn interface site towards selective C_2H_5OH production.

4.2 Computational details

All calculations were carried out using the spin-polarized density functional theory (DFT) method as implemented in the Vienna ab initio simulation package (VASP version 5.4) (Kresse and Furthmüller, 1996). The projector-augmented-wave (PAW) method was used to treat the ion-electron interactions (Blöchl, 1994; Kresse and Joubert, 1999). The valence-electron wavefunctions were expanded in the plane-wave fashion with the kinetic energy cutoff of 450 eV. The exchange and correlation energy were described using the Revised Perdew-Burke-Ernzerhof (RPBE) functional (Hammer, Hansen, and Nørskov, 1999), which has been applied for mechanistic studies of CO_2RR on various metal surfaces (Garza et al., 2018; Hussain, Jónsson, and Skúlason, 2018; Santatiwongchai et al., 2021). The correction of van der Waals interaction was employed using Grimme's DFT-D3 schemes (Grimme, Antony, Ehrlich, and Krieg, 2010). The effect of water solvent was included using an implicit solvation model as implemented in the VASPsol package (Mathew, Sundararaman, Letchworth-Weaver, Arias, and Hennig, 2014). The convergence of self-consistent field energy was set to 1×10^{-6} eV. The Methfessel-Paxton smearing method (Methfessel and Paxton, 1989) with a smearing width of 0.2 eV was used to treat the partial occupancies (extrapolating total energies to 0 K).

We constructed the phase-separated Cu–Zn model by placing a 10-atom Zn cluster on the 3×3 Cu(111) surface with a slab thickness of three atomic layers. During structural optimization, all atoms were relaxed except for the bottom-most layer, which is fixed at the Cu–Cu bulk distance. A vacuum region of 20 Å and dipole corrections were added along the z direction to correct for spurious interactions between periodic images. The Cu(111) facet was selected because it is the most stable surface. The Zn_{10} cluster was adopted from the previous study as it exhibits relatively high stability (Aguado, Vega, Lebon, and von Issendorff, 2018). Several Zn-adsorbed configurations were considered (**Figure 4.1**) and the most stable configuration was chosen as a model for further computations. A 2 × 2 × 1 k-points Monkhorst-Pack (MP) grid (Monkhorst and Pack, 1976) was used to sample the Brillouin zone. Atomic coordinates were allowed to relax until the force on each atom was lower than 0.03 eV/Å.

In addition, the 2×2 surface of homogeneous Cu–Zn(111) alloy was constructed for comparative studies with the Cu:Zn ratio of 3:1, denoted as homogeneous $Cu_3Zn(111)$. The two bottom layers were fixed during optimization. The vacuum gap of 35 Å was added in the z-direction. The MP (Monkhorst and Pack, 1976) k-point mesh of 4 × 4 × 1 was applied.

To study the Cu–Zn model, the interaction energy $E_{interaction}$ is calculated from the equation:

$$E_{interaction} = E_{Cu+Zn} - (E_{Cu} + E_{Zn}), \quad (4.1)$$

where E_{Cu+Zn} is the total energy of the optimized Cu–Zn structure, the E_{Cu} and the E_{Zn} are the single-point energies of Cu surface and Zn cluster of the optimized Cu–Zn structure, respectively. Adsorption energies of intermediates, E_{ads}, on the surface were calculated as follow:

$$E_{ads} = E_{Surface+Adsorbate} - (E_{Surface} + E_{Adsorbate}), \quad (4.2)$$

where $E_{Surface+Adsorbate}$ is the energy of the adsorbed system; $E_{Surface}$ is the energy of the bare surface; and $E_{Adsorbate}$ is the energy of an isolated adsorbate species in the gas phase.

Free energies of gas-phase molecules and adsorbates, *G*, were calculated as follows:

$$G = E_{DFT} + ZPE + \int C_p dT - TS_{vib}, \quad (4.3)$$

where E_{DFT} is the DFT-computed total energy, ZPE is the zero-point energy, $\int C_p dT$ refers to enthalpic temperature correction, and TS_{vib} is the vibrational entropic contribution of the adsorbates at 300 K. The gas-phase free energies of CO_2, CO, H_2, and H_2O were corrected, due to RPBE functional error deviated from experimental thermochemical data, by adding the correction reported by Peterson and co-workers (see **Table A1)** (Peterson, Abild-Pedersen, Studt, Rossmeisl, and Nørskov, 2010). The free energy of H_2O was further corrected using the free energy of liquid-phase formation described by Calle-Vallejo and Koper (Calle-Vallejo and Koper, 2013). The computational hydrogen electrode (CHE) approach was used to account for the coupled proton-electron transfer step in free energy landscape construction (Nørskov et al., 2004). The transition state structures were located using climbing image nudged elastic band (Henkelman, Uberuaga, and Jónsson, 2000), and dimer (Henkelman and Jónsson, 1999) methods. The saddle point was confirmed with the presence of one imaginary frequency.

4.3 Results and discussion

4.3.1 Phase-separated Cu–Zn structure

The phase-separated Cu–Zn catalyst model structure is based on the experimental work by Ren and co-workers, which reported that the Cu–Zn catalysts exhibited the phase segregation of metallic Cu and Zn without alloying phase, while Cu(111) and Zn(002) planes were observed (Ren et al., 2016). Upon structural optimization, the deposited Zn cluster tends to deform from the favorable 3-dimensional geometry – seen in the isolated Zn cluster model – to 2-dimensional Zn cluster geometries (**Figure 4.1**) on the Cu(111) surface. The most stable structure exhibits all Zn atoms bound to the Cu(111) surface, as shown in **Figure 4.2(a)**. The phase-separated Cu–Zn model applied in this work is similar to the phase-separated Cu–Ag catalyst model reported by Ting and co-workers (Ting et al., 2020). Additionally, Reichenbach and co-workers performed the global minima optimizations and found

that most small Zn clusters are flat on Cu(111) surfaces and Zn atoms located at the hollow sites of Cu(111) surface (Reichenbach, Walter, Moseler, Hammer, and Bruix, 2019).

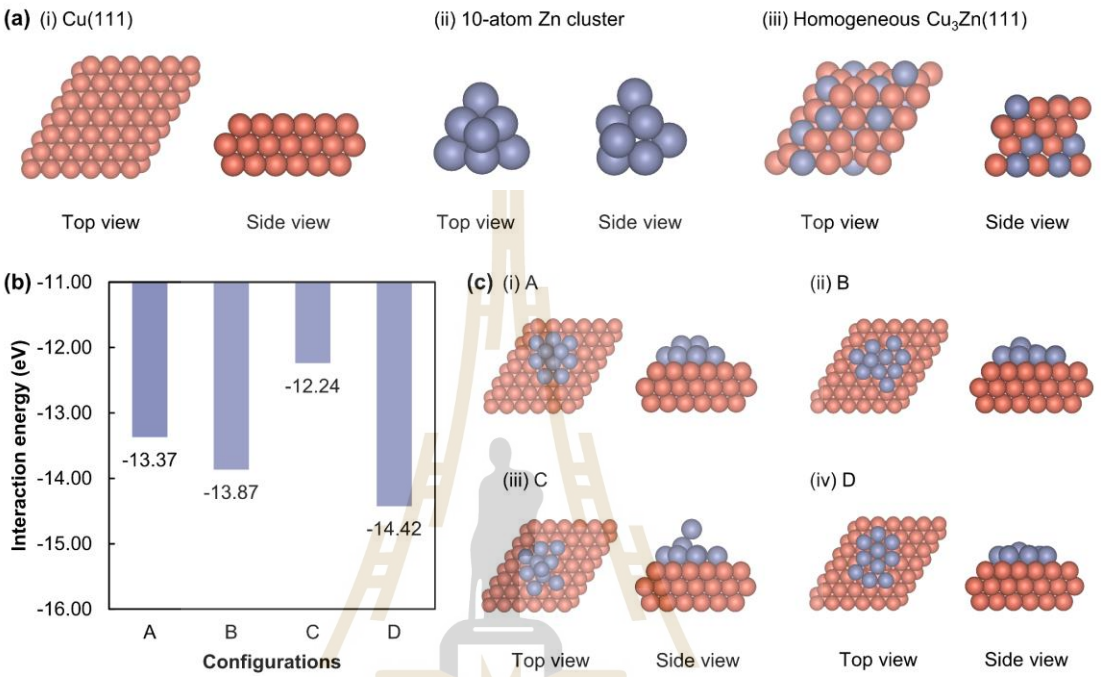

Figure 4.1 (a) Models of pure Cu (111) surface, isolated 10-atom Zn cluster, and homogeneous $Cu_3Zn(111)$ alloy surface; (b) the interaction energies between Zn cluster and Cu surface of the phase separated Cu–Zn models; (c) various configurations of the phase-separated Cu–Zn models. Cu and Zn are represented using orange and blue colors.

The interface between Cu surface and Zn cluster generates many different active sites for the reaction, classified into three groups: Cu, Zn, and interface Cu–Zn sites. The interface sites include the intermediates that bind with i) both Cu and Zn atoms, ii) Zn atoms at the cluster edge or corner, and iii) Cu atoms that close to the Zn cluster less than 3.0 Å, as shown in **Figure 4.2(a)**.

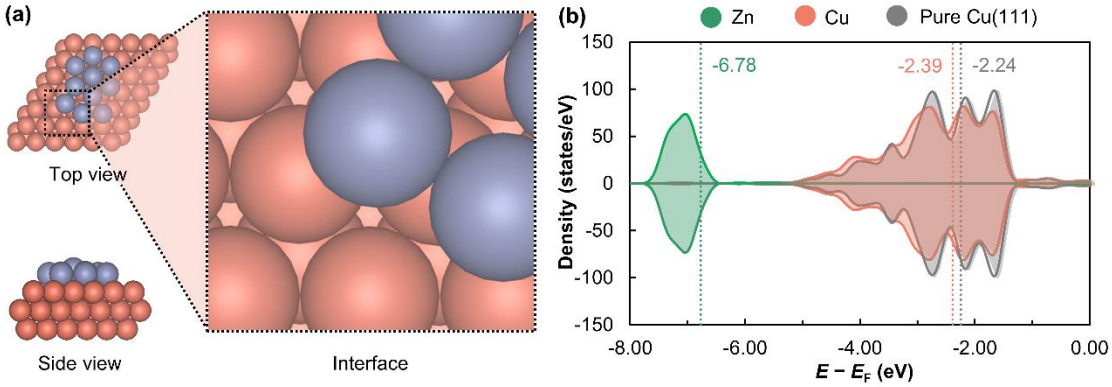

Figure 4.2 (a) The Cu–Zn model with the example of interface sites; (b) density of states for d-electrons of Cu (orange) and Zn (green) atoms on Cu–Zn structure in comparison with Cu atoms in pure Cu(111) structure (grey). The dash lines represent the corresponding calculated d-band center.

Next, we explore the electronic effect of Zn cluster on the stabilities of intermediates. As illustrated in **Figure 4.2(b)**, the localized d-electrons state of the Zn cluster locates at significantly lower energy than those of Cu surfaces, thus the Zn d-band center is located at a lower energy level relative to the Fermi energy (E_F) level. In comparison with the pure Cu(111) surface, the d-band center of the uppermost Cu layer of Cu–Zn slightly shifts to the lower energy by 0.15 eV due to the presence of the Zn cluster. This implies the effect of Zn on the electronic properties of the Cu–Zn surface leading to the change of surface reactivity. It may affect the adsorption of intermediates along the pathway.

Based on the Bader charge analysis, the Zn cluster transfers 1.38 e^- to the Cu as demonstrated in **Figure 4.3**. For the Cu atoms that bond with the Zn atom, their partial charges become more negative showing an average charge of −0.06 e^- compared to surface Cu atoms located further away from the Zn cluster showing an average charge of −0.02 e^-. Similarly, Reichenbach and co-workers also suggest that the electron of Zn atoms transfers to the surrounding surface Cu atoms (Reichenbach et al., 2019). Interestingly, the Zn effect differs from the Ag effect of Cu–Ag catalysts in that electron transfers from Cu to Ag (Lv et al., 2020). This is because Zn exhibits a lower electronegativity of 2.26 than Cu of 2.86, whereas Ag has a higher electronegativity of 2.88 (Tantardini and Oganov, 2021). The results

indicate that the Zn cluster affects the electronic properties specifically at the interface Cu–Zn sites which could change adsorption energies of the CO_2RR intermediates. Thus, the interface sites could play an important role in CO_2RR reactivity and mechanisms on phase-separated catalysts.

4.3.2 CO_2 activation

Following the tandem catalyst concept, Zn is anticipated to act as the main CO producer from the CO_2 reduction, then the CO will spillover and couple with C_1 intermediates on the Cu surface (Ren et al., 2016). After the coupling step, the intermediates are further reduced towards C_2H_4 or C_2H_5OH. Ren and co-workers reported that phase-separated Cu_x–Zn (x = 4, 2) catalysts favored the CO production at low potentials compared with other C_1 products and C_2H_5OH which are produced at more negative potentials (Ren et al., 2016). In addition, many works reported that the Cu(111) facet favored the CH_4 production (Dong, Li, and Jiang, 2018; Hussain et al., 2018; Luo, Nie, Janik, and Asthagiri, 2016; Nie, Esopi, Janik, and Asthagiri, 2013; Ou and Chen, 2020; Ou, Chen, Chen, and Jin, 2019), while Zn catalysts majorly produced the CO (Luo et al., 2020; Qin et al., 2018; Won et al., 2016; Xiao, Gao, Liu, and Luo, 2020). To thoroughly explore the active sites responsible for each process, we studied the CO_2 reduction to CO and CH_4 on Cu, Zn, and interface sites of the phase-separated Cu–Zn model. The surface atomic ratio of our Cu–Zn model is approximately 4:1 which is similar to that of the experimental result of 4:1 (Ren et al., 2016).

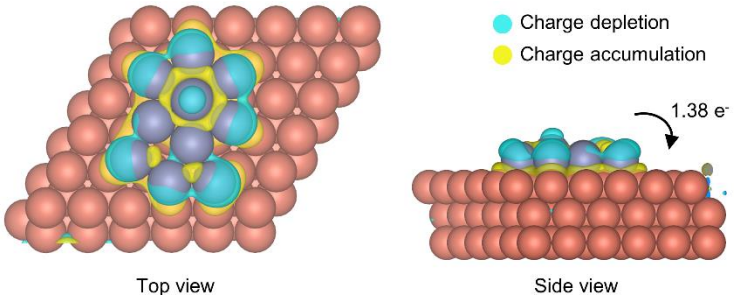

Figure 4.3 A charge density difference plot for the phase-separated Cu–Zn model. Cu atoms were represented in orange and those of Zn atoms were represented in blue. The charge density was visualized with the isosurface level of 0.39. The direction and value of charge transfer are also denoted.

The inert CO_2 molecule requires activation to undergo further reduction reaction. When the adsorbed CO_2 molecule is activated, its geometry and electronic properties are changed (Jafarzadeh, Bal, Bogaerts, and Neyts, 2020). For electrocatalysis, the activation of CO_2 is the chemisorption to form a bent configuration and negatively charged CO_2 on the surface (Etim, Zhang, and Zhong, 2021; Jafarzadeh et al., 2020). To study CO_2 reduction, we first investigate CO_2 activation on the Cu–Zn structure. The adsorbed CO_2 configurations at various sites and their adsorption energies are shown in **Figure 4.4**, and the number of accumulated charges and bond angles of adsorbed CO_2 are listed in **Table 4.1**.

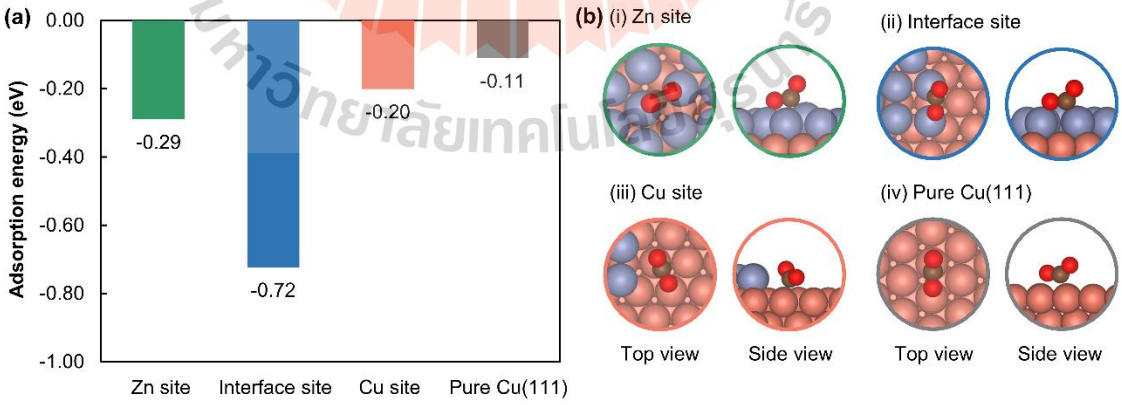

Figure 4.4 (a) The most stable CO_2 adsorption energies on Cu–Zn structure at Zn, interface, and Cu sites, and on pure Cu(111) surface, and b) the corresponding adsorbed CO_2 configurations (top and side views).

Table 4.1 Charge transferring from catalysts to adsorbed CO_2 (e^-) and O–C–O angle (°) of adsorbed CO_2 on phase-separated Cu–Zn catalyst at Zn, interface, and Cu sites, and on pure Cu(111) surface.

Active sites	Number of transferred charge (e^-)	O–C–O angle (°)
CO_2 (g)	-	179.92
Zn site	1.04	123.74
Interface site	1.07	122.44
Cu site	0.80	131.26
Pure Cu(111)	0.67	135.66

From the results, the CO_2 adsorption follows the trend from weak to strong adsorption strength: pure Cu(111), Cu, Zn, and interface sites. The strength of CO_2 adsorption monotonically increases with a more electron-rich from 0.67 - 1.07 e^- and smaller angle of molecule from 122.4 to 135.7°. The more favorable CO_2 activation at the interface site than Zn site is consistent with the work by Xiao and co-workers that activating CO_2 at Zn surfaces is more difficult than at edge and corner sites (Xiao et al., 2020). Moreover, the CO_2 adsorption is stronger on the Cu site of the Cu–Zn catalyst than on the pure Cu(111) surface which could be ascribed to the Zn effect on the electronic properties of the Cu surface as discussed in the previous section and **Figure 4.3(b)**, which the d-band center of surface Cu atoms shifts to lower energy compared to that of the pure Cu surface. Thus, the interface Cu–Zn site facilitates the CO_2 activation at a higher degree compared to the other sites on the Cu–Zn catalyst and the pure Cu catalyst.

4.3.3 CO_2 reduction to CO

After the CO_2 activation, the CO_2 can be reduced to CO on Zn, Cu, and interface sites. From the experimental study of the Cu–Zn catalysts, the CO product was predominantly produced first at −0.65 V vs RHE (Ren et al., 2016). Thus, CO production is important at relatively low potential. In this section, the CO_2 reduction to CO at all the Cu–Zn sites is discussed.

As shown in **Figure 4.5(a)**, the *CO production on phase-separated Cu–Zn structure is energetically downhill at the Cu site while it is uphill by 0.13 and 0.24 eV at the Zn and interface sites, respectively. **Figure 4.5(c)** illustrates that the adsorbed configurations of *CO and *COOH are different at the sites depending on Cu and Zn atoms. Overall, the Zn site is suitable for gaseous CO production showing a slight reaction energy of 0.13 eV and being favorable for the CO desorption step. The CO desorption is unfavorable with the endergonic reaction energy at Cu (0.51 eV) and interface sites (0.20 eV) on the phase-separated Cu–Zn structure as well as on the Cu_3Zn homogeneous surface (0.61 eV). Thus, these sites would facilitate further CO reduction steps on the surface. The interface site could play a significant role in *CO formation because it substantially promotes the first electron-proton transfer step of *COOH formation compared to the other sites. Furthermore, the weak adsorption of *CO at the interfacial sites may better facilitate the next *CO reduction step.

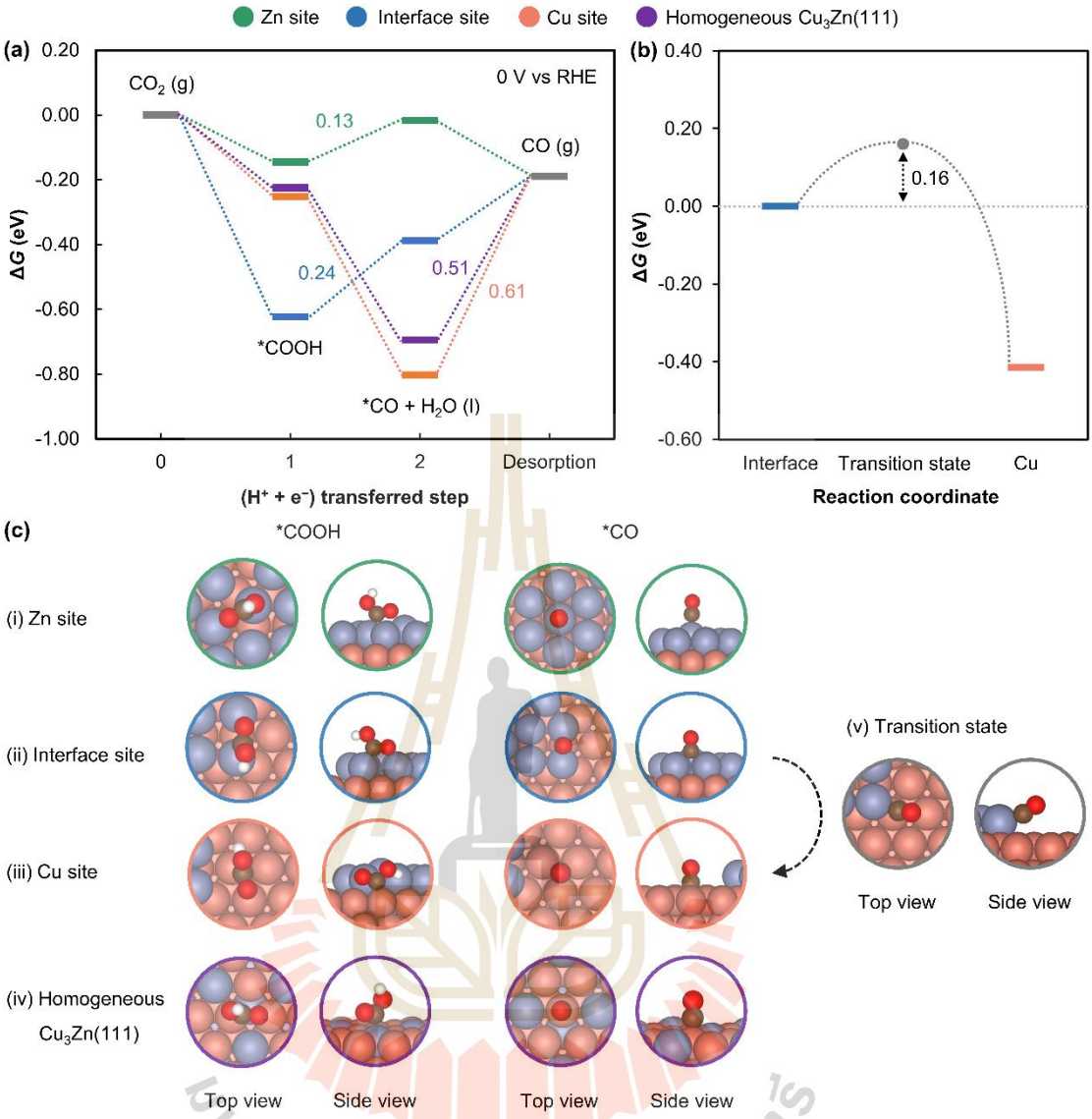

Figure 4.5 (a) Relative free energy profiles of CO_2 reduction to CO at 0 V vs RHE at various sites: Zn (green), interface (blue), Cu (orange) sites on Cu–Zn structure and on homogeneous $Cu_3Zn(111)$ structure (purple). The free energy reference is the state of * + 2×(CO_2 (g)) + 12×(½H_2 (g)).; (b) relative energy profile of the CO spillover from interface to Cu sites on Cu–Zn structure; (c) the corresponding adsorbed configurations of *COOH and *CO intermediates on Cu–Zn structure, and the transition state structure of the *CO spillover (top and side views).

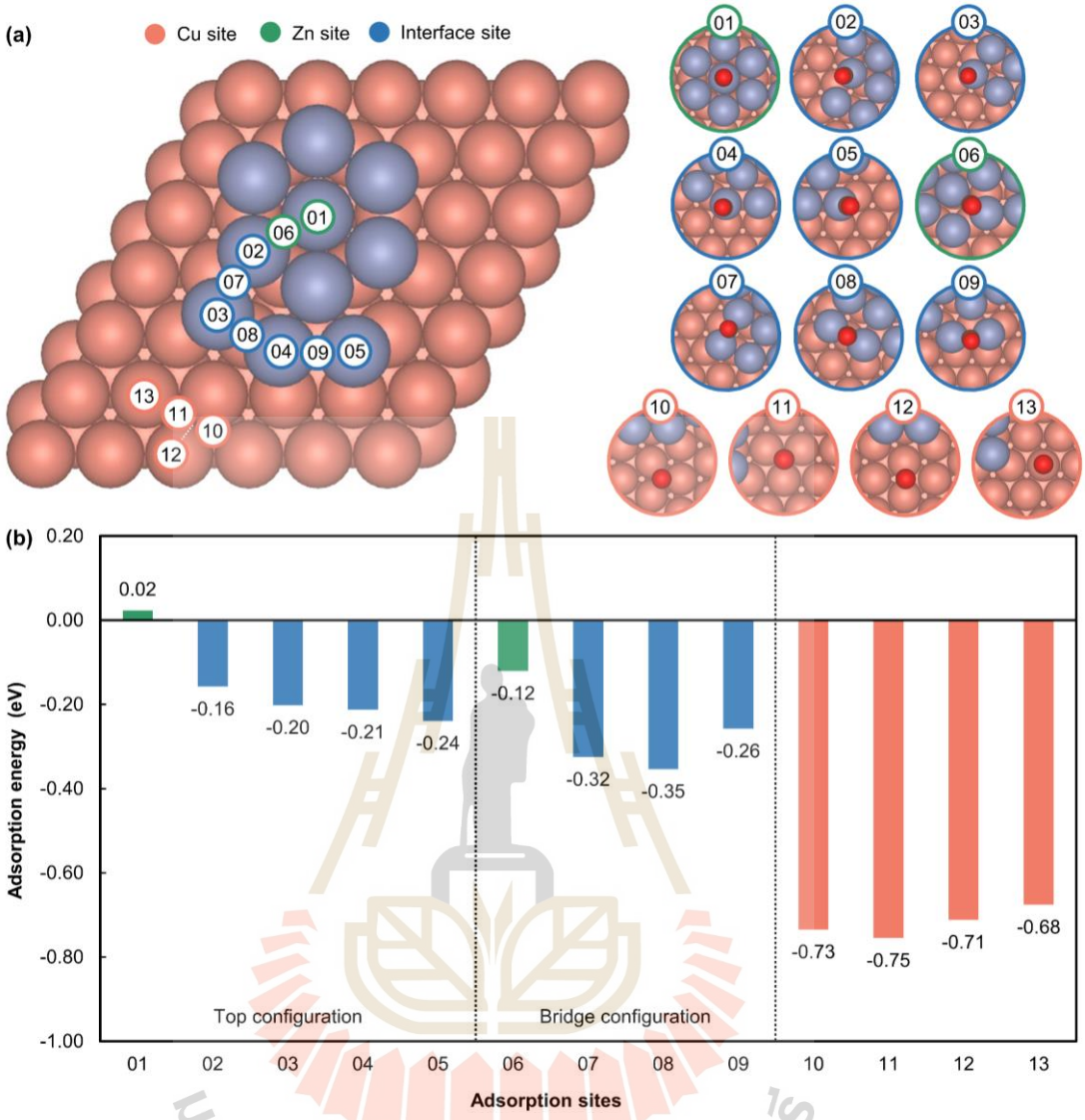

Figure 4.6 (a) *CO adsorption on the Cu–Zn model at Cu (orange), Zn (green), and interface (blue) sites; (b) the corresponding adsorption energies. Top and bridge *CO adsorptions were found at Zn and interface sites. Four distinct *CO adsorption configurations were found at hexagonal close-packed (hcp) hollow (10), face-centered cubic (fcc) hollow (11), bridge (12), and top (13) at Cu sites.

Since *CO is the important intermediate in CO_2RR to produce C_2 products (J. Li et al., 2019; Morales-Guio et al., 2018; Wang et al., 2019), the *CO adsorption was explored at many possible sites on the phase-separated Cu–Zn structure. The results shown in **Figure 4.6** demonstrate weaker *CO adsorption at all interface sites showing an adsorption energy in a range between −0.16 and −0.35 eV while the adsorption energies at the Cu sites were double in a range between −0.68 and −0.73 eV. The favorability of *CO desorption at the Zn site could lead to more CO (g) production when Zn composition increases. Ren and co-workers suggest that the phase-separated Cu–Zn catalyst with the ratio of 2:1 yields higher amount of CO (g) than that with the ratio of 4:1 (Ren et al., 2016). These results signify the role of high-coordinated Zn as the CO (g) promoter, while it suggests that the interface Cu–Zn site stabilizes the *CO intermediate. Those *CO adsorbed at the Zn sites are likely to desorb as CO (g) or diffuse to the interface sites and Cu sites since the *CO binds stronger at those sites. Thus, the later *CO reduction steps are anticipated to take place at the interface site and Cu sites.

Due to highly favorable *CO adsorption at the Cu site, we include the possibility that the produced *CO at the interface site may spillover to the Cu sites. As shown in **Figure 4.5(b)**, the spillover is thermodynamically and kinetically favored with a reaction energy of −0.41 eV and a small energy barrier of 0.16 eV. The *CO could spillover through a low-coordinated Zn atom at the corner as shown in **Figure 4.5(c, iv)**. The *CO spillover was also reported to be feasible on Cu–Ag catalyst with the reaction energy and energy barrier of −0.39 and 0.17 eV, respectively (Ting et al., 2020). This suggests that the CO spillover can occur on the Cu–Zn catalyst.

4.3.4 CO reduction to CH_4

Based on the experimental results, the major C_1 product of Cu–Zn catalysts is CO with a minor amount of CH_4 compared with the other products (Ren et al., 2016). Ren and co-workers showed that the Cu–Zn catalyst with a ratio of 4:1 produced the highest FE for CO of 40.22% at −0.95 V vs. RHE (Ren et al., 2016). Then, the C_2H_5OH production reaches the maximum FE of 29.14% at −1.05 V vs. RHE, whereas that of CO drops to 10.36% (Ren et al., 2016). At more negative potentials, the FE of C_2H_5OH decreases with the increase of FE for CH_4 (Ren et al., 2016). This implies that CH_4 and C_2H_5OH productions may share the same intermediates. Moreover, Cu(111) favors the CH_4 production for CO_2RR (Dong et al., 2018; Hussain et al., 2018; Luo et al., 2016; Nie et al., 2013; Ou and Chen, 2020; Ou et al., 2019). Therefore, the C_1 intermediates toward CH_4 should be considered as possible candidates for C–C coupling steps.

Several pathways for CO_2RR to CH_4 on Cu(111) surface were proposed using different solvent models (Dong et al., 2018; Hussain, Jónsson, and Skúlason, 2016; Hussain et al., 2018; Hussain, Skúlason, and Jónsson, 2015; Nie et al., 2013). Peterson and co-workers studied the CH_4 formation on pure Cu(111) surface, accounting for the solvent effect by using hexagonal water overlayer (Peterson et al., 2010). They proposed that the CH_4 formation is formed through a *CHO intermediate and a series of subsequent reduction steps to $*CH_2O$ and $*CH_3O$ (Peterson et al., 2010). The CH_4 product is formed by the final $*CH_3O$ reduction step. Meanwhile, Nie and co-workers theoretically studied the CH_4 formation on pure Cu(111) surface by including an explicit water molecule (12 explicit H_2O molecules): the CH_4 production proceeds through a reduction of *CO to *COH, leading to $*CH_x$ intermediate species and finally, CH_4 (Nie et al., 2013). In this work, we adopted the *CHOH pathway (the intermediate after subsequent hydrogenation to *CHO) proposed by Oh and co-workers where their simulations were modeled using fully two relaxed explicit water layers on pure Cu(111) surface (Ou and Chen, 2020; Ou et al., 2019). Here, we explored the CO reduction reaction to CH_4 at both the interface and Cu sites on phase-separated Cu–Zn structure, and the free energy diagrams are shown in **Figure 4.7(a)**.

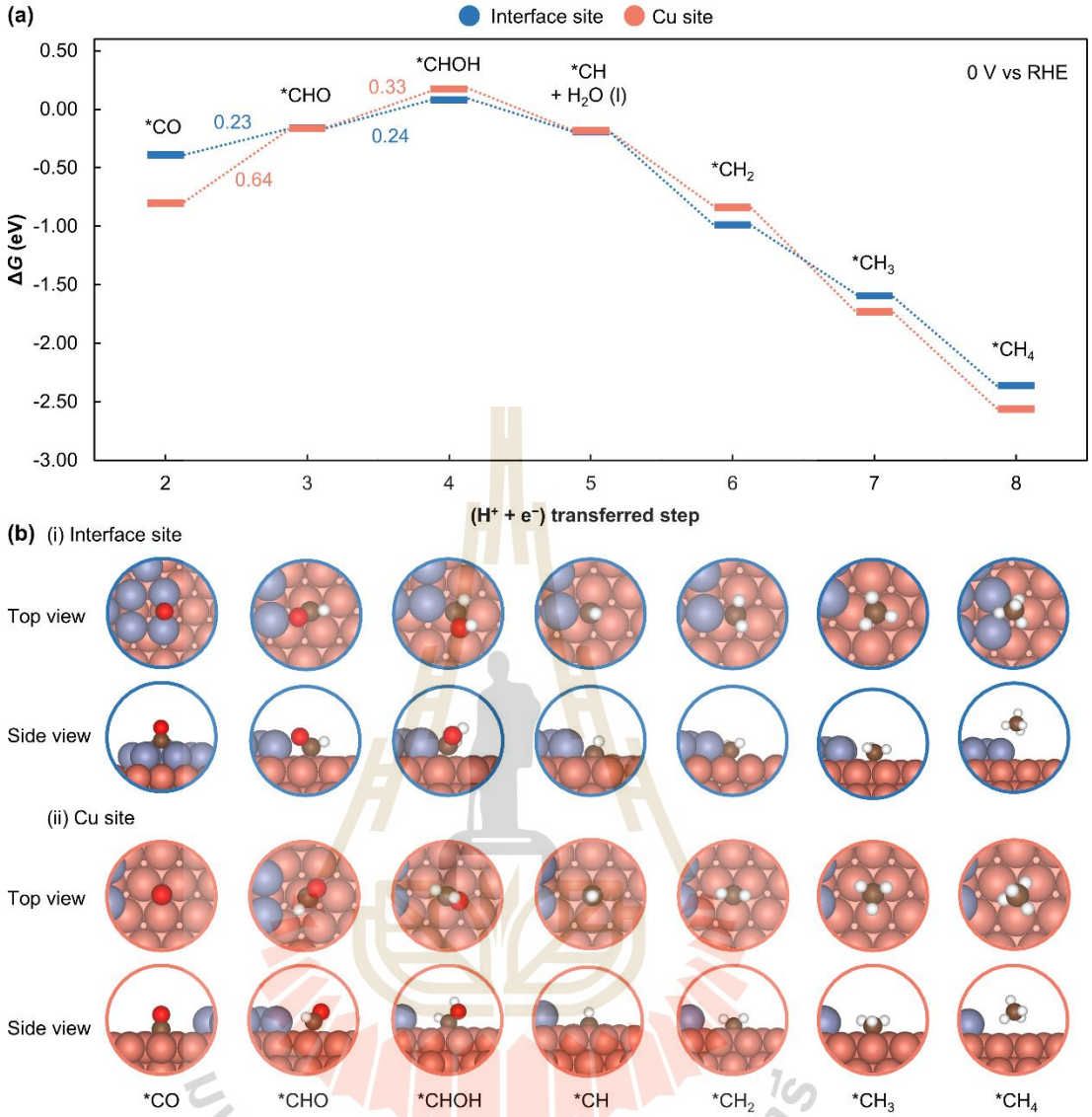

Figure 4.7 (a) Relative free energies profiles for the *CO reduction to CH_4 at 0 V vs RHE at the interface (blue) and Cu (orange) sites on phase-separated Cu–Zn structure.; b) top and side views of the corresponding adsorbed intermediates configurations at the interface and Cu sites. The free energy reference is the state of * + 2×(CO_2 (g)) + 12×(½H_2 (g)).

Figure 4.7(a) shows that some intermediates are more stabilized at the interface sites than those at Cu sites, including *CHO, *CHOH, *CH_2, and *CH_3 in the pathway except for *CO, *CH, and *CH_4. At the Cu sites, the most challenging step is *CO reduction to *CHO, which requires the reaction free energy of 0.64 eV. This step was also reported to be the potential limiting step on pure Cu(111) catalyst (Dong et al., 2018; Ou and Chen, 2020; Ou et al., 2019; Peterson et al., 2010). At the interface site, the reaction free energy of *CO reduction to *CHO is significantly lower to 0.23 eV, while the *CHO reduction to *CHOH step shows a reaction free energy of 0.24 eV. After forming *CHOH, the subsequent reduction steps to *CH_4 are all favorable at both interface and Cu sites. This shows that the interface site may facilitate CH_4 production by stabilizing certain intermediates.

The potential limiting step of *CO reduction to *CHO is facilitated at the interface sites because *CO adsorption is suitably weakened. Furthermore, the later reduction steps become more favored at the interface sites because the intermediates i.e., *CHOH, *CH, and *CH_2 along the pathway are more stabilized compared with those on Cu sites. **Figure 4.7(b)** illustrates that, at the interface site, *CO formation is favored on the Zn edge atom whereas the formation of other C_1 intermediates takes place on those Cu atoms at the interface site. For the Cu site, most intermediates adsorb at the hollow-fcc sites except for *CHO that adsorbs at the top site. These findings suggest that the interface sites on the Cu–Zn catalysts favor *CO reduction and formation of the C_1 intermediates. This could influence the C_2 production since these C_1 intermediates are key intermediates for the C–C coupling steps, as will be discussed in **Section 4.3.6**.

4.3.5 Hydrogen evolution reaction

The hydrogen evolution reaction (HER) is one of the competitive reactions that hinders the C_2 production of CO_2RR (Nitopi et al., 2019). Hori and co-workers showed that the H_2 evolution increases while the hydrocarbon formation decreases with small amounts of Zn contaminant on the Cu catalyst (Hori et al., 2005). To investigate the HER activity of the Cu–Zn catalysts, **Figure 4.8** shows the energy profile of HER at different sites i.e. Cu, Zn, and two interface sites denoted as the interface A and B sites. The interface A site is the bridge site between Zn edge atoms and the interface B site is the hollow site of Cu atoms in contact with the Zn cluster.

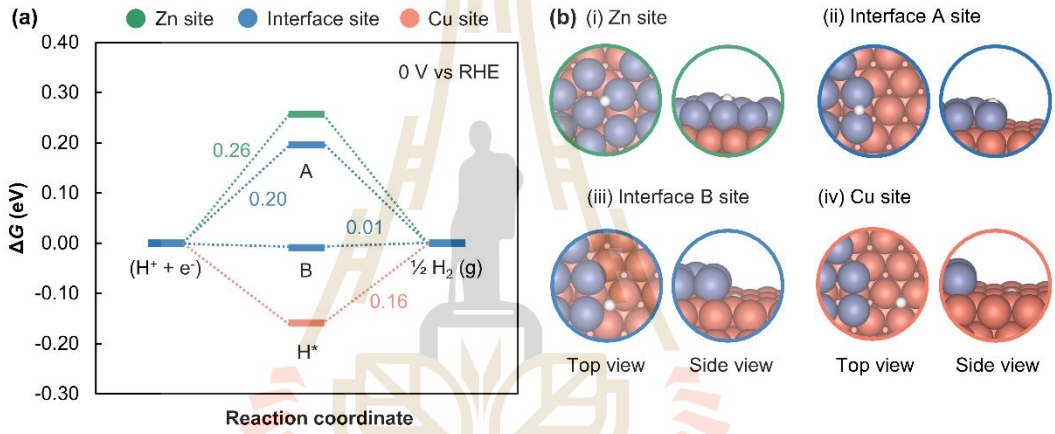

Figure 4.8 (a) Relative free energy profiles of hydrogen evolution reaction (HER) at 0 V vs RHE on various sites: Zn, Cu, interface A and interface B sites on the Cu–Zn structure; (b) the corresponding adsorbed configuration of *H on those sites (top and side view).

Figure 4.8(a) reveals that HER is most favorable at the interface B site, while it is least favorable on the Zn cluster. The reaction free energies of the most difficult step are relatively low at all sites, ranging from 0.01 – 0.26 eV. Additionally, the *H adsorption energy on the Cu site (–0.16 eV) is slightly lower than those that reported for (111) and (100) surfaces of Cu with adsorption energies of –0.24 and –0.29 eV, respectively, calculated using the explicit solvent model (Wang et al., 2020). As seen in **Figure 4.8(b)**, *H intermediate favors adsorbing at the hollow-fcc site on Cu which is consistent with the work of Xu and co-workers that the hollow-fcc site is the most preferred site (Xu, Lin, Bai, and Mavrikakis, 2018). On the Zn cluster, *H is favorable to adsorb at the bridge site, yet it was reported that *H can favor the top site of low-

coordinated Zn atoms at the edge or corner of the cluster (Xiao et al., 2020; Zhang et al., 2018). The results indicate that the Cu–Zn structure could promote H_2 evolution at the interface site on Cu, while the HER at the Cu site remains as favorable as on a pure Cu catalyst.

The *CO favorability of the phase-separated Cu–Zn surface may affect the HER activity. Cave and co-workers found that the high *CO coverage on the strong *CO-binding metal surfaces can weaken the *H binding energy and shift it further away from the optimal ΔG value of zero, thus lowering the HER activity (Cave et al., 2018). *CO is highly favorable at the Cu site, which may lead to high *CO coverage on the surface. The presence of the high *CO coverage may be able to potentially decrease the *H binding energy at the interface B site, leading to the HER suppression at the active interface sites. This is of significance as these sites play a vital role in the C–C coupling steps, as will be discussed in the next section.

4.3.6 Identification of the C–C coupling steps for C_2 production

The C–C coupling step is crucial for the C_2 production of CO_2RR on Cu-based catalysts (Garza et al., 2018; Nitopi et al., 2019; Santatiwongchai et al., 2021). The formation of C_2 products including C_2H_4 and C_2H_5OH requires the C–C coupling step of two C_1 intermediates. Many works of CO_2RR on Cu(100) surface considered the C–C coupling step to involve *CO, *CHO, and *COH intermediates (Calle-Vallejo and Koper, 2013; Garza et al., 2018; Luo et al., 2016; Sandberg, Montoya, Chan, and Nørskov, 2016). We consider the possibility of coupling between *CO and other intermediates in the CH_4 pathway on the Cu–Zn surface for two reasons. First, the CH_4 formation increases while the formation of C_2H_5OH decreases at the same potential on Cu–Zn catalysts (Ren et al., 2016). Second, the Cu(111) surface showed the highest reactivity towards CH_4, thus coupling between *CO and other C_1 intermediates in the CH_4 pathway possibly occur on Cu–Zn surface.

On bimetallic Cu-based catalysts, researchers proposed several C–C coupling steps as the key reaction leading to C_2 products such as *CO–*CO, *CO–*CHO, and *CO–*CH_2 coupling steps (Li et al., 2021; Lv et al., 2020; Ting et al., 2020). In this work, we thoroughly explore the coupling between *CO and all intermediates in the CH_4 pathway on the phase-separated Cu–Zn structure. The reaction free energies (ΔG_{rxn}) and free energy barriers ($\Delta G^{\neq}$) of all considered C–C coupling steps are shown in **Figure 4.9(a)**.The energy profiles of all coupling reactions are exhibited in **Figure 4.10 - 4.12**, and their corresponding values are summarized in **Table 4.2**.

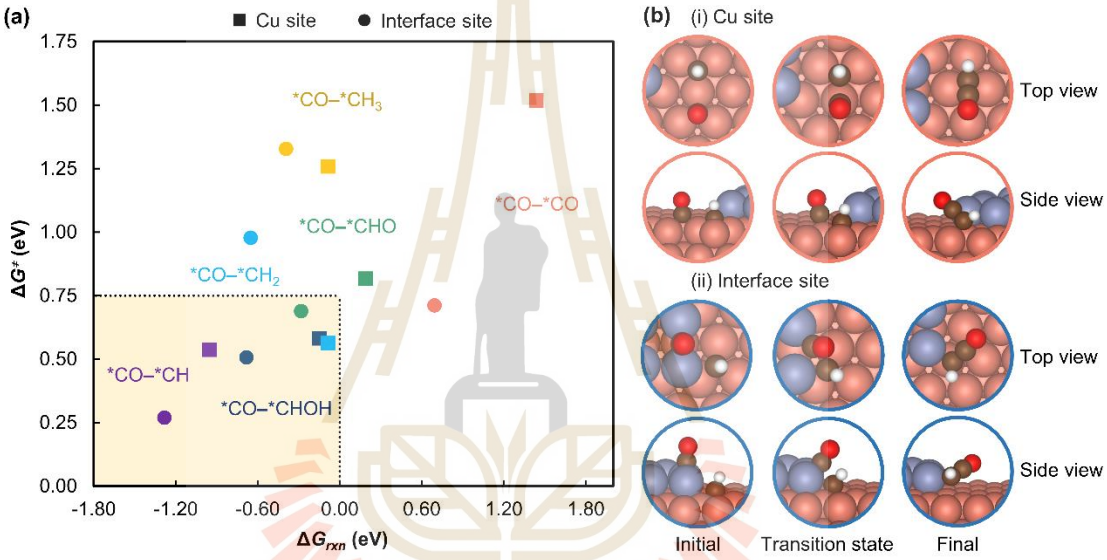

Figure 4.9 (a) A plot between the reaction free energies (ΔG_{rxn}) and free energy barriers ($\Delta G^{\neq}$) of the C–C coupling reactions at the interface (circle) and Cu (square) sites on phase-separated Cu–Zn structure (Each color indicates a different C–C coupling reaction) and (b) the corresponding structures of the initial, transition and final states of the *CO–*CH coupling reaction at the interface and Cu sites.

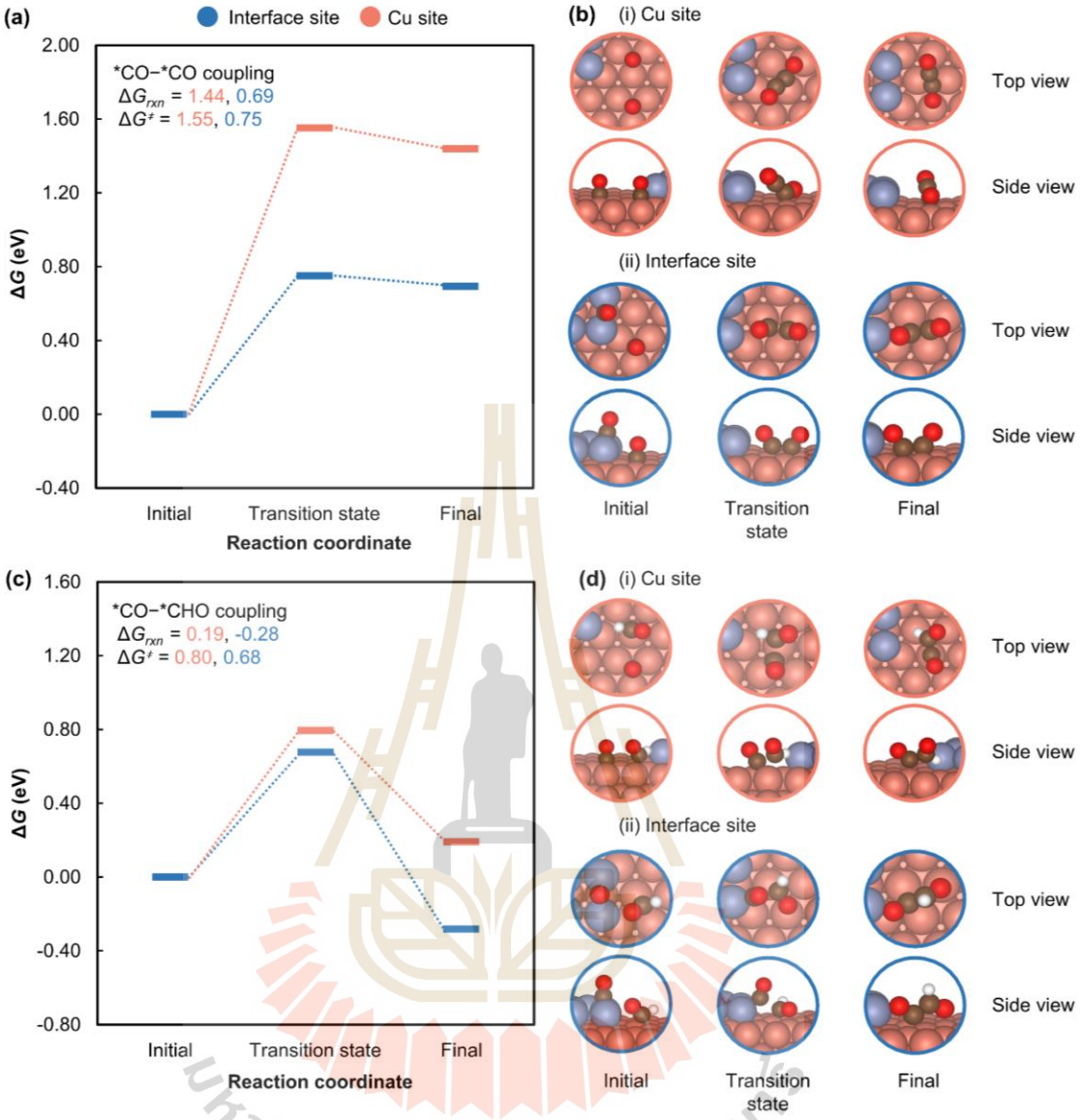

Figure 4.10 Relative free energy profiles for the (a) *CO–*CO and (c) *CO–*CHO coupling reactions at the interface and Cu sites of the phase-separated Cu–Zn structure and their corresponding structures of the initial, transition and final states of the (b) *CO–*CO and (d) *CO–*CHO coupling reactions.

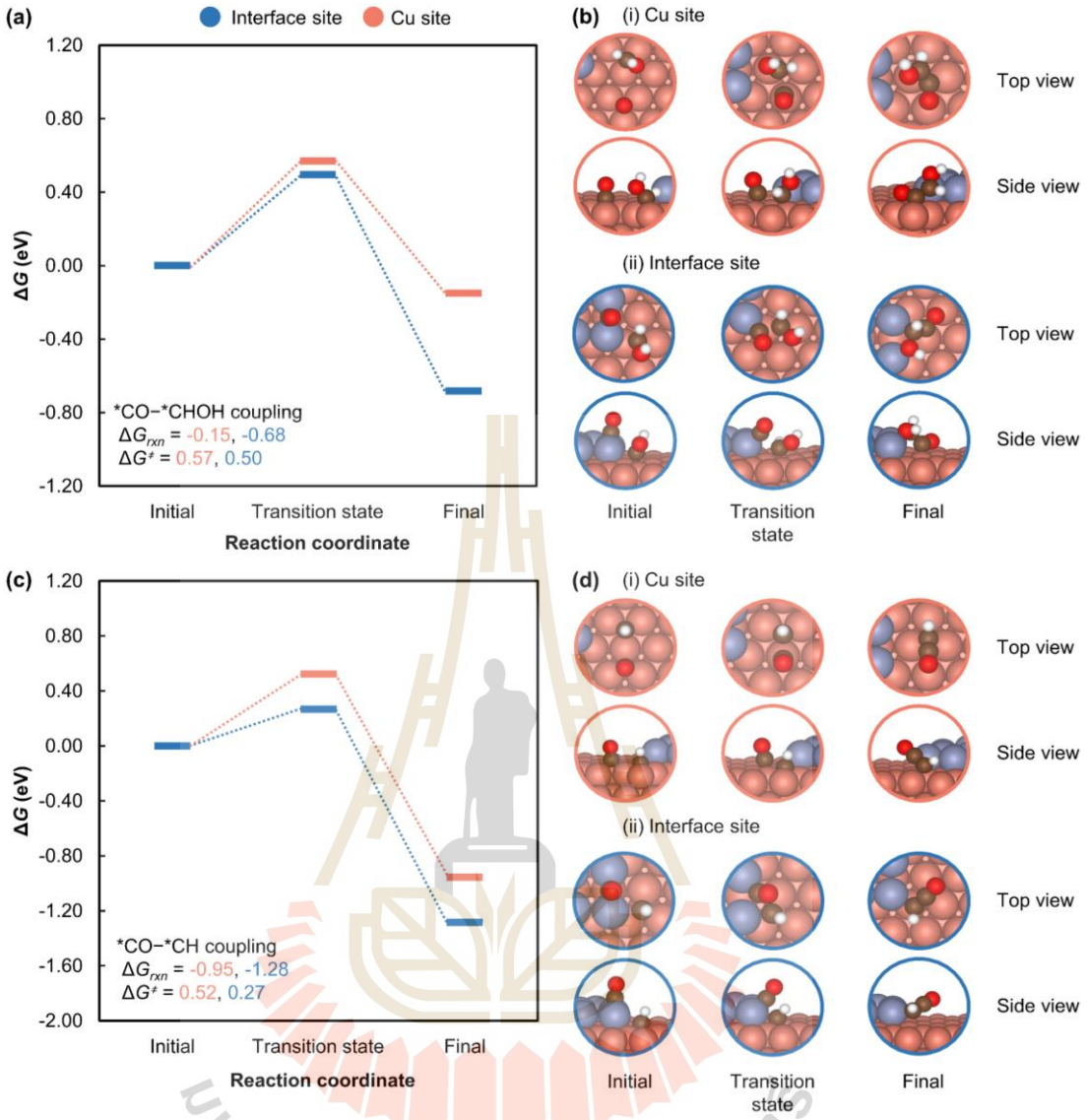

Figure 4.11 Relative free energy profiles for the (a) *CO−*CHOH and (c) *CO−*CH coupling reactions at the interface and Cu sites of the phase-separated Cu–Zn structure and their corresponding structures of the initial, transition and final states of the (b) *CO−*CHOH and (d) *CO−*CH coupling reactions.

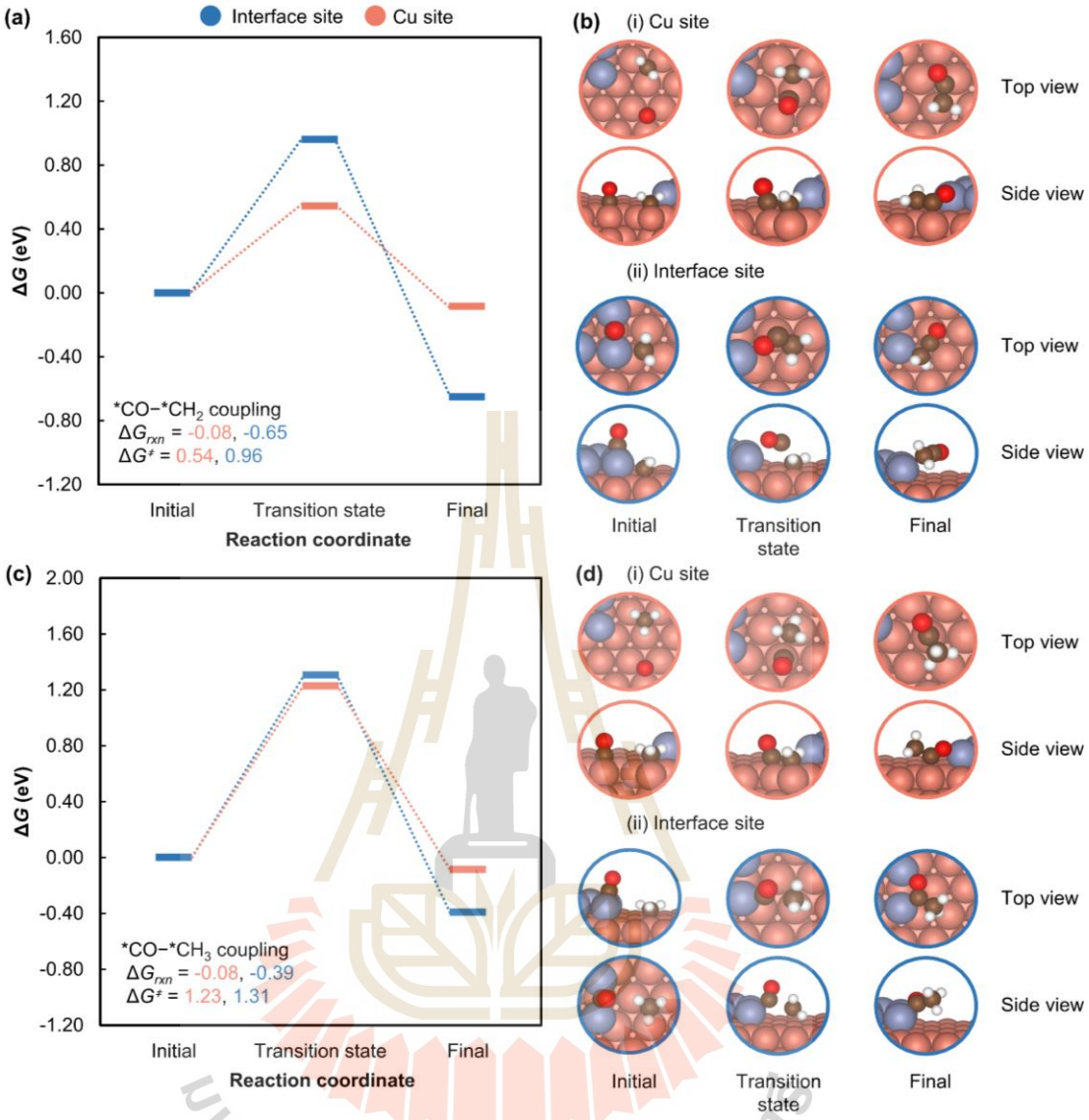

Figure 4.12 Relative free energy profiles for the (a) *CO–*CH_2 and (c) *CO–*CH_3 coupling reactions at the interface and Cu sites of the phase-separated Cu–Zn structure and their corresponding structures of the initial, transition and final states of the (b) *CO–*CH_2 and (d) *CO–*CH_3 coupling reactions.

Table 4.2 Reaction free energies (ΔG_{rxn}) and free energy barriers ($\Delta G^{\neq}$) of the C–C coupling reactions at the Cu and interface sites on phase-separated Cu–Zn structure.

C-C coupling reaction	Cu site		Interface site	
	ΔG_{rxn} (eV)	$\Delta G^{\neq}$ (eV)	ΔG_{rxn} (eV)	$\Delta G^{\neq}$ (eV)
*CO–*CO	1.44	1.55	0.69	0.75
*CO–*CHO	0.19	0.80	-0.28	0.68
*CO–*CHOH	-0.15	0.57	-0.68	0.50
*CO–*CH	-0.95	0.52	-1.28	0.27
CO–CH_2	-0.08	0.54	-0.65	0.96
CO–CH_3	-0.08	1.23	-0.39	1.31

The C–C coupling and the subsequent reduction steps leading to C_2H_5OH were proposed to take place predominantly at the Cu sites on bimetallic Cu-based catalysts (Morales-Guio et al., 2018; Ren et al., 2016; Ting et al., 2020). However, our work demonstrates that the interface site is the most preferable site, promoting CO_2 activation and *CO reduction. Therefore, in this work, the C–C coupling reactions are investigated at both the interface and Cu sites on the phase-separated Cu–Zn structure.

The feasibility of C–C coupling is assessed based on two criteria: the ΔG_{rxn} should be exergonic, and the $\Delta G^{\neq}$ should be lower than 0.75 eV which is the upper limit for achieving facile kinetics with a turnover frequency of approximately 1 s^{-1} at room temperature (Nitopi et al., 2019; Sandberg et al., 2016). Based on these two criteria, the results in **Figure 4.9(a)** demonstrate that several C–C coupling steps are feasible on the Cu–Zn catalyst. These include the *CO–*CHOH and *CO–*CH coupling reactions at both the interface and Cu sites, as well as *CO–*CHO at the interface site and *CO–*CH_2 at the Cu site. The *CO–*CH coupling at the interface site is the most

preferable coupling step on the phase-separated Cu–Zn catalyst, showing the lowest ΔG_{rxn} of -1.28 eV and $\Delta G^{\neq}$ of 0.27 eV. In comparison, ΔG_{rxn} and $\Delta G^{\neq}$ of the *CO–*CH coupling step are −0.90 and 0.98 eV, respectively, on the homogeneous $Cu_3Zn(111)$ surface as shown in **Figure 4.13** These clearly indicate that the C–C coupling on homogeneous Cu–Zn catalyst is significantly less energetically and kinetically favorable than at the interface sites. This signifies the important role of the interface sites in promoting the C–C coupling step. Additionally, the significant decrease in the ΔG_{rxn}, and $\Delta G^{\neq}$ of most coupling reactions between the interface and Cu sites, as depicted in **Figure 4.9(a)**, highlights the vital role of the interface sites.

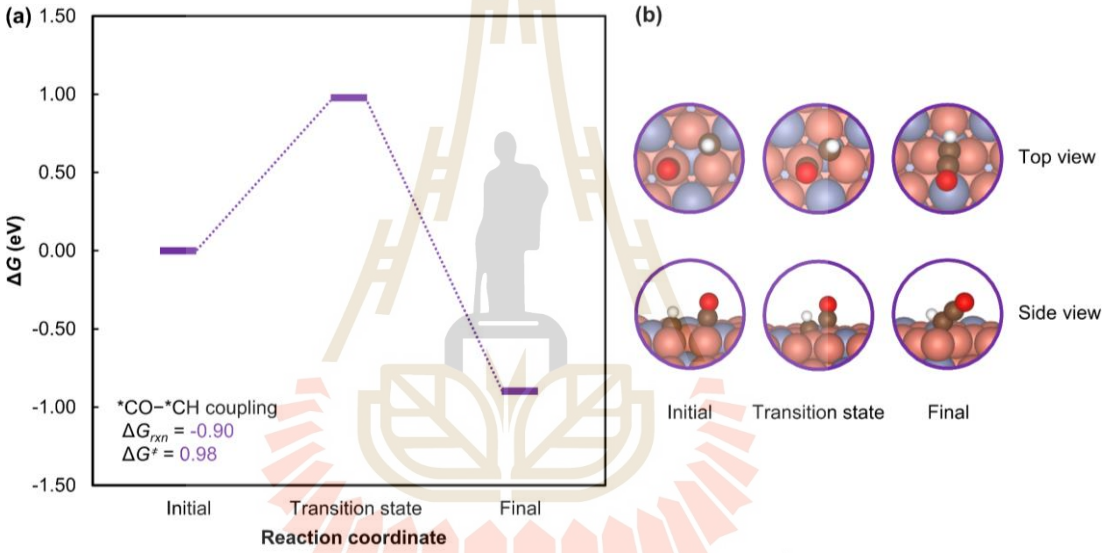

Figure 4.13 Relative free energy profile for *CO–*CH coupling reaction on the homogeneous $Cu_3Zn(111)$ surface (a) and the corresponding structures of initial, transition and final states (b).

The intermediate configurations also exhibit substantial distinctions. As shown in **Figure 4.9(b)**, for the Cu site, *CO and *CH adsorb at the hollow-fcc and hollow-hcp sites, respectively. After coupling, the *CHCO adsorbs on the 3-fold site through the carbon atom of an alkyl (–CH) end. For the interface site, the *CO adsorbs on the bridge of the Zn cluster, while *CH absorbs on the hollow-hcp site of Cu near the Zn atom. The coupling product binds at the top of the corner Zn atom with the same binding mode at the Cu site. This shows that the interface site provides favorable binding configurations promoting the C_2 production.

The C–C coupling reactions on bare Cu(111) surface are more difficult than those that occur at the interface. Ting and co-workers suggested that *CO–*CH and *CO–*CH_2 have the $\Delta G^{\neq}$ of 0.70 and 0.71 eV, respectively, through the Langmuir–Hinshelwood (LH) mechanism on pure Cu(111) surface (Ting et al., 2020). To assess this possibility, we studied the *CO–*CH and *CO–*CH_2 coupling reactions on the pure Cu(111) surface using both Langmuir-Hinshelwood (LH) and Eley-Rideal (ER) mechanisms. The results are exhibited in **Figure 4.14 – 4.15**. The *CO–*CH coupling reaction exhibits a $\Delta G^{\neq}$ of 0.46 eV for the LH mechanism and 1.17 eV for the ER mechanism. For the *CO–*CH_2 coupling reaction, the $\Delta G^{\neq}$ values are 0.56 eV for the LH mechanism and 1.11 eV for the ER mechanism. These results are consistent with the findings reported by Ting and co-workers, suggesting that the *CO–*CH and *CO–*CH_2 coupling reactions prefer the LH mechanism. In comparison, the *CO–*CH coupling step exhibits a lower $\Delta G^{\neq}$ at the interface site compared to that on the pure Cu(111), following the LH mechanism (Ting et al., 2020). This result also suggests the influence of the interface site in promoting the *CO–*CH coupling step for CO_2RR on the Cu–Zn catalyst.

Many works proposed that the C_2 production from CO_2RR on Cu-based catalysts occurs through the *CO–*CO, *CO–*CHO coupling steps (Garza et al., 2018; Li et al., 2021; Lv et al., 2020; Sandberg et al., 2016; Santatiwongchai et al., 2021). As shown in **Figure 4.9(a)**, the *CO–*CO coupling reactions at both interface and Cu sites are unfavored on the phase-separated Cu–Zn structure. The *CO–*CHO coupling step at the interface site could be feasible with the ΔG_{rxn} value of −0.28 eV and $\Delta G^{\neq}$ value of 0.68 eV. On the other hand, the *CO–*CHO coupling at the Cu site is energetically and kinetically unfavorable, with a ΔG_{rxn} of 0.19 eV and $\Delta G^{\neq}$ of 0.80 eV. Thus, the *CO–*CO and *CO–*CHO coupling may not take place on the phase-separated Cu–Zn catalyst. In comparison to the previously reported results on the Cu(100) surface (Lin et al., 2023), the reactivity is unimproved for the *CO–*CO and *CO–*CHO coupling reactions on the phase-separated Cu–Zn, except for the *CO–*CHO coupling at the interface site. In contrast, the other C–C coupling reactions that are unlikely to occur on the Cu(100) surface are found to be substantially more favorable at both the interface and Cu sites on the phase-separated Cu–Zn catalyst. This implies a significant change in

the CO_2RR mechanisms toward multi-carbon products on phase-separated Cu-based catalysts. Furthermore, it is worth noting that a change in the C–C coupling step may not apply to the homogeneous Cu–Zn catalyst, as the *CO–*CO coupling was found to be energetically and kinetically feasible (Juntrapirom et al., 2021). Nevertheless, a thorough investigation should be done in the future.

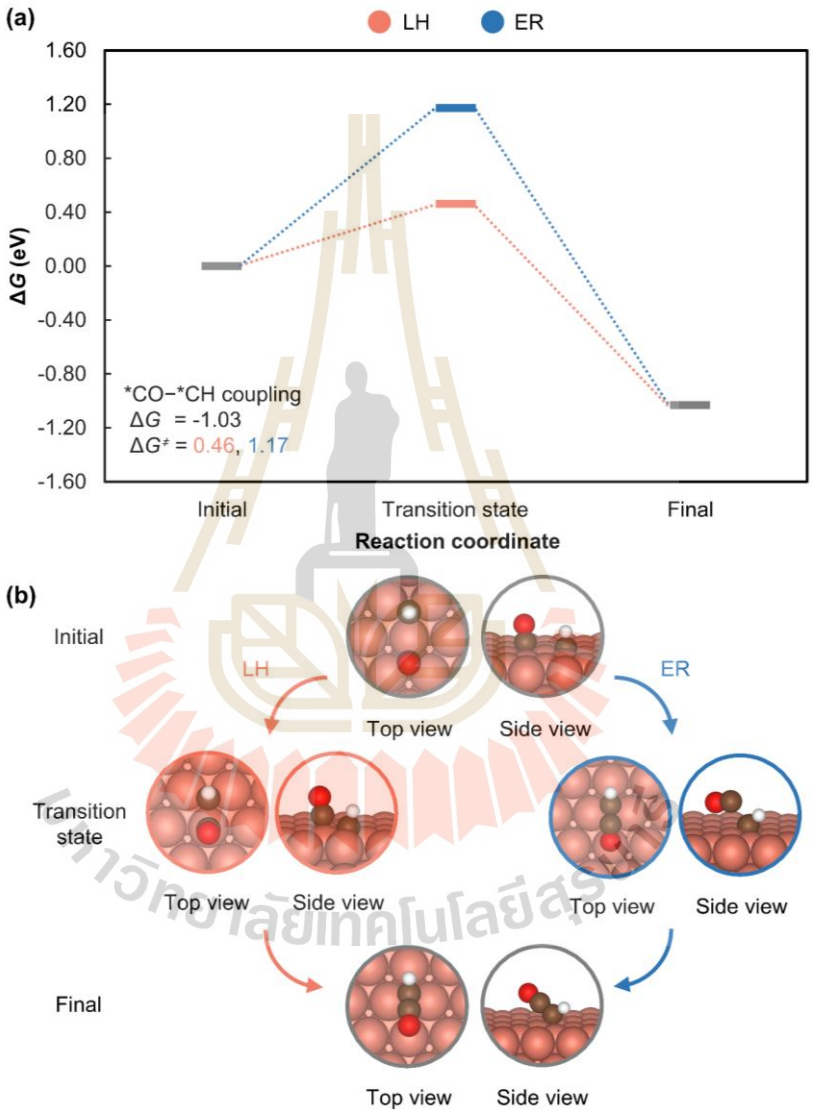

Figure 4.14 (a) Relative free energy profile for *CO–*CH coupling reaction on the pure Cu(111) surface following the Eley-Rideal (ER) and Langmuir-Hinshelwood (LH) mechanisms and (b) the corresponding structures of the initial, transition and final state.

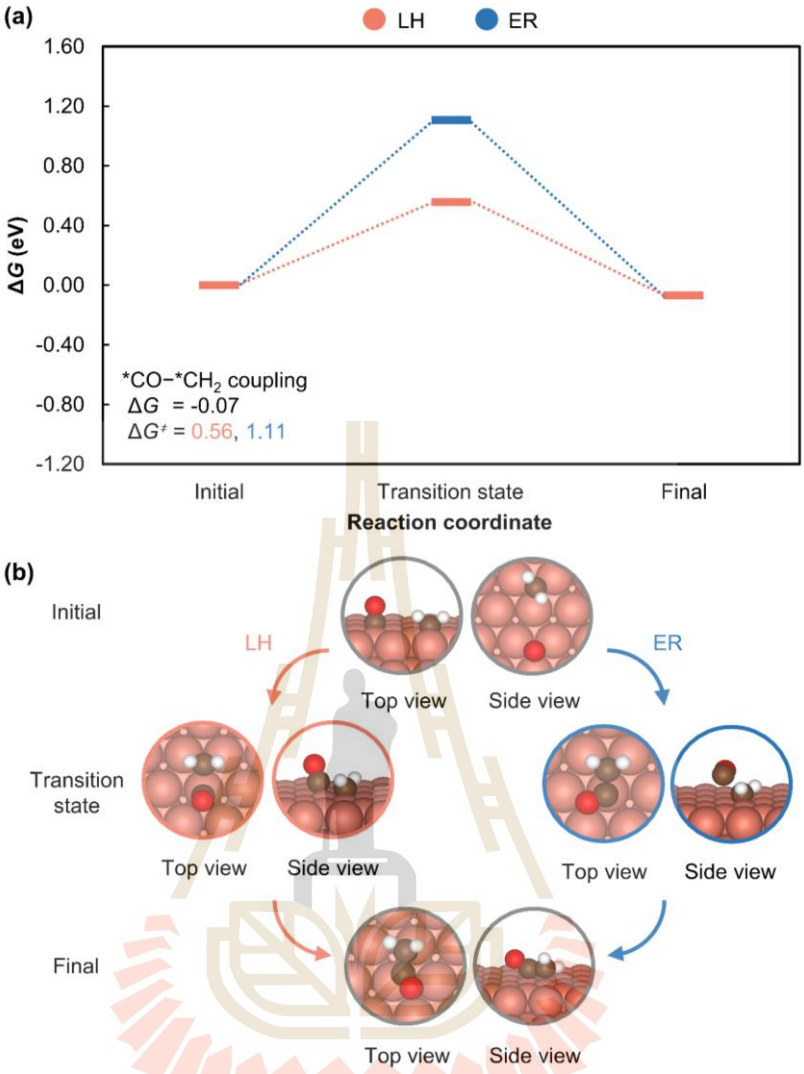

Figure 4.15 (a) Relative free energy profile for *CO–*CH_2 coupling reaction on the pure Cu(111) surface following the Eley-Rideal (ER) and Langmuir-Hinshelwood (LH) mechanisms and (b) the corresponding structures of the initial, transition and final state.

4.3.7 Late reduction steps toward C_2H_4 and C_2H_5OH

While C_2H_5OH is a valuable liquid fuel, it is commonly observed that most Cu-based catalysts yield higher reactivity and selectivity toward C_2H_4 rather than C_2H_5OH. However, interestingly, Ren and co-workers reported approximately 2 times higher selectivity toward C_2H_5OH on the phase-separated Cu–Zn (4:1) compared to Cu catalysts at their peak performance (Ren et al., 2016). To elucidate the origin of the high C_2H_5OH selectivity, it is necessary to discuss the reaction mechanism, which, at present, remains unclear. There are several proposed pathways for C_2H_4 and C_2H_5OH formation, which involve variations in C–C bond formation and subsequent intermediate reduction steps leading to the production of C_2H_5OH (Calle-Vallejo and Koper, 2013; Garza et al., 2018; Kortlever et al., 2015; Lum et al., 2018). C_2H_5OH can potentially be produced through various coupling reactions such as *CO–*CO, *CO–*CHO, and *CHO–*CHO on Cu-based catalysts (Garza et al., 2018; Luo et al., 2016; Lv et al., 2020; Piqué, Viñes, Illas, and Calle-Vallejo, 2020; Ting et al., 2020). Previous theoretical and experimental studies have also suggested that *CH_3CHO served as a key intermediate in the production of C_2H_5OH (Bertheussen et al., 2016; Calle-Vallejo and Koper, 2013; Hori, Takahashi, Yoshinami, and Murata, 1997; Santatiwongchai et al., 2021; Ting et al., 2020). Therefore, gaining mechanistic insights into the selectivity between C_2H_5OH and C_2H_4 could be valuable for designing catalysts with enhanced selectivity towards C_2H_5OH.

Pathway bifurcation toward the production of C_2H_4 and C_2H_5OH has been suggested to occur at a late stage (Karapinar et al., 2021; Nitopi et al., 2019; Todorova et al., 2020). Therefore, in this work, we investigate the subsequent protonation steps following the *CO–*CH coupling reaction, resulting in the formation of *CHCO intermediate, which can further lead to the production of C_2H_4 and C_2H_5OH. These pathways are studied at both the interface and Cu sites, as shown in **Figure 4.16** Various possible protonation sites were considered for each intermediate state. Moreover, we considered the C–O bond-breaking steps of *CH_2CH_2O and *CH_2CH_2OH intermediates, as these steps have been identified as potential pathways leading to C_2H_4 production on the Cu(100) catalyst (Santatiwongchai et al., 2021).

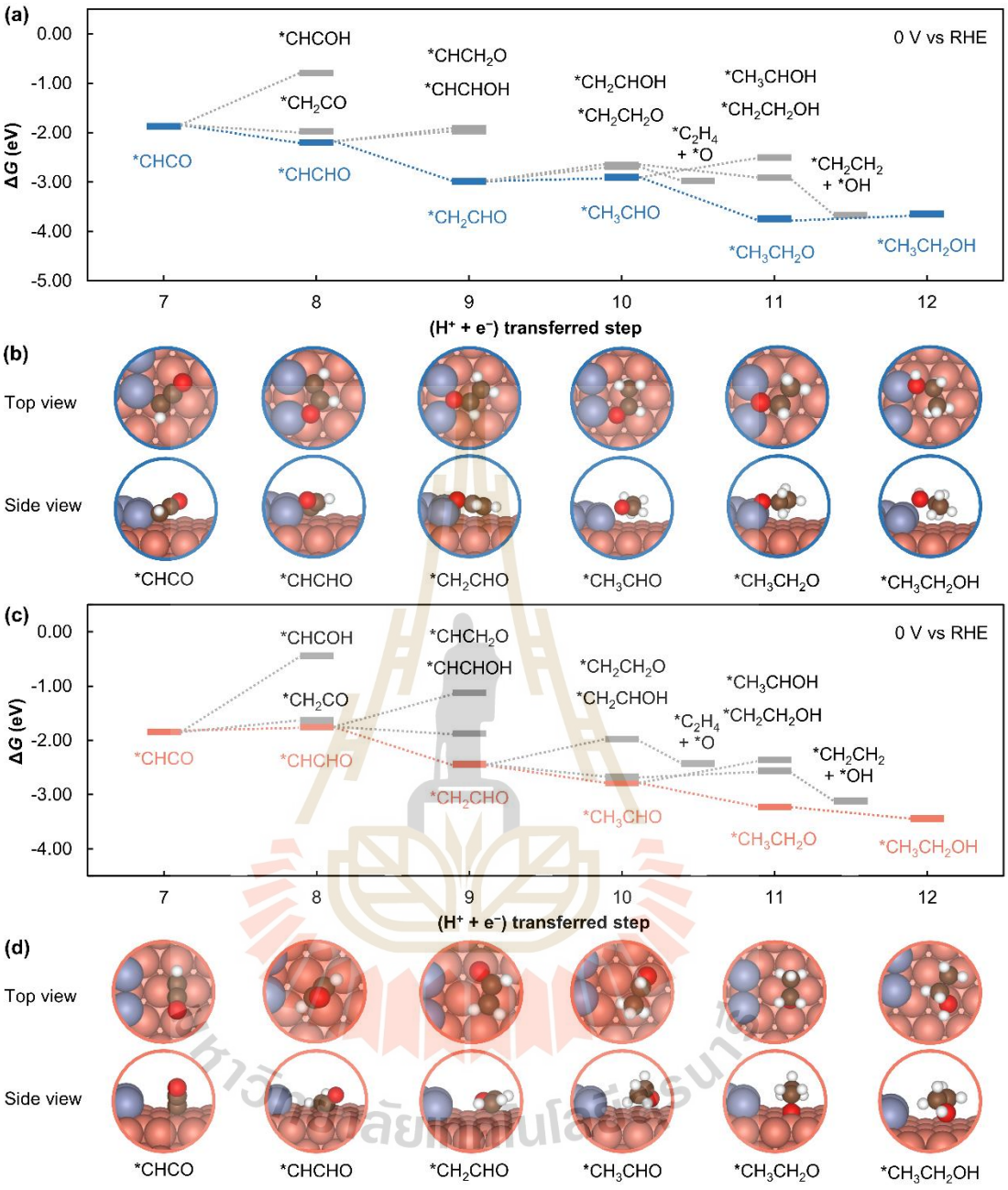

Figure 4.16 Relative energy profiles for the subsequent reduction of C_2 intermediates upon *CO–*CH coupling reaction toward ethylene (gray) and ethanol (blue/orange) products at (a) interface and (c) Cu sites on the phase-separated Cu–Zn structure, and the corresponding adsorbed configurations at (b) interface and (d) Cu sites, respectively. The free energy reference is the state of * + 2×(CO_2 (g)) + 12×(½H_2 (g)).

As illustrated in **Figure 4.16(a)**, the most thermodynamically favorable pathway at the interface site is *CHCO ⟶ *CHCHO ⟶ *CH_2CHO ⟶ *CH_3CHO ⟶ *CH_3CH_2O ⟶ *CH_3CH_2OH. After the formation of *CHCO, the intermediates prefer to adsorb at the Zn sites at the interface, as depicted in **Figure 4.16(b)**. The unsaturated carbon atom of *CHCO binds to the interfacial Zn atom, while both the O and C atoms of *CHCHO binds to the interfacial Zn atom. However, in the case of all the latter intermediates, only the O atom binds to the interfacial Zn atom. Although the formations of *CH_3CHO and *CH_3CH_2OH are slightly energetically uphill with reaction energies of approximately 0.1 eV, it is anticipated that these reactions can still be facile when applying electrical potential as the driving force. The pathway is found to be consistent with previous works that have reported the preference for C_2H_5OH formation after the formation of *COCH, followed by subsequent reduction to *CH_3CHO (Lv et al., 2020; Ocampo-Restrepo, Verga, and Da Silva, 2023; Piqué et al., 2020). This finding is in agreement with experimental results that showed the detection of a small amount of CH_3CHO product in the same potential range of −0.85 to −1.15 V vs. RHE, where C_2H_5OH was also observed, on the phase-separated Cu–Zn (4:1) catalyst (Juntrapirom et al., 2021). This information supports the notion that the interface site may favor C_2H_5OH production through a pathway involving *CH_3CHO, as exhibited in **Figure 4.16(a).**

Furthermore, the C–O bond-breaking reactions are found to be exergonic for *CH_2CH_2O and *CH_2CH_2OH. However, these intermediates are less stable, and the preferred pathway toward ethanol is more likely to proceed through *CH_3CH_2O, which is strongly stabilized at the interface site. Therefore, the C_2H_5OH pathway is preferred at the interface site compared to the C_2H_4 pathway through the C–O bond breaking of *CH_2CH_2O and *CH_2CH_2OH intermediates.

The energy profile of the pathways on the Cu sites is presented in **Figure 4.16(c)**. The most stable intermediates at each protonation state, leading to ethanol production, are the same as those at the interface site. While the other protonation steps are exergonic, the protonation of *CHCO to *CHCHO is slightly energetically uphill by 0.09 eV. **Figure 4.16(d)** illustrates the adsorption configurations on the Cu sites, which are found to be similar to those at the interface site in terms of how the

intermediates atoms bind to the catalyst atom Cu compared to Zn. In addition, the C–O breaking steps of $*CH_2CH_2O$ and $*CH_2CH_2OH$ are exergonic. However, the formation of $*CH_2CH_2O$ and $*CH_2CH_2OH$ is significantly less favorable, indicating that the formation of C_2H_4 via these steps may not be preferred. Therefore, the Cu site favors C_2H_5OH production over C_2H_4 production. This finding is consistent with the previous computational works, which showed that pure Cu(111) catalyst prefers C_2H_5OH production over C_2H_4 production once *COCH and $*CH_3CHO$ are formed (Piqué et al., 2020; Ting et al., 2020).

To gain a better understanding of the C_2H_5OH production performance at the interface and Cu sites, we compared the stability of these intermediates as depicted in **Figure 4.17.** It is observed that all the intermediates adsorbed at the interface site are more stabilized than those at the Cu site. In the computational study by Piqué and co-workers, it was revealed that low-coordinated sites enhance C_2H_5OH production on the Cu-island deposited on Cu(100) and Cu(111) surfaces by stabilizing the intermediates along the pathway (Piqué et al., 2020). Therefore, the geometric effect of phase-separated Cu–Zn catalyst is one of the crucial factors for enhancing C_2H_5OH selectivity.

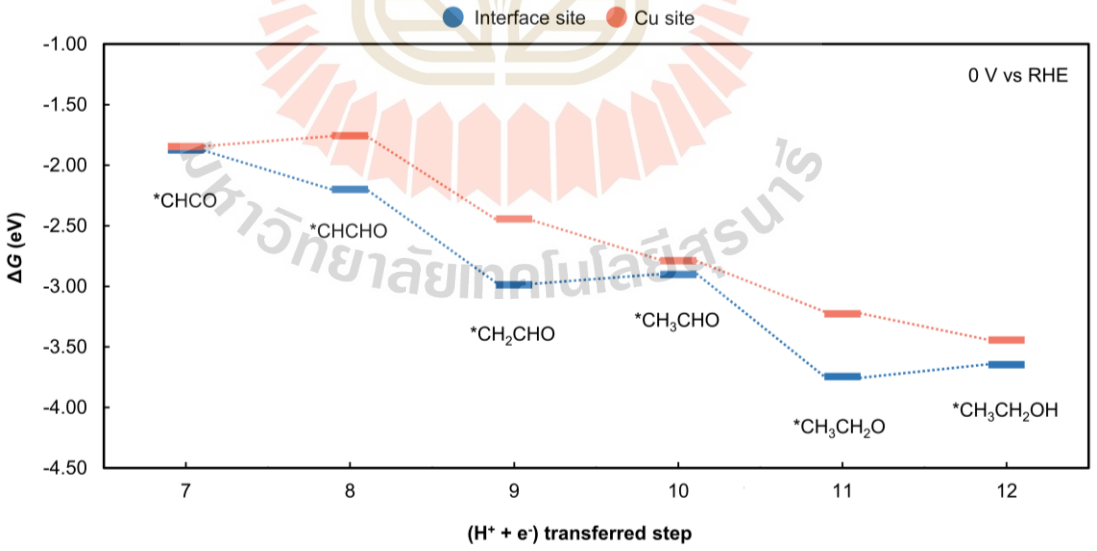

Figure 4.17 Relative free energy profiles for the subsequent C_2 intermediates reductions upon *CO–*CH coupling reaction toward ethanol product at the interface and Cu sites on phase-separated Cu–Zn structure.

4.4 Conclusions

In this work, we theoretically studied the effect of the interface Cu–Zn site on CO_2RR to C_2H_5OH of phase-separated Cu–Zn catalysts. Our results show that the interface site affects the stability of the key intermediates along the reaction pathway: stabilizing *COOH and destabilizing *CO of the CO pathway, thus promoting the further production of alkyl intermediates of the CH_4 pathway. The interface site also facilitates HER, which may affect C_2 production. Among the *CO–*C_1 coupling reactions, the *CO–*CH coupling is an exergonic reaction and the most kinetically favorable with $\Delta G^{\neq}$ of 0.27 eV at the interface site, which is significantly lower than $\Delta G^{\neq}$ of 0.52 eV at the Cu site. This emphasizes the cooperative effect of the interface site on promoting the coupling reaction for C_2 production. At the late steps of CO_2RR, the C_2H_5OH production is more thermodynamically preferred than the C_2H_4 through the *COCH pathway at both interface and Cu sites. The interface site strongly stabilizes the intermediates of the C_2H_5OH pathway compared to the Cu site, leading to more facile C_2H_5OH production. Overall, this work reveals the effect of the interface Cu–Zn site on selective CO_2RR to C_2H_5OH as one of the vital factors to be considered in the design of bimetallic Cu-based electrocatalysts.

4.5 References

Aguado, A., Vega, A., Lebon, A., and von Issendorff, B. (2018). Are zinc clusters really amorphous? A detailed protocol for locating global minimum structures of clusters. *Nanoscale, 10*(40), 19162-19181.

Bertheussen, E., Verdaguer-Casadevall, A., Ravasio, D., Montoya, J. H., Trimarco, D. B., Roy, C., Meier, S., Wendland, J., Nørskov, J. K., Stephens, I. E. L., and Chorkendorff, I. (2016). Acetaldehyde as an intermediate in the electroreduction of carbon monoxide to ethanol on oxide-derived copper. *Angewandte Chemie International Edition, 55*(4), 1450-1454.

Birdja, Y. Y., Pérez-Gallent, E., Figueiredo, M. C., Göttle, A. J., Calle-Vallejo, F., and Koper, M. T. M. (2019). Advances and challenges in understanding the electrocatalytic conversion of carbon dioxide to fuels. *Nature Energy, 4*(9), 732-745.

Blöchl, P. E. (1994). Projector augmented-wave method. *Physical Review B, 50*(24), 17953-17979.

Calle-Vallejo, F., and Koper, M. T. M. (2013). Theoretical considerations on the electroreduction of CO to C_2 species on Cu(100) electrodes. *Angewandte Chemie International Edition, 52*(28), 7282-7285.

Cave, E. R., Shi, C., Kuhl, K. P., Hatsukade, T., Abram, D. N., Hahn, C., Chan, K., and Jaramillo, T. F. (2018). Trends in the catalytic activity of hydrogen evolution during CO_2 electroreduction on transition metals. *ACS Catalysis, 8*(4), 3035-3040.

Dong, H., Li, Y., and Jiang, D.-e. (2018). First-principles insight into electrocatalytic reduction of CO_2 to CH_4 on a copper nanoparticle. *The Journal of Physical Chemistry C, 122*(21), 11392-11398.

Etim, U. J., Zhang, C., and Zhong, Z. (2021). Impacts of the catalyst structures on CO_2 activation on catalyst surfaces. *Nanomaterials, 11*(12), 3265.

Feaster, J. T., Shi, C., Cave, E. R., Hatsukade, T., Abram, D. N., Kuhl, K. P., Hahn, C., Nørskov, J. K., and Jaramillo, T. F. (2017). Understanding selectivity for the electrochemical reduction of carbon dioxide to formic acid and carbon monoxide on metal electrodes. *ACS Catalysis, 7*(7), 4822-4827.

Feng, Y., Li, Z., Liu, H., Dong, C., Wang, J., Kulinich, S. A., and Du, X. (2018). Laser-prepared CuZn alloy catalyst for selective electrochemical reduction of CO_2 to ethylene. *Langmuir, 34*(45), 13544-13549.

Garza, A. J., Bell, A. T., and Head-Gordon, M. (2018). Mechanism of CO_2 reduction at copper surfaces: Pathways to C_2 products. *ACS Catalysis, 8*(2), 1490-1499.

Gawande, M. B., Goswami, A., Felpin, F.-X., Asefa, T., Huang, X., Silva, R., Zou, X., Zboril, R., and Varma, R. S. (2016). Cu and Cu-based nanoparticles: Synthesis and applications in catalysis. *Chemical Reviews, 116*(6), 3722-3811.

Grimme, S., Antony, J., Ehrlich, S., and Krieg, H. (2010). A consistent and accurate ab initio parametrization of density functional dispersion correction (DFT-D) for the 94 elements H-Pu. *The Journal of Chemical Physics, 132*(15), 154104.

Hammer, B., Hansen, L. B., and Nørskov, J. K. (1999). Improved adsorption energetics within density-functional theory using Revised Perdew-Burke-Ernzerhof functionals. *Physical Review B, 59*(11), 7413-7421.

Henkelman, G., and Jónsson, H. (1999). A dimer method for finding saddle points on high dimensional potential surfaces using only first derivatives. *The Journal of Chemical Physics, 111*(15), 7010-7022.

Henkelman, G., Uberuaga, B. P., and Jónsson, H. (2000). A climbing image nudged elastic band method for finding saddle points and minimum energy paths. *The Journal of Chemical Physics, 113*(22), 9901-9904.

Herzog, A., Bergmann, A., Jeon, H. S., Timoshenko, J., Kühl, S., Rettenmaier, C., Lopez Luna, M., Haase, F. T., and Roldan Cuenya, B. (2021). Operando investigation of Ag-decorated Cu_2O nanocube catalysts with enhanced CO_2 electroreduction toward liquid products. *Angewandte Chemie International Edition, 60*(13), 7426-7435.

Hori, Y. (2008). Electrochemical CO_2 reduction on metal electrodes. In C. G. Vayenas, R. E. White, and M. E. Gamboa-Aldeco (Eds.), *Modern aspects of electrochemistry* (pp. 89-189). New York, NY: Springer New York.

Hori, Y., Konishi, H., Futamura, T., Murata, A., Koga, O., Sakurai, H., and Oguma, K. (2005). "Deactivation of copper electrode" in electrochemical reduction of CO_2. *Electrochimica Acta, 50*(27), 5354-5369.

Hori, Y., Takahashi, R., Yoshinami, Y., and Murata, A. (1997). Electrochemical reduction of CO at a copper electrode. *The Journal of Physical Chemistry B, 101*(36), 7075-7081.

Hori, Y., Wakebe, H., Tsukamoto, T., and Koga, O. (1994). Electrocatalytic process of CO selectivity in electrochemical reduction of CO_2 at metal electrodes in aqueous media. *Electrochimica Acta, 39*(11), 1833-1839.

Hussain, J., Jónsson, H., and Skúlason, E. (2016). Faraday efficiency and mechanism of electrochemical surface reactions: CO_2 reduction and H_2 formation on Pt(111). *Faraday Discussions, 195*(0), 619-636.

Hussain, J., Jónsson, H., and Skúlason, E. (2018). Calculations of product selectivity in electrochemical CO_2 reduction. *ACS Catalysis, 8*(6), 5240-5249.

Hussain, J., Skúlason, E., and Jónsson, H. (2015). Computational study of electrochemical CO_2 reduction at transition metal electrodes. *Procedia Computer Science, 51*, 1865-1871.

Jafarzadeh, A., Bal, K. M., Bogaerts, A., and Neyts, E. C. (2020). Activation of CO_2 on copper surfaces: The synergy between electric field, surface morphology, and excess electrons. *The Journal of Physical Chemistry C, 124*(12), 6747-6755.

Jeon, H. S., Timoshenko, J., Scholten, F., Sinev, I., Herzog, A., Haase, F. T., and Roldan Cuenya, B. (2019). Operando insight into the correlation between the structure and composition of CuZn nanoparticles and their selectivity for the electrochemical CO_2 reduction. *Journal of the American Chemical Society, 141*(50), 19879-19887.

Jouny, M., Luc, W., and Jiao, F. (2018). General techno-economic analysis of CO_2 electrolysis systems. *Industrial & Engineering Chemistry Research, 57*(6), 2165-2177.

Jouny, M., Luc, W., and Jiao, F. (2020). Correction to "General techno-economic analysis of CO_2 electrolysis systems". *Industrial & Engineering Chemistry Research, 59*(16), 8121-8123.

Juntrapirom, S., Santatiwongchai, J., Watwiangkham, A., Suthirakun, S., Butburee, T., Faungnawakij, K., Chakthranont, P., Hirunsit, P., and Rungtaweevoranit, B. (2021). Tuning CuZn interfaces in metal–organic framework-derived electrocatalysts for enhancement of CO_2 conversion to C_2 products. *Catalysis Science & Technology, 11*(24), 8065-8078.

Karapinar, D., Creissen, C. E., Rivera de la Cruz, J. G., Schreiber, M. W., and Fontecave, M. (2021). Electrochemical CO_2 reduction to ethanol with copper-based catalysts. *ACS Energy Letters, 6*(2), 694-706.

Kortlever, R., Shen, J., Schouten, K. J. P., Calle-Vallejo, F., and Koper, M. T. M. (2015). Catalysts and reaction pathways for the electrochemical reduction of carbon dioxide. *The Journal of Physical Chemistry Letters, 6*(20), 4073-4082.

Kresse, G., and Furthmüller, J. (1996). Efficient iterative schemes for ab initio total-energy calculations using a plane-wave basis set. *Physical Review B, 54*(16), 11169-11186.

Kresse, G., and Joubert, D. (1999). From ultrasoft pseudopotentials to the projector augmented-wave method. *Physical Review B, 59*(3), 1758-1775.

Kuhl, K. P., Hatsukade, T., Cave, E. R., Abram, D. N., Kibsgaard, J., and Jaramillo, T. F. (2014). Electrocatalytic conversion of carbon dioxide to methane and methanol on transition metal surfaces. *Journal of the American Chemical Society, 136*(40), 14107-14113.

Li, J., Wang, Z., McCallum, C., Xu, Y., Li, F., Wang, Y., Gabardo, C. M., Dinh, C.-T., Zhuang, T.-T., Wang, L., Howe, J. Y., Ren, Y., Sargent, E. H., and Sinton, D. (2019). Constraining CO coverage on copper promotes high-efficiency ethylene electroproduction. *Nature Catalysis, 2*(12), 1124-1131.

Li, X., Wu, X., Lv, X., Wang, J., and Wu, H. B. (2022). Recent advances in metal-based electrocatalysts with hetero-interfaces for CO_2 reduction reaction. *Chem Catalysis, 2*(2), 262-291.

Li, Y., Tian, Z., and Chen, L. (2021). Theoretical understanding of the interface effect in promoting electrochemical CO_2 reduction on Cu–Pd alloys. *The Journal of Physical Chemistry C, 125*(39), 21381-21389.

Li, Y. C., Wang, Z., Yuan, T., Nam, D.-H., Luo, M., Wicks, J., Chen, B., Li, J., Li, F., de Arquer, F. P. G., Wang, Y., Dinh, C.-T., Voznyy, O., Sinton, D., and Sargent, E. H. (2019). Binding site diversity promotes CO_2 electroreduction to ethanol. *Journal of the American Chemical Society, 141*(21), 8584-8591.

Lin, W.-Y., Chen, Z.-X., Xiong, H., Li, H.-C., Ho, Y.-S., Hsieh, C.-T., Lu, Q., and Cheng, M.-J. (2023). Identification of CO_2 as a reactive reagent for C–C bond formation via copper-catalyzed electrochemical reduction. *ACS Catalysis, 13*(17), 11697-11710.

Lum, Y., Cheng, T., Goddard, W. A., and Ager, J. W. (2018). Electrochemical CO reduction builds solvent water into oxygenate products. *Journal of the American Chemical Society, 140*(30), 9337-9340.

Luo, W., Nie, X., Janik, M. J., and Asthagiri, A. (2016). Facet dependence of CO_2 reduction paths on Cu electrodes. *ACS Catalysis, 6*(1), 219-229.

Luo, W., Zhang, Q., Zhang, J., Moioli, E., Zhao, K., and Züttel, A. (2020). Electrochemical reconstruction of ZnO for selective reduction of CO_2 to CO. *Applied Catalysis B: Environmental, 273*, 119060.

Lv, X., Shang, L., Zhou, S., Li, S., Wang, Y., Wang, Z., Sham, T.-K., Peng, C., and Zheng, G. (2020). Electron-deficient Cu sites on Cu_3Ag_1 catalyst promoting CO_2 electroreduction to alcohols. *Advanced Energy Materials, 10*(37), 2001987.

Ma, S., Sadakiyo, M., Heima, M., Luo, R., Haasch, R. T., Gold, J. I., Yamauchi, M., and Kenis, P. J. A. (2017). Electroreduction of carbon dioxide to hydrocarbons using bimetallic Cu–Pd catalysts with different mixing patterns. *Journal of the American Chemical Society, 139*(1), 47-50.

Mathew, K., Sundararaman, R., Letchworth-Weaver, K., Arias, T. A., and Hennig, R. G. (2014). Implicit solvation model for density-functional study of nanocrystal surfaces and reaction pathways. *The Journal of Chemical Physics, 140*(8), 084106.

Methfessel, M., and Paxton, A. T. (1989). High-precision sampling for brillouin-zone integration in metals. *Physical Review B, 40*(6), 3616-3621.

Monkhorst, H. J., and Pack, J. D. (1976). Special points for brillouin-zone integrations. *Physical Review B, 13*(12), 5188-5192.

Morales-Guio, C. G., Cave, E. R., Nitopi, S. A., Feaster, J. T., Wang, L., Kuhl, K. P., Jackson, A., Johnson, N. C., Abram, D. N., Hatsukade, T., Hahn, C., and Jaramillo, T. F. (2018). Improved CO_2 reduction activity towards C_{2+} alcohols on a tandem gold on copper electrocatalyst. *Nature Catalysis, 1*(10), 764-771.

Nie, X., Esopi, M. R., Janik, M. J., and Asthagiri, A. (2013). Selectivity of CO_2 reduction on copper electrodes: The role of the kinetics of elementary steps. *Angewandte Chemie International Edition, 52*(9), 2459-2462.

Nitopi, S., Bertheussen, E., Scott, S. B., Liu, X., Engstfeld, A. K., Horch, S., Seger, B., Stephens, I. E. L., Chan, K., Hahn, C., Nørskov, J. K., Jaramillo, T. F., and Chorkendorff, I. (2019). Progress and perspectives of electrochemical CO_2 reduction on copper in aqueous electrolyte. *Chemical Reviews, 119*(12), 7610-7672.

Nørskov, J. K., Rossmeisl, J., Logadottir, A., Lindqvist, L., Kitchin, J. R., Bligaard, T., and Jónsson, H. (2004). Origin of the overpotential for oxygen reduction at a fuel-cell cathode. *The Journal of Physical Chemistry B, 108*(46), 17886-17892.

Ocampo-Restrepo, V. K., Verga, L. G., and Da Silva, J. L. F. (2023). Ab initio study for late steps of CO_2 and CO electroreduction: From CHCO* toward C_2 products on Cu and CuZn nanoclusters. *Physical Chemistry Chemical Physics*, *25*, 32931-32938.

Ou, L., and Chen, J. (2020). Theoretical insights into the effect of the overpotential on CO electroreduction mechanisms on Cu(111): Regulation and application of electrode potentials from a CO coverage-dependent electrochemical model. *Physical Chemistry Chemical Physics, 22*(1), 62-73.

Ou, L., Chen, J., Chen, Y., and Jin, J. (2019). Mechanistic study on Cu-catalyzed CO_2 electroreduction into CH_4 at simulated low overpotentials based on an improved electrochemical model. *Physical Chemistry Chemical Physics, 21*(28), 15531-15540.

Peterson, A. A., Abild-Pedersen, F., Studt, F., Rossmeisl, J., and Nørskov, J. K. (2010). How copper catalyzes the electroreduction of carbon dioxide into hydrocarbon fuels. *Energy & Environmental Science, 3*(9), 1311-1315.

Piqué, O., Viñes, F., Illas, F., and Calle-Vallejo, F. (2020). Elucidating the structure of ethanol-producing active sites at oxide-derived Cu electrocatalysts. *ACS Catalysis, 10*(18), 10488-10494.

Qin, B., Li, Y., Fu, H., Wang, H., Chen, S., Liu, Z., and Peng, F. (2018). Electrochemical reduction of CO_2 into tunable syngas production by regulating the crystal facets of earth-abundant Zn catalyst. *ACS Applied Materials & Interfaces, 10*(24), 20530-20539.

Reichenbach, T., Walter, M., Moseler, M., Hammer, B., and Bruix, A. (2019). Effects of gas-phase conditions and particle size on the properties of Cu(111)-supported Zn_yO_x particles revealed by global optimization and ab initio thermodynamics. *The Journal of Physical Chemistry C, 123*(51), 30903-30916.

Ren, D., Ang, B. S.-H., and Yeo, B. S. (2016). Tuning the selectivity of carbon dioxide electroreduction toward ethanol on oxide-derived Cu_xZn catalysts. *ACS Catalysis, 6*(12), 8239-8247.

Sandberg, R. B., Montoya, J. H., Chan, K., and Nørskov, J. K. (2016). CO-CO coupling on Cu facets: Coverage, strain and field effects. *Surface Science, 654*, 56-62.

Santatiwongchai, J., Faungnawakij, K., and Hirunsit, P. (2021). Comprehensive mechanism of CO_2 electroreduction toward ethylene and ethanol: The solvent effect from explicit water–Cu(100) interface models. *ACS Catalysis, 11*(15), 9688-9701.

Su, X., Sun, Y., Jin, L., Zhang, L., Yang, Y., Kerns, P., Liu, B., Li, S., and He, J. (2020). Hierarchically porous Cu/Zn bimetallic catalysts for highly selective CO_2 electroreduction to liquid C_2 products. *Applied Catalysis B: Environmental, 269*, 118800.

Tantardini, C., and Oganov, A. R. (2021). Thermochemical electronegativities of the elements. *Nature Communications, 12*(1), 2087.

Ting, L. R. L., Piqué, O., Lim, S. Y., Tanhaei, M., Calle-Vallejo, F., and Yeo, B. S. (2020). Enhancing CO_2 electroreduction to ethanol on copper–silver composites by opening an alternative catalytic pathway. *ACS Catalysis, 10*(7), 4059-4069.

Todorova, T. K., Schreiber, M. W., and Fontecave, M. (2020). Mechanistic understanding of CO_2 reduction reaction (CO_2RR) toward multicarbon products by heterogeneous copper-based catalysts. *ACS Catalysis, 10*(3), 1754-1768.

Vasileff, A., Xu, C., Jiao, Y., Zheng, Y., and Qiao, S.-Z. (2018). Surface and interface engineering in copper-based bimetallic materials for selective CO_2 electroreduction. *Chem, 4*(8), 1809-1831.

Wang, X., de Araújo, J. F., Ju, W., Bagger, A., Schmies, H., Kühl, S., Rossmeisl, J., and Strasser, P. (2019). Mechanistic reaction pathways of enhanced ethylene yields during electroreduction of CO_2–CO co-feeds on Cu and Cu-tandem electrocatalysts. *Nature Nanotechnology, 14*(11), 1063-1070.

Wang, Y., Wang, Z., Dinh, C.-T., Li, J., Ozden, A., Golam Kibria, M., Seifitokaldani, A., Tan, C.-S., Gabardo, C. M., Luo, M., Zhou, H., Li, F., Lum, Y., McCallum, C., Xu, Y., Liu, M., Proppe, A., Johnston, A., Todorovic, P., Zhuang, T.-T., Sinton, D., Kelley, S. O., and Sargent, E. H. (2020). Catalyst synthesis under CO_2 electroreduction favours faceting and promotes renewable fuels electrosynthesis. *Nature Catalysis, 3*(2), 98-106.

Won, D. H., Shin, H., Koh, J., Chung, J., Lee, H. S., Kim, H., and Woo, S. I. (2016). Highly efficient, selective, and stable CO_2 electroreduction on a hexagonal Zn catalyst. *Angewandte Chemie International Edition, 55*(32), 9297-9300.

Xiao, J., Gao, M.-R., Liu, S., and Luo, J.-L. (2020). Hexagonal Zn nanoplates enclosed by Zn(100) and Zn(002) facets for highly selective CO_2 electroreduction to CO. *ACS Applied Materials & Interfaces, 12*(28), 31431-31438.

Xie, L., Liang, J., Priest, C., Wang, T., Ding, D., Wu, G., and Li, Q. (2021). Engineering the atomic arrangement of bimetallic catalysts for electrochemical CO_2 reduction. *Chemical Communications, 57*(15), 1839-1854.

Xu, L., Lin, J., Bai, Y., and Mavrikakis, M. (2018). Atomic and molecular adsorption on Cu(111). *Topics in Catalysis, 61*(9), 736-750.

Zhang, T., Li, X., Qiu, Y., Su, P., Xu, W., Zhong, H., and Zhang, H. (2018). Multilayered Zn nanosheets as an electrocatalyst for efficient electrochemical reduction of CO_2. *Journal of Catalysis, 357*, 154-162.

Zhu, W., Tackett, B. M., Chen, J. G., and Jiao, F. (2018). Bimetallic electrocatalysts for CO_2 reduction. *Topics in Current Chemistry, 376*(6), 41.

CHAPTER V
CONCLUSIONS

This thesis utilizes the density functional theory (DFT) method to study the CO_2 reduction reaction (CO_2RR) at the heterogeneous interface between Cu and Zn on the phase-separated bimetallic Cu–Zn electrocatalysts. The most stable Cu–Zn structure was chosen as the model — the surface model consists of a Zn-island on top of Cu(111) surface — to study CO_2RR at various active sites including Cu, Zn, and interface sites. The CO_2RR reaction was studied from the CO_2 activation to the late-stage reduction to C_2 products.

From the beginning, the interface site exhibited a more active role in CO_2 activation compared to those of other sites. Then, *COOH was strongly stabilized at the interface site, reducing the potential energy for *CO production. The *CO is more unstable at the interface site than the Cu site, promoting the productions of alkyl intermediates, and CH_4. The potential-determining step differs for the *CHO formation of the Cu site, and the *CHOH formation of the interface site. These show the obvious impacts of interface site on the C_1 pathway of CO_2RR.

The C_2 productions were proposed to initiate from the coupling reaction between two C_1 intermediates. In this study, the C–C coupling reactions were investigated between the *CO and all the C_1 intermediate of the CH_4 pathway at both interface, and Cu sites comparatively. Among them, *CO–*CH coupling at the interface site was the most favorable reaction in both thermodynamics and kinetics — A reaction free energy (ΔG_{rxn}) was -1.28 eV, and the free-energy barrier ($\Delta G^{\neq}$) was 0.27 eV. After this coupling step, the C_2H_5OH pathway was promoted over that of C_2H_4. The interface site stabilizes all the intermediates along the late-stage reduction to C_2H_5OH. These findings signify the effect of the interface site on selective CO_2RR toward C_2H_5OH on the phase-separated Cu–Zn catalyst.

This thesis highlights the cooperative role of the interface site on CO_2RR of the phase-separated Cu–Zn catalyst for selective C_2H_5OH production. The information will be beneficial for the design of those bimetallic Cu-based catalysts for CO_2RR.

APPENDICES

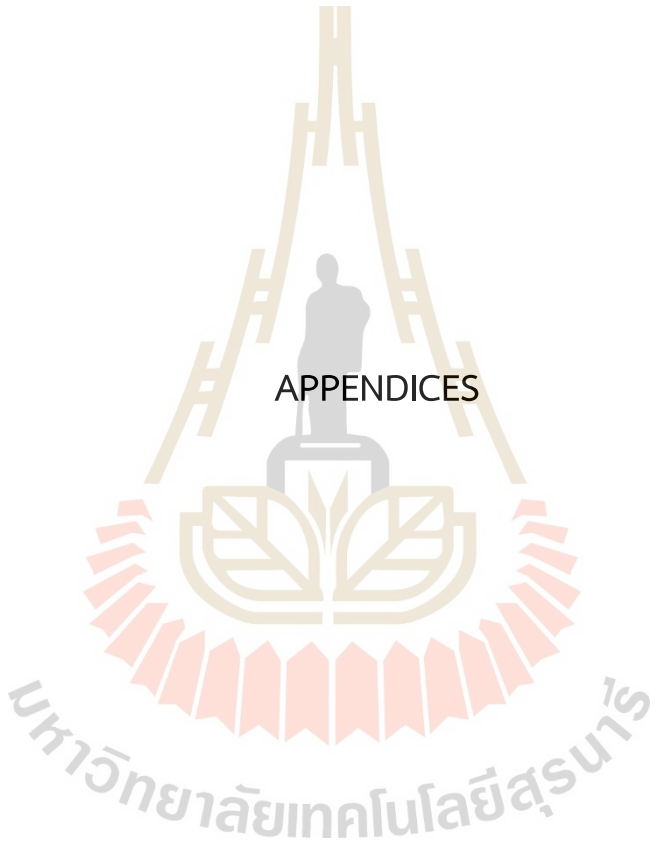

APPENDIX A

ADDITIONAL COMPUTATIONAL DETAILS

A.1 Calculated electronic energy (E_{elec}), zero-point energy correction (ZPE), enthalpic temperature correction ($\int C_p dT$), entropy contribution ($-TS_{vib}$), gas-phase RPBE correction (ΔG_{gas}) (Peterson, Abild-Pedersen, Studt, Rossmeisl, and Nørskov, 2010), and free energy correction of liquid-phase formation ($\Delta G_{g\rightarrow l}$) of each non-adsorbate species (Calle-Vallejo and Koper, 2013), respectively. The temperature (T) is 300 K. All values are given in eV.

Species	E_{elec}	ZPE	$\int C_p dT$	$-TS_{vib}$	ΔG_{gas}	$\Delta G_{g\rightarrow l}$
H_2 (g)	-6.99	0.29	0.11	0.30	0.09	-
H_2O (l)	-14.15	0.59	0.14	0.36	-0.21	-0.09
CO_2 (g)	-22.29	0.32	0.12	0.33	0.41	-
CO (g)	-14.43	0.15	0.11	0.31	-0.18	-

References

Calle-Vallejo, F., and Koper, M. T. M. (2013). Theoretical considerations on the electroreduction of CO to C_2 species on Cu(100) electrodes. *Angewandte Chemie International Edition, 52*(28), 7282-7285.

Peterson, A. A., Abild-Pedersen, F., Studt, F., Rossmeisl, J., and Nørskov, J. K. (2010). How copper catalyzes the electroreduction of carbon dioxide into hydrocarbon fuels. *Energy & Environmental Science, 3*(9), 1311-1315.

APPENDIX B

PUBLICATIONS AND PRESENTATIONS

B.1 List of publications

Juntrapirom, S., Santatiwongchai, J., Watwiangkham, A., Suthirakun, S., Butburee, T., Faungnawakij, K., Chakthranont, P., Hirunsit, P., Rungtaweevoranit, B. (2021). Tuning CuZn interfaces in metal–organic framework-derived electrocatalysts for enhancement of CO_2 conversion to C_2 products. *Catalysis Science & Technology*, *11*(24), 8065-8078.

Jankhunthod, S., Moonla, C., Watwiangkham, A., Suthirakun, S., Siritanon, T., Wannapaiboon, S., Ngamchuea, K. (2021). Understanding electrochemical and structural properties of copper hexacyanoferrate: Application in hydrogen peroxide analysis. *Electrochimica Acta*, *394*, 139147.

Nonkuntod, P., Meenongwa, A., Senawong, T., Soikum, C., Chaveerach, P., Watwiangkham, A., Suthirakun, S., Chaveerach, U. (2022). Mixed-ligand copper(II) complexes of guanidine derivatives containing ciprofloxacin: synthesis, characterization, DFT calculations, DNA interactions and biological activities. *New Journal of Chemistry*, *46*(25), 12342-12357.

Nonkuntod, P., Senawong, T., Soikum, C., Chaveerach, P., Watwiangkham, A., Suthirakun, S., Chaveerach, U. (2022). Copper(II) compounds of 4-nitrobenzohydrazide with different anions (ClO_4^-, NO_3^- and Br^-): Synthesis, characterization, DFT calculations, DNA interactions and cytotoxic properties. *Chemistry & Biodiversity*, *19*(3), e202100708.

Ngamchuea, K., Moonla, C., Watwiangkham, A., Wannapaiboon, S., Suthirakun, S. (2022). Electrochemical and structural investigation of copper phthalocyanine: Application in the analysis of kidney disease biomarker. *Electrochimica Acta*, *428*, 140951.

Jiamprasertboon, A., Waehayee, A., Sertwatsana, S., Nijpanich, S., Busayaporn, W., Eknapakul, T., Chanlek, N., Bootchanont, A., Sunkhunthod, C., Watwiangkham, A., Nakajima, H., Li, J., Subramanian, M. A., Suthirakun, S., Siritanon, T. (2023). Effects of M cations on crystal structure and optical properties of MTe_3O_8 tellurites. *Solid State Sciences*, *135*, 107067.

Nonkuntod, P., Boonmak, J., Senawong, T., Soikum, C., Chaveerach, P., Watwiangkham, A., Suthirakun, S., Chaveerach, U. (2023). The effect of gallic acid on the copper(II) complex of N-(methylpyridin-2-yl)-amidino-O-methylurea: Crystal structure, DNA interactions, in vitro cytotoxicity and antibacterial activity. *New Journal of Chemistry*, *47*(26), 12259-12273.

Singsen, S., Watwiangkham, A., Ngamwongwan, L., Fongkaew, I., Jungthawan, S., Suthirakun, S. (2023). Defect engineering of green phosphorene nanosheets for detecting volatile organic compounds: A computational approach. *ACS Applied Nano Materials*, *6*(2), 1496-1506.

Usmani, A., Tharat, B., Watwiangkham, A., Grisdanurak, N., Suthirakun, S. (2023). Enhancing kinetics of carbonyl sulfide hydrolysis using Pt-supported Al_2O_3 catalysts: First-principles-informed energetic span analysis. *The Journal of Physical Chemistry C*, *127*(19), 9002-9012.

Kaeosamut, N., Chaichana, P., Watwiangkham, A., Suthirakun, S., Wannapaiboon, S., Sammawipawekul, N., Chimupala, Y., Yimklan, S. (2023). Synergistic induction of solvent and ligand-substitution in single-crystal to single-crystal transformations toward a MOF with photocatalytic dye degradation. *Inorganic Chemistry*, *62*(49), 19908-19921.

Aryamueang, S., Chansaenpak, K., Watwiangkham, A., Suthirakun, S., Muangsopa, P., Wattanathana, W., Lai, R.-Y., Kamkaew, A. (2024). Imidazole-based styryl dyes as viscosity-sensitive agents. *Journal of Photochemistry and Photobiology A: Chemistry*, *447*, 115268.

Sammawipawekul, N., Kaeosamut, N., Autthawong, T., Watwiangkham, A., Suthirakun, S., Wannapaiboon, S., Mahamai, N., Sarakonsri, T., Chimupala, Y., Yimklan, S. (2024). Isostructural dual-ligand-based MOFs with different metal centers in response to diverse capacity lithium-ion battery anode. *Chemical Engineering Journal*, *482*, 148904.

Watwiangkham, A., Santatiwongchai, J., Suthirakun, S., Hirunsit, P., Cooperative phase-separated Cu–Zn catalyst for selective CO_2 electrochemical reduction toward ethanol: Theoretical insights into the role of the interface sites. (Submitted).

B.2 List of presentations

1. Watwiangkham, A., Suthirakun, S., and Hirunsit, P. (2022). Theoretical studies of carbon dioxide reduction to ethanol on the bimetallic Copper/Zinc electrocatalyst. **Pure and Applied Chemistry International Conference (PACCON 2022).** 30 June - 1 July 2022, KMITL Convention Hall, King Mongkut's Institute of Technology Ladkrabang, Bangkok, Thailand. (Oral presentation)

2. Watwiangkham, A., Santatiwongchai, J., Suthirakun, S., and Hirunsit, P. (2022). Role of interface sites of phase-separated Cu–Zn catalyst for selective CO_2 electrochemical reduction towards ethanol: Theoretical studies. **The 25th International Annual Symposium on Computational Science and Engineering 2022 (ANSCSE25).** 8 - 11 June 2022, Department of Physics, Faculty of Science, Khon Kaen University, Thailand. (Poster presentation)

Abstract submitted to The Pure and Applied Chemistry International Conference

(PACCON 2022)

PT-O-025

THEORETICAL STUDIES OF CARBON DIOXIDE REDUCTION TO ETHANOL ON THE BIMETALLIC COPPER/ZINC ELECTROCATALYST

A. Watwiangkham[1], S. Suthirakun[1], and P. Hirunsit[2]*

[1] *School of Chemistry, Institute of Science, Suranaree University of Technology, Nakhon Ratchasima, Thailand*

[2] *National Nanotechnology Center, National Science and Technology Development Agency, 111 Thailand Science Park, Pathum Thani, Thailand*

*Corresponding address (Email: Pussana@nanotec.or.th)

The carbon dioxide reduction reaction (CO_2RR) using Cu/Zn electrocatalysts is one of the efficient ways to convert the major greenhouse gas, CO_2, to a value-added product, especially ethanol. In this work, we study the effect of Zn on CO_2RR to ethanol on the Zn-cluster deposited Cu (111) model by using the density functional theory (DFT) method. From the results, the Zn cluster acts as a *CO producer, while the *CO undergoes spillover from the Zn to Cu sites. For the C-C coupling step to C_2 products, the Zn cluster promotes the *CO-*CH coupling at the Cu/Zn interface. After that, we consider all protonation sites of each stage after *COCH. Ethylene and ethanol pathways break at the $*CH_2CHO$ intermediate. The Zn stabilizes the $*CH_3CHO$ more than the $*CH_2CH_2O$, favoring the ethanol pathway rather than the ethylene pathway. Thus, the Zn affects CO_2RR to ethanol on Cu/Zn electrocatalysts by tuning the intermediate at the bifurcation between the ethylene and ethanol pathways. These findings can use as guidance in catalyst engineering of CO_2RR on bimetallic electrocatalysts.

Keywords: Carbon dioxide; Copper; Zinc; Ethanol; Density functional theory

Abstract submitted to The 25th International Annual Symposium on Computational Science and Engineering 2022 (ANSCSE25)

CHE-P-1

ROLE OF INTERFACE SITES OF PHASE-SEPARATED CU−ZN CATALYST FOR SELECTIVE CO_2 ELECTROCHEMICAL REDUCTION TOWARDS ETHANOL: THEORETICAL STUDIES

Athis Watwiangkham,[1] Jirapat Santatiwongchai,[2] Suwit Suthirakun,[1]* Pussana Hirunsit[2]*

[1]*School of Chemistry, Institute of Science, Suranaree University of Technology, Nakhon Ratchasima, Thailand*
[2]*National Nanotechnology Center (NANOTEC), National Science and Technology Development Agency (NSTDA), Pathum Thani, 12120 Thailand*

*(E-mail: pussana@nanotec.or.th, pussana.hirunsit@gmail.com (P.H), suthirak@sut.ac.th (S.S))

The carbon dioxide reduction reaction (CO_2RR) is one of the efficient ways to utilize CO_2. The bimetallic phase-separated Cu−Zn electrocatalysts can selectively produce C_2H_5OH from CO_2RR. However, the role of the Cu−Zn interface site has not been discussed before. Herein, we theoretically investigate the character of the interface Cu−Zn sites on the separated phase Cu−Zn catalyst in selective CO_2RR toward C_2H_5OH production. Interestingly, the interface facilitates the CO_2 reduction to CO by stabilizing the *COOH intermediate. Then, the interface site favors the CH_4 production by lowering the reaction energy of potential-determining step and stabilizing some intermediates along the pathway. Since the C_2 production requires the C−C coupling reaction, we systematically studied the coupling between *CO and C_1 intermediates. We find that the *CO−*CH coupling is the most favorable step at the interface site which is more favorable than that of the Cu site. Through the *COCH intermediate, production of C_2H_5OH is energetically preferred compared with that of C_2H_4. All intermediates of the C_2H_5OH route are more stable at the interface site than at the Cu site. This study highlights the role of the Cu−Zn interface site in the design of electrocatalysts in CO_2RR to achieve high C_2H_5OH production.

Keywords: Carbon dioxide reduction reaction; Cu−Zn catalysts; Ethanol; Density functional theory

CURRICULUM VITAE

Athis Watwiangkham, was born on October 30th, 1996, in Nong Khai, Thailand. From his undergraduate to doctoral studies, He received a scholarship from the Human Resource Development in Science Project (Science Achievement Scholarship of Thailand, SAST). He received his Bachelor of Science (Chemistry) with a first-class honor in 2018 from the Department of Chemistry, Faculty of Science, Khon Kaen University. In 2017, he did an internship in experimental photocatalysis at North Dakota State University (NDSU), Fargo, North Dakota, under the supervision of Prof. Dr. Eakalak Khan and Prof. Dr. Jayaraman Sivaguru. During his senior year of bachelor's degree, he did a senoir research project on the topic of 'Histone deacetylase inhibitory activities of flavonoid and anthraquinone analogs: A molecular docking study' under the supervision of Assoc. Prof. Dr. Khatcharin Siriwong.

He continued to pursue the master's program at the Department of Chemistry, Faculty of Science, Chiang Mai University, under the supervision of Prof. Dr. Nawee Kungwan. He received the degree of Master of Science in Chemistry in 2020 with a thesis on the topic of 'Theoretical investigation of photophysical properties and excited state intramolecular proton transfers of derivatives of 2-(2′-Hydroxyphenyl)benzothiazole and methyl salicylate for fluorescent materials'.

For his doctoral study, he joined the School of Chemistry, Suranaree University of Technology, Thailand in 2020, under the supervision of Assoc. Prof. Dr. Suwit Suthirakun and Dr. Pussana Hirunsit from the National Nanotechnology Center (NANOTEC). His thesis focused on a computational electrocatalysis of CO_2 conversion on metal surfaces. In 2023, he was a research visiting scholar studying a solid-liquid interface modeling in heterogeneous catalysis at the Department of Chemical Engineering, University of South Carolina (USC), Columbia, South Carolina, under the supervision of Prof. Dr. Andreas Heyden. He has published research articles in international journals with many collaborators, and participated in international conferences during the course of his doctoral degree.